NORTHWESTERN UNIVERSITY

Interplay between superconductivity and ferromagnetism at the $LaAlO_3/SrTiO_3$ interface

A DISSERTATION

SUBMITTED TO THE GRADUATE SCHOOL

IN PARTIAL FULFILLMENT OF THE REQUIREMENTS

for the degree

DOCTOR OF PHILOSOPHY

Field of Physics and Astronomy

By

Manan Mehta

EVANSTON, ILLINOIS

December 2015

ABSTRACT

Interplay between superconductivity and ferromagnetism at the $LaAlO_3/SrTiO_3$ interface

Manan Mehta

As we approach the limit of minimum feature size in silicon based technology, there is a need to move to novel, low-dimensional, multi-functional materials which can power the future generations of computers. Many complex oxide materials show a rich variety of multi-functional properties and are thought to be viable candidates for future computing devices. We study here one such complex oxide heterostructure, the $LaAlO_3/SrTiO_3$ (LAO/STO) interface, which has been shown to host a two dimensional electron gas (2DEG). Physical phenomena that have been observed at the interface include superconductivity, magnetism, a metal-to-insulator transition, and a gate voltage tuned two dimensional superconductor-to-insulator transition (SIT). This thesis presents evidence for the coexistence of the two conventionally competing phenomena of superconductivity and ferromagnetism at the interface. It further explores the interplay between the two orders through electrical transport measurements, which results in a novel manifestation of charge-vortex duality between the superconducting and insulating states as the system

is tuned through the gate voltage tuned SIT. A phenomenological model of the system is presented which helps explain the observed transport behaviour. Finally, the magnetic field tuned SIT at this interface is also presented along with a scaling analysis of the magnetoresistance.

Acknowledgements

Acknowledgements are the most read part of a thesis.

Taewan Noh

A lot of people have been instrumental for the successful completion of this document.

I would like to start by mentioning my advisor, Prof. Venkat Chandrasekhar. During my time as a graduate student in his lab, he has been an excellent teacher, a motivator and a constant source of inspiration to me. Not only did I learn many fundamental condensed matter concepts from him, but he also taught me how to be a thorough experimentalist. In addition, I owe my scientific writing and communication skills to him.

My seven years and a bit in the lab were made immeasurably more memorable and fun by the constant companionship of Taewan Noh and Scott Mayle, both of whom joined the lab with me in 2008. Taewan was subsequently also my flatmate for three years, and there were many occasions when we would be up late into the night debating everything from the physics of phase transitions to the superiority of cricket over baseball (despite many attempts from me to help him see the light, he still remains firmly in the baseball camp).

I was also fortunate to have worked with Goutam Sheet, who was a post-doc in the lab when I joined. From him I learned the basics of superconductivity and also the technique of point-contact spectroscopy. Both him and Jian Wei, another post-doc, were always happy to answer any questions we young graduate students had about the physics of the work happening in the lab.

To Dima Dikin, with whom I published all the work presented in this thesis, I owe a lot of gratitude. He was a constant guide to me while I was first introduced to making transport measurements at low temperatures. He also taught me many tricks for machining, for which I am very thankful.

From 2011, the lab was made livelier by the addition of two new graduate students Sam Davis and Tanuj Gupta. Sam, in particular, shared an office with me and Taewan, and we have had many lively discussions on a range of subjects.

Gratitude is also owed to Prof. John Ketterson and Prof. Vinayak Dravid for being on my committee and giving helpful advice about the thesis.

My parents, Mayank and Toral, have unceasingly supported me and have shown limitless patience during these last seven years, for which I am very grateful. My sister, Manasee, has also been there for an encouraging word whenever I needed to take my mind off the fact that I was more than 7500 miles from home.

Finally, Varada Bal, fellow graduate student and in whom I have found a friend for life.

Table of Contents

List of Tables

List of Figures

CHAPTER 1

Introduction

Herbert Kroemer famously declared in his Nobel lecture in 2000: "The interface is the device" [**1**]. Said in the context of semiconductor heterointerfaces, his statement is today proving to be true in the very active research field of heterointerfaces in complex oxide materials. The reason these materials attract the research efforts of many scientists world-wide, including physicists, material scientists, and chemists, is their tremendous potential: not only technological, but also as models to study fundamental concepts in condensed matter physics. Figure 1.1 shows the various physical phenomena that can be engineered in such materials, by tuning one or more of the spin, charge, and orbital degrees of freedom in these systems.

One of the paradigms of such an interfacial oxide system is the conducting gas that forms at the interface between the two band insulators, $LaAlO_3$ (LAO) and $SrTiO_3$ (STO), which was first reported in a pioneering paper by Ohtomo and Hwang in 2004 [**2**]. Both LAO and STO are perovskite oxides with very close lattice matching ($a_{LAO} = 3.789$ Å & $a_{STO} = 3.905$ Å), making possible epitaxial growth of one on another. Figure 1.2 shows the two different configurations possible for the epitaxial growth of LAO on STO. It was found that the interface is conducting, with $n-$type carriers, when LAO is grown on TiO_2 terminated STO; while the corresponding $p-$type interface, expected to form when LAO is grown on SrO terminated STO, was found to be insulating. It was also found that the

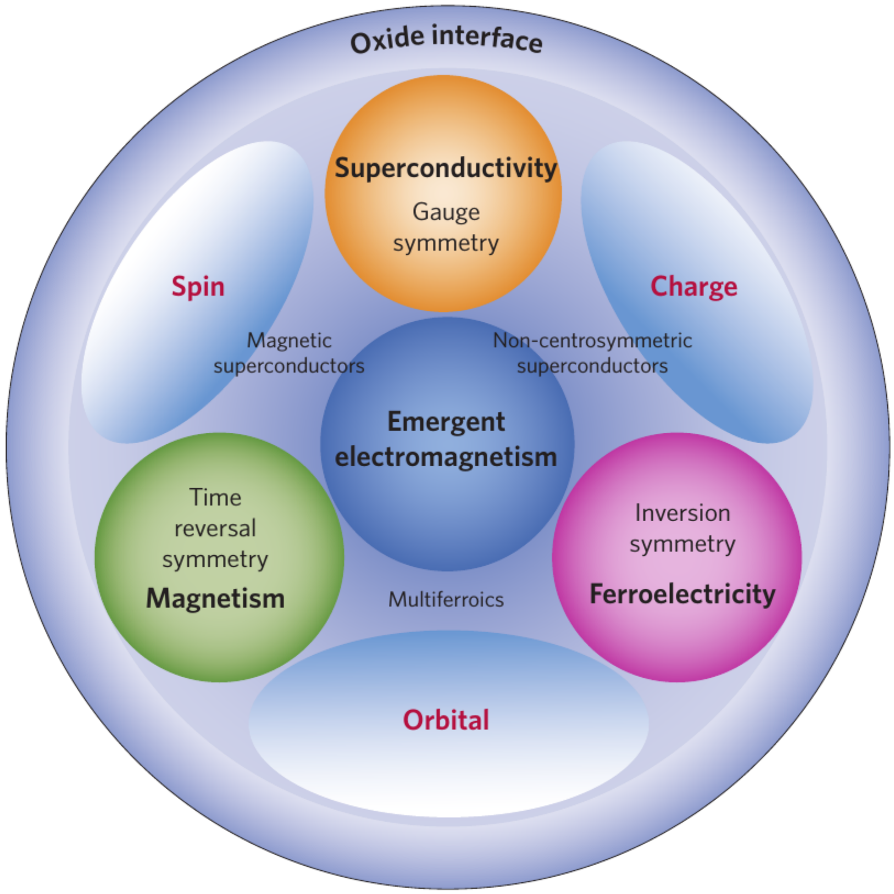

Figure 1.1. Schematic diagram showing the symmetries and degrees of freedom of correlated electrons that can be engineered at oxide interfaces. Figure and caption from Ref. 3.

electron gas that forms at the interface is essentially confined to it, forming a quasi-two dimensional electron gas (2DEG) [**4–6**]. There have since been a number of different reports on the observation of a multitude of rich physical phenomena at this interface. These include superconductivity [**5**], magnetism [**7**, **8**], a metal-to-insulator transition [**4**, **9**], and a two dimensional superconductor-to-insulator transition (SIT) [**6**]. The system is also one of the very few in nature to exhibit a coexistence of magnetism and superconductivity [**10–12**], making it an exciting laboratory for investigating the interplay between these two conventionally competing phenomena.

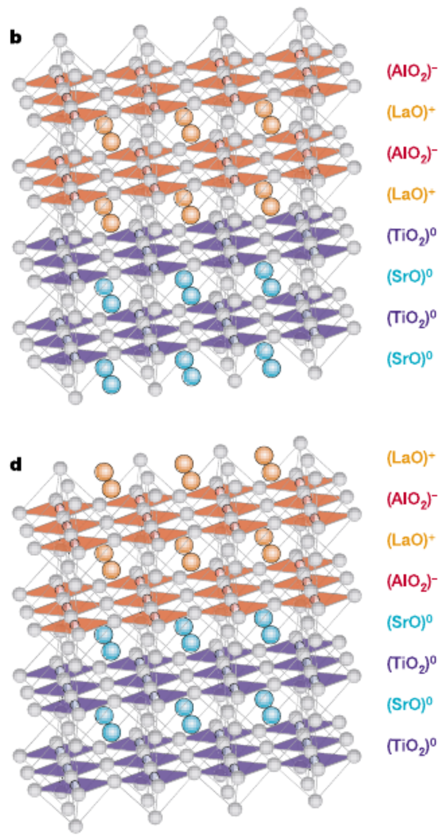

Figure 1.2. **LAO/STO interface.** Schematic models of the two possible interfaces between LAO and STO in the (001) orientation. **Top,** $(LaO)^+/(TiO_2)^0$ interface. **Bottom,** $(AlO_2)^-/(SrO)^0$. From Ref. 2

In this thesis, I will present electrical transport data which show this coexistence of ferromagnetism and superconductivity. I will then explore the effects of this coexistence on the transport properties of this system by studying its behaviour in the large phase space of varying temperatures, magnetic fields and gate voltages. One of the more interesting effects of this is the observation of a novel manifestation of the phenomenon of charge-vortex duality (CVD) [**13**] in the electric field tuned SIT at this interface. This manifestation of CVD is seen in the magnetoresistance (MR) of the 2DEG as a function of the gate voltage and is made possible by the influence of the magnetization dynamics in the ferromagnet on the superconducting electrons. I will also present my results on the magnetic field tuned SIT. Analyzing the results within the framework of scaling theory, I will show that the data suggest quantum percolation for this quantum phase transition.

Following is a summary of the organization of the remaining chapters of this thesis.

In Chapter 2, I will go over the relevant theoretical background needed to understand the electrical transport data I will present. I will go over the band structure and electronic properties of STO, where the charges in this system are thought to reside, and also discuss various proposed mechanisms of charge formation at this interface. I will then discuss the proposed theories to explain the coexistence of ferromagnetism and superconductivity. Finally, I will briefly present the different models and theories for the 2D-SIT, which still remains a contested field despite more than 3 decades of both theoretical and experimental research.

In Chapter 3, I will discuss the experimental techniques employed in order to study this system. This includes not only the epitaxial growth of the sample, which is done by Prof. Chang-Beom Eom's group at UW-Madison, but also the patterning of the Hall bars used for the transport data. The Hall bars were made using photo-lithography and Ar-ion milling. A majority of the transport data were obtained at milli-kelvin temperatures, which in our group are attained in two dilution refrigerators, a Kelvinox-100 and a Kelvinox-300, both from Oxford, both of which were used to make the measurements discussed in this thesis. I will also discuss the extreme care needed to make the kind of low-noise, sensitive measurements that are presented here and describe some of the instrumentation used to make such measurements.

Chapter 4 is the heart of the thesis. This chapter presents the experimental data and their analyses, and is broadly divided into four sections: (i) data for electrical characterization of the sample, including the gate voltage tuned SIT, (ii) data showing the coexistence of superconductivity and ferromagnetism, (iii) data showing the phenomenon of charge-vortex duality, and (iv) data for the magnetic field tuned SIT. I will also present our phenomenological model of the system, which explains the data for gate voltage tuned SIT and the coexistence of ferromagnetism and superconductivity. Additionally, I will present my analysis for the explanation of the observed features in the MR of this system. Finally, I will discuss how, within the scaling theory, the magnetic field tuned SIT at this interface points toward a quantum percolation model of the transition.

In Chapter 5, I will conclude this thesis. I will summarize the principal findings of this thesis and briefly discuss possible future research directions. These include local scanning probe measurements, making top-gated devices, and making further detailed transport measurements in order to resolve some of the outstanding issues regarding the physics in this system.

CHAPTER 2

Theoretical Background

In this chapter I will discuss the relevant theoretical background needed to understand the physical phenomena observed at the LAO/STO interface. I will start with a brief background and discussion of the properties of STO, focusing on the electronic properties. Strontium titanate is becoming the material of choice for use as a substrate in the newly emerging field of oxide electronics [**14**]. A large class of materials, grouped under the name perovskite oxides, so named owing to them sharing the perovskite crystal structure, have been grown successfully on STO, due to the matching crystal structures and also the closely matched lattice parameters for such structures. Examples include high temperature superconductors like YBCO ($YBa_2Cu_3O_{7-x}$) [**15**], ferroelectrics like BTO ($BaTiO_3$) [**16**], and heterostructures like LAO/STO. For the LAO/STO system, however, the role of STO is much more than just a structural substrate: most of the interesting physics in this system takes place in the electronic bands of STO. Specifically, the interesting two dimensional electron physics happens in the Ti bands of STO in a few atomic layers near the interface.

Although STO is a band insulator, it has been shown to conduct, and even superconduct, by doping. In the first part of this chapter, I will discuss some of the basics of the conduction mechanism in bulk STO, which has been studied historically and which will lay the groundwork upon which the conduction mechanisms at the LAO/STO interface

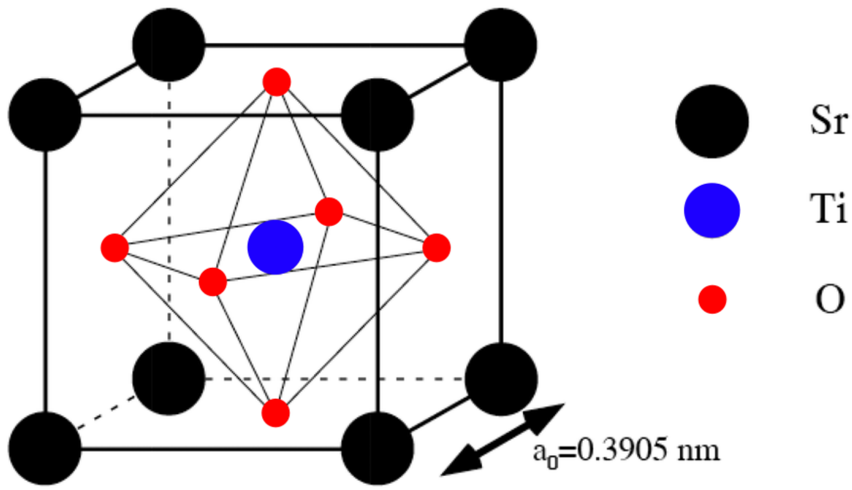

Figure 2.1. A unit cell of STO. Adapted from Bandura *et al.* [**17**]

can be understood. The rest of the chapter is divided into four parts: (i) the first part reviews some new work on surface states in STO, (ii) the second part goes over the proposed mechanisms for charge formation at the interface, (iii) the third part explains the current theoretical understanding behind the observed co-existence of superconductivity and ferromagnetism at the interface, (iv) while the fourth part describes the physics of the superconductor-insulator-transition in this system. A well grounded theoretical background of all of these would help in understanding the transport data of our samples.

2.1. STO as a substrate: electronic properties

Before discussing the band structure of STO, I will briefly state some of the salient properties of *bulk* STO that are relevant to understanding the phenomena at the LAO/STO interface. Newer insights into the nature of the two dimensional electron gas found at the *surface* of cleaved STO [**18**–**21**], will be discussed in a later section.

Bulk STO is a non-magnetic band insulator, with a band gap of 3.2 eV. At room temperature, STO is formed in the perovskite structure, a schematic unit cell of which is shown in Fig. 2.1. In the cubic unit cell shown, the Sr atoms are at the corners, the O atoms are at the face centers, while the Ti atoms reside at the center of the cube. At full ionicities in the stoichiometric compound, Sr has a valency of +2, O has has a valency of -2 and Ti is in the +4 oxidation state (the electronic configuration of Ti^{+4} is $[Ar]3d^0 4s^0$). In the fully ionic picture of the formation of an STO unit cell, the four electrons from Ti and the two from Sr are donated to the three O atoms. In reality, there is some evidence for a small degree of covalency also, i.e., the electrons are actually shared between the various atoms. Nevertheless it is useful and sufficient to think of the ionic picture without any loss of essential physics. In the +4 oxidation state, the Ti atom is non-magnetic with no unpaired electron in its d shell ($[Ar]3d^0 4s^0$). However, in the +3 oxidation state of Ti, with an electronic configuration $[Ar]3d^1 4s^0$, there does exist an unpaired electron spin which can give rise to magnetism.

STO also has a very high static dielectric constant, with $\epsilon \sim 10^4$ at low temperatures [**22**], which makes it a very good candidate for electrical gating of devices. This rise in the static dielectric constant is attributed to an increase in the long wavelength optical phonon frequencies at low temperatures [**22**]. It should also be noted that the dielectric constant of STO is dependent on the crystal orientation and also on the strength of an external applied electric field. While ϵ can reach values of $\sim 10^4$ for low field strength

($E \sim 10$ V/cm), it drops down to $\epsilon < 1000$ for electric field strength of $E \sim 20,000$ V/cm. Finally, although bulk, stoichiometric STO is insulating, on doping it with various electron donors like Nb, La, Zr or even by introducing oxygen vacancies, conduction and even superconductivity is observed in bulk STO [**23**–**29**]. There also occurs a structural phase transition in STO, from the high temperature cubic phase to the low temperature tetragonal phase at $T \sim 105$ K; which may also affect the properties of the electrons in the LAO/STO system. Below I discuss in brief the band diagram of STO.

Based on the calculation of atomic energies of Sr, Ti and O atoms [**30**, **31**], it can be shown that the band gap in STO arises from the O 2p orbitals, which form the valence band, and the Ti 3d orbitals, which form the conduction band. The energies of the Ti 4s and the Sr 5s orbitals are much above (≥ 10 eV), and those of the O 2s orbitals much below (≤ 10 eV) the Fermi energy to be of any significance in affecting the electronic properties. It can also be shown that the crystal field splitting results in two energy manifolds of the Ti 3d orbitals; the t_{2g} (composed of the d_{xy}, d_{yz}, d_{zx} orbitals) and the e_g (composed of $d_{x^2-y^2}$ and d_{z^2} orbitals), with the t_{2g} bands being lower in energy by ~ 2 eV, forming the conduction bands. Figure 2.2a shows the band structure of STO, calculated in the 1970s using a combined augmented plane wave (APW) and linear combination of atomic orbitals (LCAO) method [**31**]. It is seen that the dispersion is parabolic, especially near the conduction band minimum at the $\Gamma-$point. Hence the electrons can be considered as *free*, with the appropriate effective mass determined by the band curvature. Figure 2.2b shows a schematic of the STO cubic unit cell in the reciprocal space with the names for the various directions labeled. The bands labeled CB are the three t_{2g} conduction

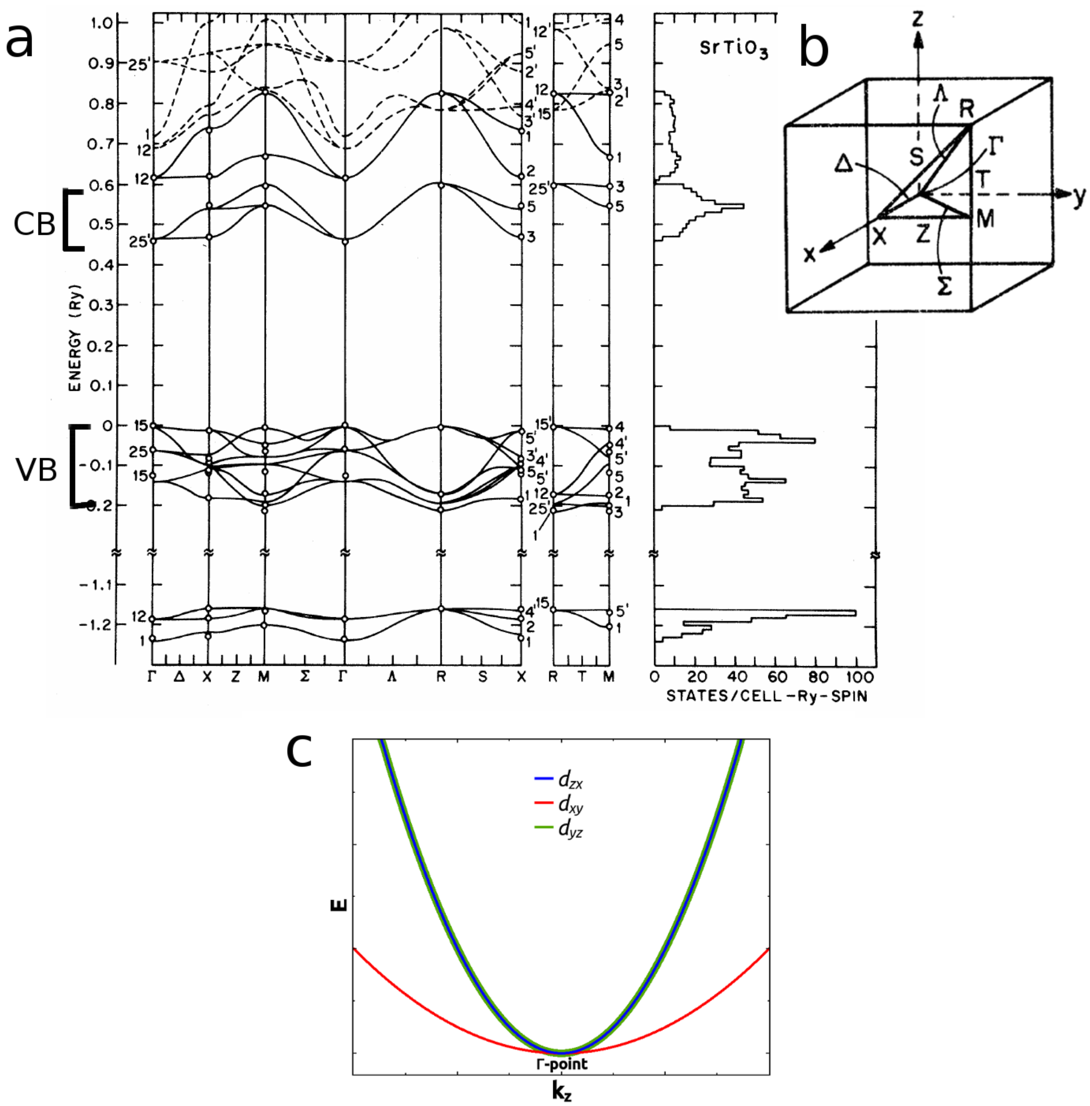

Figure 2.2. **a)** Bulk band structure of STO. The bands labeled CB are the t_{2g} conduction bands, the bands labeled VB are the valence bands. The side panel shows the calculated DOS, for both up- and down- spins. **b)** A schematic of the STO cubic unit cell in the reciprocal space with the names for the various directions labeled. **c)** The three t_{2g} bands in the z direction. While the three are degenerate at the $\Gamma-$point, the d_{xy} band has a large effective mass and the d_{yz} and d_{zx} bands have a smaller mass. **a** and **b** from L. F. Mathiess, Ref. 31

sub-bands. As seen in Fig. 2.2a, all of the three conduction sub-bands are degenerate in some directions of the crystal, for e.g., in the $\Gamma \rightarrow R$ direction, while the degeneracy is lifted in the other directions. Additionally, while the three t_{2g} sub-bands, d_{xy}, d_{yz}, d_{zx}, are degenerate at the $\Gamma-$point, they have different effective masses in the x, y, and z directions. This is expected from the directional nature of these d orbitals, with, for example, the d_{xy} band having a large mass (weak dispersion) in the z-direction due to the small overlap of those orbitals in the z direction, while the d_{yz} and d_{zx} bands are degenerate and have a lighter mass (stronger dispersion). This is shown schematically in Fig. 2.2c.

Figure 2.2a also shows the calculated density of states (DOS) in STO. An important thing to note is that the DOS was calculated by imposing the Kramers degeneracy for spin, i.e., the DOS for up- and down- spins is the same. Hence there is no spin polarization at the Fermi level. In the LAO/STO system, however, magnetism is observed and there is also believed to be finite spin polarization, which implies an imbalance in the up- and down- spin DOS at the Fermi level. Additionally, there is also the strong Rashba spin-orbit coupling in the LAO/STO system [**32**, **33**], which causes further spin splitting of the t_{2g} sub-bands, and a lifting of the Kramers degeneracy. Recent studies on cleaved STO surfaces also show evidence for such spin-splitting due to the spin orbit interactions [**21**]. These issues are further discussed in the following sections.

It was discovered as early as in the 1960s that doping bulk STO by reducing it [**34**], results in $n-$type semiconducting STO. This is because reducing STO introduces oxygen vacancies, each of which contributes two electrons to the system. A useful way to think about oxygen vacancies is in the ionic picture, where if the O atom had been present it would have accepted two electrons from either Ti or Sr to achieve the -2 oxidation state. However, in case of a vacant oxygen site, this transfer of electrons does not happen and as a result there are two additional electrons in the system. These extra electrons occupy the Ti t_{2g} conduction bands discussed above. Similarly any electron-donor dopant in STO, like Nb [**25**], also introduces extra electrons in the system which occupy the conduction bands. Even in the LAO/STO system, the charge carriers, whose origins are different as discussed below, occupy these bands.

As mentioned above, along with conduction, bulk (3D) superconductivity has also been observed in doped STO [**23–29**]. An interesting aspect of such superconductivity is the dependence of the critical temperature, T_C, on the density of carriers [**23, 35**]. Such a dependence is shown in Fig. 2.3. As is seen in the figure, there is an optimum concentration of carriers, $n_C \sim 10^{20}/\text{cm}^3$, at which T_C peaks. This has been explained within the BCS framework by considering intervalley interactions [**23, 35–37**] in many valley materials, like STO. Here "valley" refers to the conduction band minima of the system, which can occur at multiple points of symmetry in the Brillouin zone. The effect of the intervalley coupling is such as to increase the density of states at the Fermi level, which in turn increases the "$N(0)V$" term in the BCS theory. The larger the "$N(0)V$" term, the larger is the gap [**36–39**]. This is in contradistinction to the BCS theory as applied to intrinsic semiconductors, where due to the small DOS at the Fermi level, superconductivity is not favoured. Beyond a certain critical density, the repulsive interactions between the electrons become too large, and the T_C reduces. (For further details see Refs. 36 and

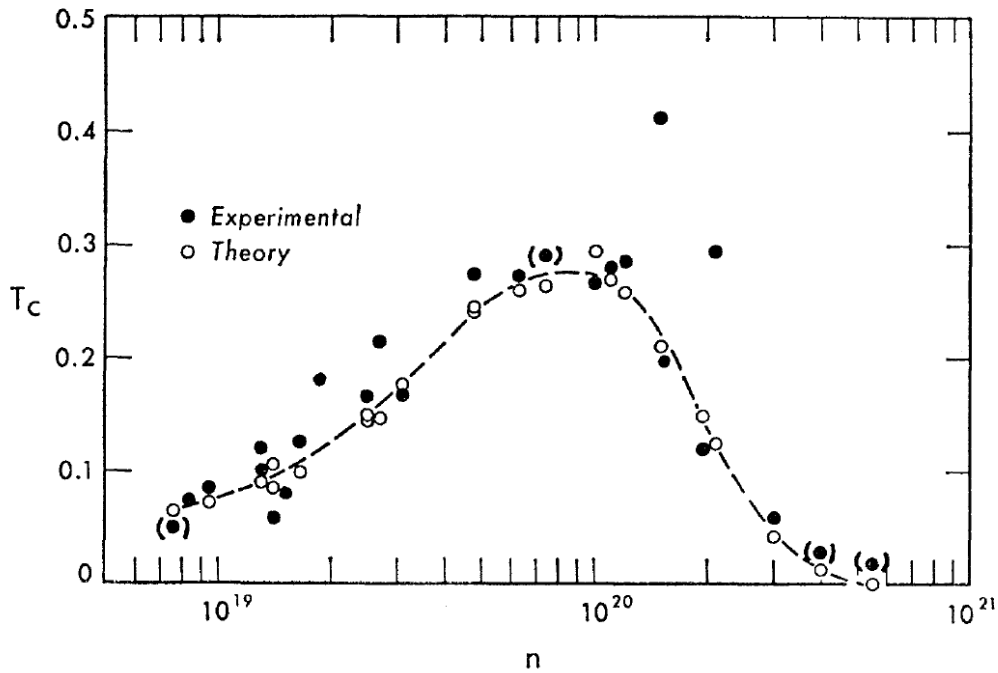

Figure 2.3. Dependence of the superconducting critical temperature, T_C, on the carrier concentration in bulk reduced STO. From Koonce *et al.* [**23**]

37.) Interestingly, such dome-shaped, non-monotonic dependence of T_C has also been observed in the 2D superconductivity of the LAO/STO system, so some of the physics of the reduced STO system carries over into the LAO/STO system. However, in the LAO/STO system, a crucial question is the coexistence of magnetism and superconductivity, which gives rise to the possibility of physics beyond that already developed for the bulk reduced STO system. I address this point in the section covering the coexistence and also in the results chapter.

Next, I discuss the newly discovered sub-band structure at the surface of STO [**18**–**21**], distinct from the bulk band structure, which is believed to host a majority of the charges in the LAO/STO system.

2.2. Surface states in STO

We have already seen the bulk band structure of STO, with the three Ti t_{2g} sub-bands, d_{xy}, d_{yz}, d_{zx}, being degenerate at the conduction band minimum, which happens to be at the $\Gamma-$point (Fig. 2.2). In the last few years, a richer and more complex sub-structure has been discovered in the surface states of bare STO which were found to host a universal 2DEG [**18**–**21**]. The 2DEG is termed universal in the sense that it is independent of the bulk doping of the crystal. These surface states have been discovered by advanced angle-resolved photoemission spectroscopy (ARPES), which is a very effective tool to measure the dispersion relations on the surface of materials. The universal 2DEG in STO has been observed on *in situ* cleaved STO surfaces [**18**] and on *in situ* oxygen annealed surfaces [**20**]. Figure 2.4a shows the results of an ARPES measurement on cleaved STO from 2011, when it was first reported by Santander-Syro *et al.* in Ref.18. In the following I summarize their findings.

Before explaining the data in Fig. 2.4a, I will explain the model of the system as proposed by the authors of Ref.18, as it helps in understanding the structure of the observed bands. Figures 2.4b and c show schematics of the Ti $3d$ bands at the surface of STO. When compared to the bulk band structure of STO at the $\Gamma-$point, as presented in Fig. 2.2, it is seen at first glance in Fig. 2.4 that the proposed surface band structure of

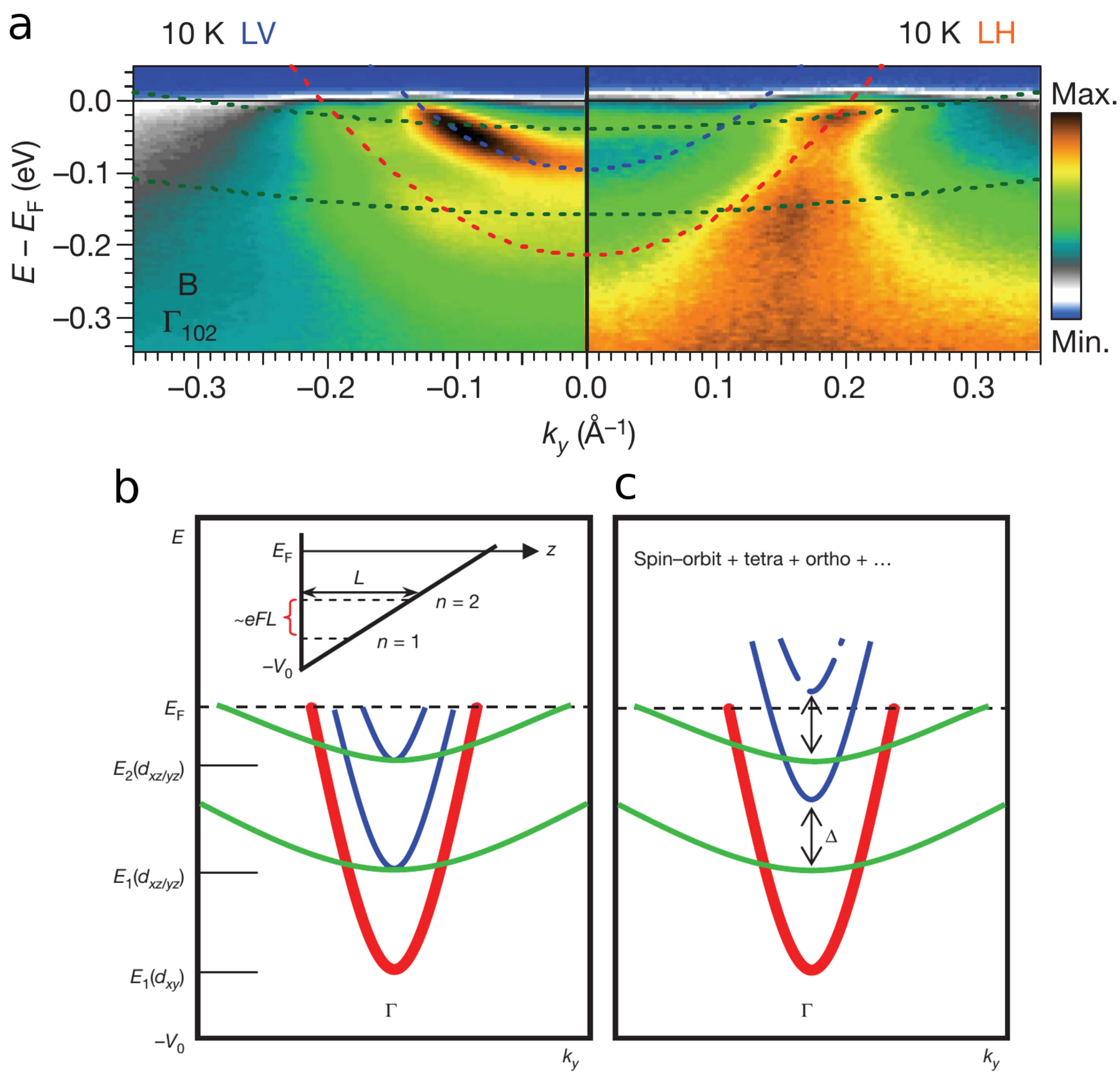

Figure 2.4. **a)** ARPES intensity for the cleaved STO surface along k_y showing a rich sub-band structure. **b)** A schematic of the Ti 3d sub-bands under the effect of a postulated confining potential energy, $-V_0$, at the surface. **c)** The sub-band structure, with the degeneracy lifted between the d_{yz} and the d_{zx} orbitals, under the influence of spin-orbit interactions, or other structural changes. Figure from Santander-Syro *et al.* [**18**]

STO is much more complex. Instead of the three degenerate t_{2g} orbitals at the $\Gamma-$point in the bulk, one now has a multi-level splitting of the bands. In order to explain this substructure, Santander-Syro *et al.* postulate the existence of a finite quantum confining potential energy, $-V_0$, on the surface which lowers the energy of the Ti $3d$ bands at the $\Gamma-$point. This potential decreases in strength along the z direction inside the STO. For simplicity, the shape of the potential well is taken to be linear as shown in Fig. 2.4b. The resulting quantized bands, denoted by $E_n, n = 1, 2, ...$, whose splittings are inversely proportional to their effective masses in the z direction (m_z^*), are also shown in Fig. 2.4b. This implies that the d_{xy} band, which has a large m_z^*, has a negligible splitting (only the first level, $E_1(d_{xy})$, is shown); whereas the d_{yz} and d_{zx} bands have an appreciable splitting (two levels $E_1(d_{yz/zx})$ and $E_2(d_{yz/zx})$ are shown). Note that in Fig. 2.4b, the bands are plotted along k_y (the direction in which the data is shown), and so the bands which are heavy along z, like the d_{xy} band, will appear as light in the figure. Additional interactions, like the Rashba spin-orbit coupling [**59**, **60**], which can be appreciable at the surface, can further lift the degeneracy of the d_{yz} and d_{zx} bands as shown in Fig. 2.4c.

With the above model of the surface states in STO in mind, one can understand the data shown in Fig. 2.4a. The figure shows the measured ARPES intensity around the $\Gamma-$point at the surface of STO in the k_y direction. One can identify four distinct bands with different dispersions around the $\Gamma-$point, very different from the bulk picture (Fig. 2.2). There are two light mass bands (stronger dispersion) and two heavy mass bands (weaker dispersion), indicated by dashed lines in the figure. The lowest band (dashed red line) is identified as the $E_1(d_{xy})$ band discussed above, which has a light mass in the y

direction. The other light band (blue dashed line) is identified as the $E_1(d_{yz})$ band which is split from the $E_1(d_{zx})$ band, possibly due to spin orbit interactions. The two heavy bands are $E_1(d_{zx})$ and $E_2(d_{zx})$ (green dashed lines). The resultant Fermi surface from these measurements, projected onto the xy plane, is shown in Fig. 2.5. As can be seen, all the three bands, d_{xy}, d_{yz}, d_{zx}, contribute to the electrons at the Fermi surface. From the area of the Fermi surface, a universal areal density of $n_{2D} \approx 2 \times 10^{14}/\text{cm}^2$ is estimated at the surface of STO. A similar Fermi surface has also been proposed theoretically for the LAO/STO interface using the tight binding method [**48**], suggesting that the electrons at the LAO/STO interface occupy these universal surface states in STO.

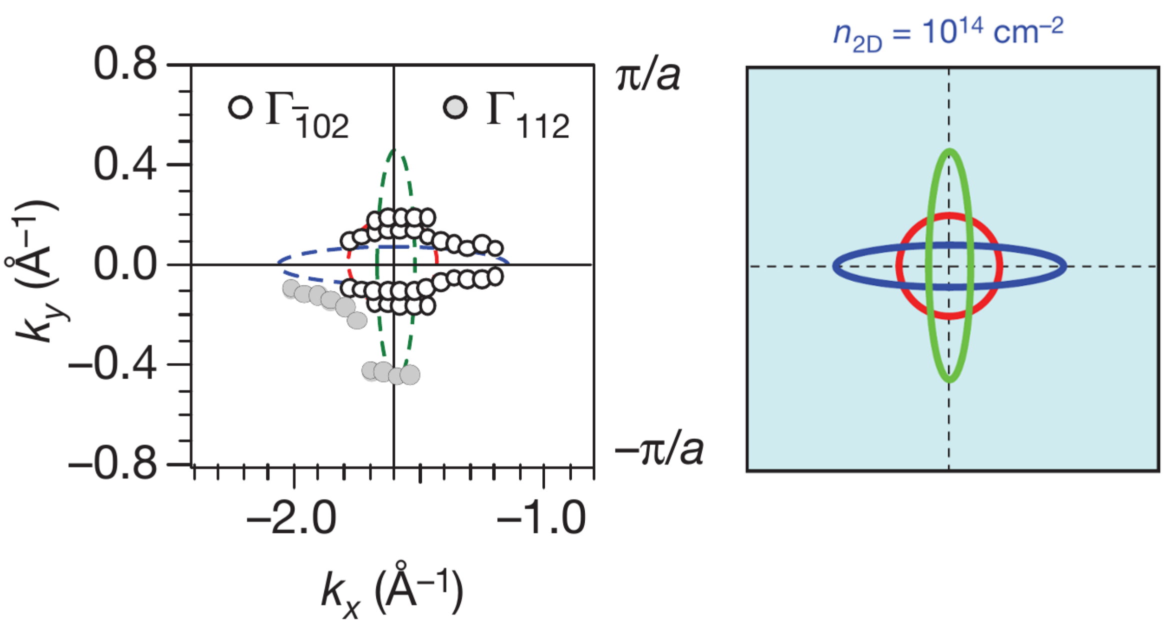

Figure 2.5. The Fermi surface of the 2DEG at the surface of STO, as constructed from ARPES data. A schematic is also shown for clarity. From Santander-Syro *et al.* [**18**]

It should be noted that there exist the so-called Shockley-Tamm surface states, different from the bulk Bloch states, at the surface of any material, at its interface with vacuum [**61**, **62**]. These states arise due to a mismatch in the crystal potential experienced by the electrons at the surface, with their wave functions found to be exponentially decaying into the bulk of the crystal. Such states were shown to have sub-gap energies in materials with a band gap [**63**]. The exact energies and the decay lengths of the Shockley-Tamm states depend on the crystal structure and other material properties [**63**]. The surface states of STO described above could also be viewed as the Shockley-Tamm surface states of STO, although Santander-Syro *et al.* make no mention of that in their paper. They attribute their confining potential energy to the accumulation of positive charge from the oxygen vacancies at the surface [**18**]. This issue is addressed in more detail below.

In the next section, I describe the various mechanisms of charge formation at the LAO/STO interface.

2.3. Mechanisms of charge formation at the interface

While STO "hosts" the mobile charge carriers found in the LAO/STO system, their origins are thought to be from multiple sources. Below I discuss the three principal mechanisms proposed to explain the existence of charge carriers at the interface. After a description of the mechanisms, I will discuss the strength of their relative contributions in the system. I will then compare and contrast the physics of charge formation at the

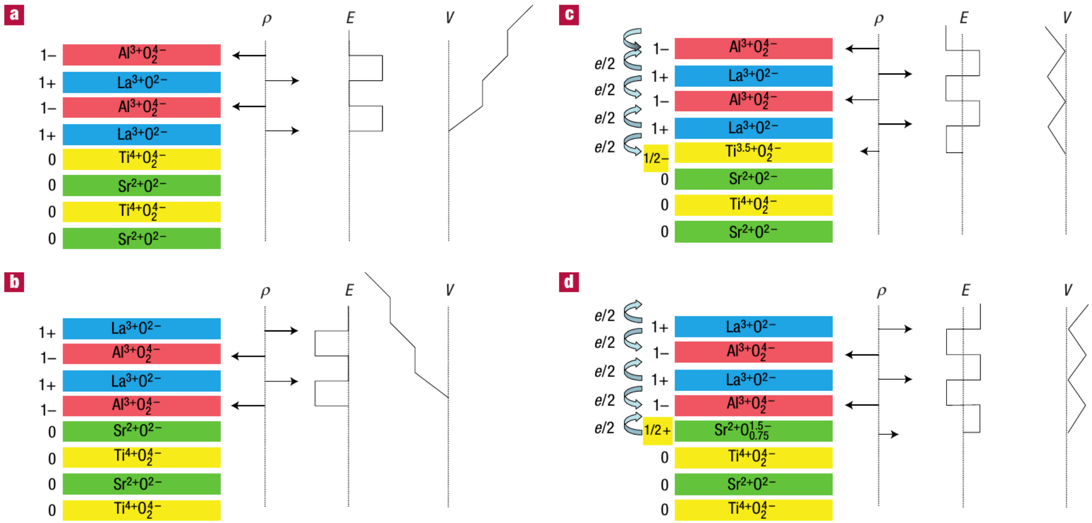

Figure 2.6. **Polar discontinuity scenario.** Electronic reconstruction at the LAO/STO interface due to the polar catastrophe scenario. **a,** The unreconstructed interface, LaO/TiO_2. The charge mismatch creates a non-negative electric field (E), leading in turn to an electric potential (V) that diverges with thickness. **b,** At the AlO_2/SrO interface, the potential diverges negatively. **c,** The divergence catastrophe at the LaO/TiO_2 interface can be avoided if half an electron is added to the last Ti layer. This produces an interface dipole that causes the electric field to oscillate about zero and the potential remains finite. The upper free surface is not shown, but in this simple model the uppermost AlO_2 layer would be missing half an electron, which would bring the electric field and potential back to zero at the upper surface. The actual surface reconstruction is more complicated [**40**]. **d,** The divergence for the AlO_2/SrO interface can also be avoided by removing half an electron from the SrO plane in the form of oxygen vacancies. Figure and caption from Nakagawa *et al.* [**43**]

LAO/STO interface with that at the surface of bare STO.

2.3.1. Polar discontinuity scenario

Being perovskite structures, both LAO and STO are layered materials, as seen in Fig. 1.2. In the (001) orientation, in STO there exist alternating planes of $(Sr^{2+}O^{2-})^0$ and

$(Ti^{4+}O_2^{4-})^0$, while in LAO there exist alternating planes of $(Al^{3+}O_2^{4-})^-$ and $(La^{3+}O^{2-})^+$ [**40**]. This makes STO a non-polar material, while LAO is a polar material with a dipole moment between the $(Al^{3+}O_2^{4-})^-$ and $(La^{3+}O^{2-})^+$ layers. It should be noted that the word *polar* here is used in a strict and limited sense to characterize a material which has the alternative charged layers as described above for LAO in the (001) orientation. It should not be confused with the use of polar as a description of any old ionic solid, under which definition even STO falls. It should also be emphasized that the description given above of the arrangement of atomic planes in LAO and STO is only valid in the (001) direction. Since all of my data were taken on LAO/STO samples with the (001) orientation, we will restrict our discussion to a description of the system in that orientation.

As can be seen in Fig. 2.6, the epitaxial growth of a polar material, LAO, on a non-polar material, STO, leads to a discontinuity of electric potential at the interface, and its subsequent divergence as the LAO thickness is increased. Such a build up of potential actually happens at the surface of any polar material, even at its interface with vacuum, which results in its surface reconstruction by a compensation of the surface charges. The surface reconstruction happens by a loss of stoichiometry on the surface, where multiple ions can be adsorbed/desorbed, including of foreign species, so as to compensate for the surface charge. However, for any odd polar material, such a reconstruction does not necessarily result in mobile charges at the surface, due to the lack of states available for them. In contrast, at the interface of LAO/STO, this potential divergence is reconciled by electronic reconstruction at the interface, where there are mobile electron states available in the Ti t_{2g} bands of STO. In the polar catastrophe model, this reconstruction is accomplished by a transfer of half an electron per interfacial unit cell (for the $n-$type interface) from the top LAO surface to the interface. The excess electrons in the Ti t_{2g} bands at the interface result in changing half of the Ti^{4+} states to Ti^{3+} [**41**, **42**]. For the $p-$type interface, formed when LAO is grown on SrO terminated STO, opposite sign charges are required to compensate for the potential divergence, which is now reversed in polarity (see Fig. 2.6**b**). However, accessing the Ti^{5+} state is difficult in this structure, and hence oxygen vacancies close to the interface are created to provide the excess charge [**2**]. Since this does not result in itinerant holes, the p-type interfaces remain insulating, as has been observed [**2**].

A useful way of thinking about the polar catastrophe mechanism is to view it in the familiar band bending picture at semiconductor heterointerfaces [**44**]. We recall that in the simple case of the $pn-$junction, the transfer of *mobile* charges across the interface gives rise to the depletion layer and the associated opposite polarity "space charges" in the $p-$ and $n-$type materials. It is this space charge that causes the band bending at the $pn-$junction [**45**].

Similar band bending has also been observed experimentally in the LAO/STO system [**46**,**47**]. A schematic of the band bending at the LAO/STO interface is shown in Fig. 2.7, which is taken from Ref. 46. Unlike in the $pn-$junction, where the "space charge" builds up due to a transfer of mobile charges, in the LAO/STO system the "space charge" is formed due to the polar nature of LAO. As shown in Fig. 2.7, there is a build up of a positive “space charge” in the $(LaO)^+$ layer at the interface. This results in an electric field, and hence a electric potential, that extends into the STO. The shape of this potential can be determined by solving the Poisson equation in STO, with the boundary condition that the potential is zero far enough inside the STO. The shape of the potential gives rise to the band bending in the STO, with both the conduction and valence bands bending downwards (the electron energy bands have the opposite sign to the surface potential, due to the negative charge of the electron, i.e., if the potential is ϕ, the band energies will be $-e\phi$). Once the conduction band minimum of STO drops below the chemical potential for electrons in the system, it will start to get filled. In the polar catastrophe scenario, these electrons are sourced by the topmost layer of LAO. The charge left behind on the top surface of LAO may get compensated by surface reconstruction, but does not result in mobile carriers at the surface. The strength of the confining potential in STO is determined by photoemission spectroscopy and theoretical efforts to be $\sim 0.2 - 0.3$ eV [**46**–**48**]. The reported extent of the confining potential in STO varies from 2 to 50 unit cells, i.e., 0.8 to 20 nm [**4**, **18**, **43**, **47**]. While these numbers vary a little with the thickness of LAO and other factors, like the number of oxygen vacancies, they remain around the range quoted above for most of the samples studied.

A major consequence of the polar catastrophe mechanism is the dependence of the electrical conductivity of samples on the thickness of LAO grown, as the potential build-up in LAO is directly proportional to its thickness. If a few mono-layers thick LAO is grown, then the potential will be small enough to not require an electronic reconstruction at the interface of the kind described above. This has indeed been observed experimentally [**4**].

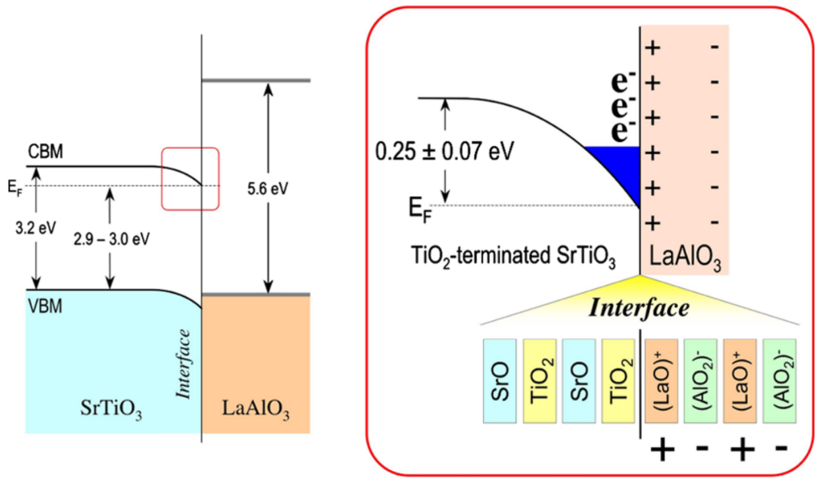

Figure 2.7. The band bending at the LAO/STO interface, induced from experimental *in situ* photoemission spectroscopy data. [**46**]

It was observed that the $n-$type interface is conducting only above a critical thickness of four mono-layers of LAO. Evidences against the polar catastrophe mechanism are, (i) the independence of the carrier density on the thickness of LAO layers, above the critical thickness of four mono-layers, (ii) observation of conductivity in non-polar LAO/STO interfaces, for e.g., at the (110) oriented interface [**49**], and (iii) the observation of carrier densities much below the critical density ($n_C \approx 3 \times 10^{14}/\text{cm}^2$) needed to satisfy the polar catastrophe [**4**], including in the samples presented in this thesis. It should also be noted that the density of carriers required to compensate the polar discontinuity at the interface is less than the experimentally measured carrier densities as reported in a few of the publications [**50, 51**], implying sources of charge other than this mechanism also contribute to the interface conductivity. I discuss these other sources next.

2.3.2. Role of oxygen vacancies

Occurrence of oxygen vacancies in perovskites is not uncommon, especially in STO [**52**]. Typically, in perovskite oxides, oxygen vacancies result in the donation of two negative charge carriers in the material. Oxygen vacancies can be created during growth, or during post-growth fabrication of samples, by the bombardment of energetic ions at the interface. There have been many studies that report the dependence of the electronic properties of the interface on the oxygen partial pressure during growth [**7**, **50**, **51**]. Changing the oxygen partial pressure has been shown to give rise to a range of behaviours at the interface: insulating, metallic, and magnetic [**7**]. Since oxygen is a donor of electrons, it is natural to expect that the samples grown in high oxygen partial pressure result in relatively lower conductivities, while those grown in lower partial pressures result in samples with higher conductivities. Broadly speaking, this is what has been observed as seen in Fig. 2.8. As in the polar discontinuity scenario, the excess electrons due to the oxygen vacancies also result in the creation of the Ti^{3+} states in addition to the existing Ti^{4+} states, suggesting a contribution to magnetism at the interface.

2.3.3. Ionic "interdiffusion"

Another scenario suggested for charge generation at the interface is the so called "ionic interdiffusion". Wilmott *et al.* reported the intermixing of the various cations (La, Al, Sr, and Ti) at the interface using surface X-ray scattering [**53**]. Based on these observations the origin of conductivity was attributed to the formation of the metallic, bulk-like solid solution of $La_{1-x}Sr_xTiO_3$ at the interface. Like in the two cases above, this mechanism

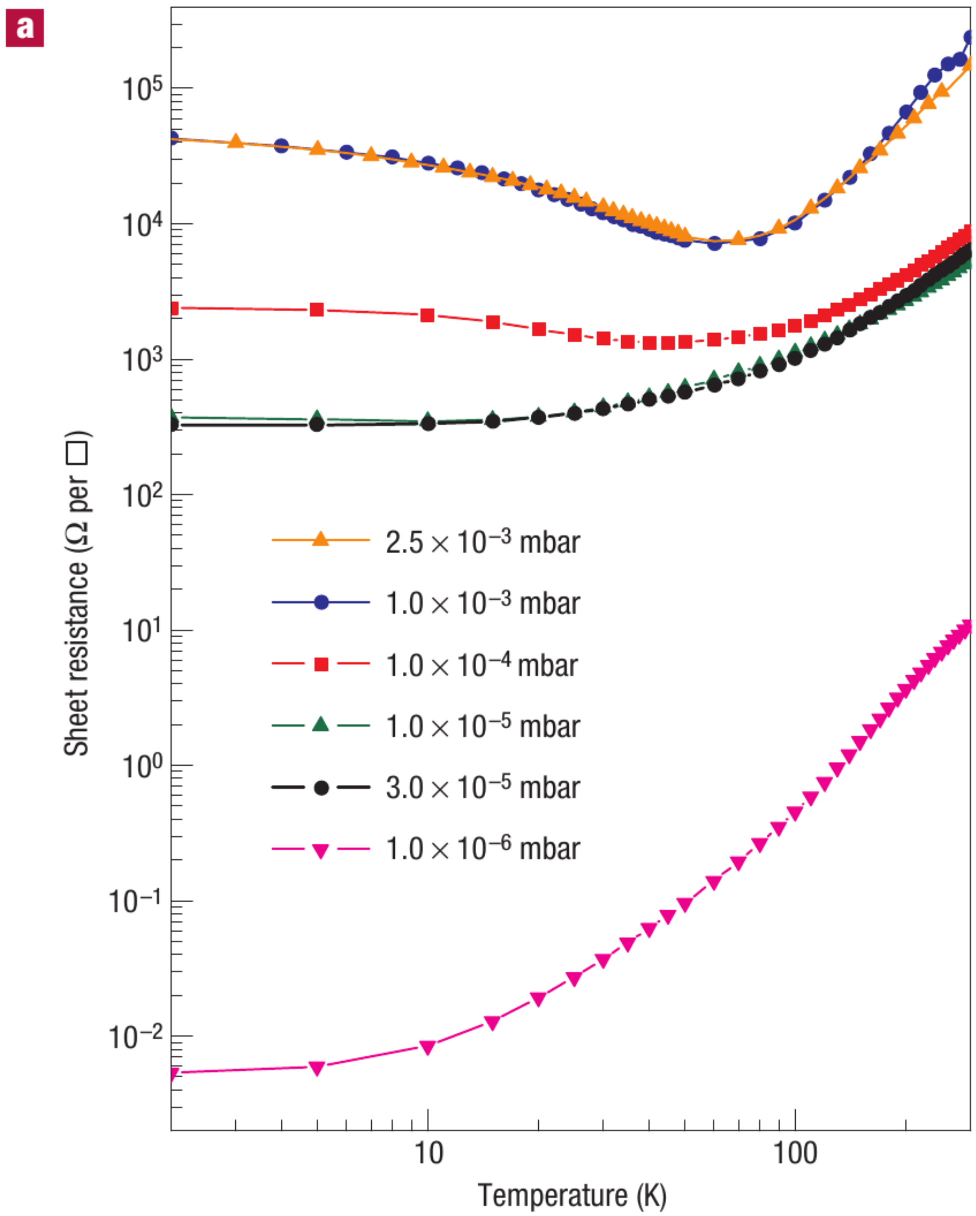

Figure 2.8. Dependence of electrical transport properties on oxygen partial pressure during growth. Adapted from Brinkman *et al.* [**7**]

also results in the formation of multi-valent Ti ions at the interface, Ti^{3+} and Ti^{4+}. However, this scenario does not agree with the observation of the critical thickness of LAO (4 unit cell) for metallic conduction.

Apart from the three major sources for charges mentioned above, various other sources have also been used to induce charge at this interface. Principal among these is the use of electric field using a gate voltage on the STO. This has the effect of populating/depopulating the interface with charges, like in a field effect transistor. In my experiments I use this extensively to change the density of charge carriers in my samples. Utilizing the fact that the polarization density, P, in a linear dielectric is proportional to the applied electric field, $P = \epsilon_0 \chi E$, one can calculate the induced charge at the interface as a result of gating. Here, ϵ_0 is the permittivity of vacuum, χ is the dielectric susceptibility, and E is the external applied field. With the typical numbers used in our experiments, $E \sim 2 \times 10^5$ V/m and $\chi \sim 10^4$ [**22**], I calculate the induced surface charge density due to an applied back gate voltage to be, $n_{ind} \sim 10^{13}/\mathrm{cm}^2$. This is close to what we observe in our experiments. We address this issue further in the results chapter. Charge can also be induced at the interface due to ionic adsorption at the *surface* [**54**,**55**], which transfers charge to the interface. Another method is to actually *write* a conducting channel at the interface using a conductive AFM tip [**9**]. In this method the conductive AFM tip is thought to induce positive charges at the top surface of LAO, which in turn attracts charges at the interface, similar to localized gating from the top [**56**, **57**].

Currently, there is no single accepted mechanism for the creation of charge at the interface. In fact, while there are no theoretical predictions for hole-like charges at the interface, there is some experimental evidence for a hole channel existing at the interface [**58**]. As discussed in the results chapter, we also see evidence for hole-like conduction at the interface, in addition to the $n-$type conduction. The three principal mechanisms discussed above are all believed to contribute to varying degrees to the conductance of a particular sample. A significant consequence of these multiple contributions to charges at the interface is the possibility of forming local inhomogeneities. These intrinsic inhomogeneities would form depending on which scenario is dominant locally, subject to the constraint of local charge neutrality [**40**].

2.3.4. Similarities and differences between the LAO/STO interface and bare STO surface

No matter what the source of charge is at the LAO/STO interface, all of the charges reside in the Ti t_{2g} conduction bands within several nanometers of the interface, forming the 2DEG [**2**, **4**]. In the following I lay out the similarities and differences between the charge formation models proposed for the LAO/STO interface and those proposed for bare STO surface.

The confining potential at the surface STO is analogous to the confining potential at the LAO/STO interface discussed above in the section on polar discontinuity scenario (Fig. 2.7). Unlike in the LAO/STO case, where the source of the potential was the positive charge from the interfacial $(\mathrm{LaO})^{+}$ plane, here the source of the potential is thought to be the positive charge due to the oxygen vacancies at the surface [**18**]. The cleaving of

STO surface results in the generation of a lot of oxygen vacancies which act as electron donors. Thus, according to Santander-Syro *et al.*, oxygen vacancies perform the dual role of supplying the electrons for the universal 2DEG, and also form the localized, positive surface charge layer, which is the source of the confining potential for the electrons. Like in the LAO/STO case, here also the strength of the confinement potential is, $V_0 \sim 0.3$ eV. The maximum extent of the confining potential in STO is measured to be $L \leq 4$ nm, which is also similar to the extent of the 2DEG in LAO/STO as measured by hard X-ray photoelectron spectroscopy [**64**]. (Although a range of 2DEG thicknesses have been reported in the LAO/STO system [**4**, **43**, **51**, **53**, **65**, **66**] using different methods, most of them restrict the extent of the 2DEG to $d < 20$ nm.)

Therefore it is very likely that the Ti $3d$ states at the LAO/STO interface have a lot of the same characteristics as the surface states in bare STO. We can reasonably assume that the in the LAO/STO system, the d_{xy} band, being the lowest in energy, is the first to be occupied as charges get generated at the interface (no matter what their source). That the d_{xy} band is the lowest in energy is inferred from tight binding calculations of Ti bands in STO, as d_{xy} states have the highest overlap (i.e., a large hopping term) in the xy plane, which lowers their energy with respect to orbitals like d_{yz} and d_{zx} which have a z character [**48**]. This is especially true for the first TiO_2 layer next to the interface. Beyond that there is still considerable debate about the hierarchy of bands in terms of their occupation at the LAO/STO interface. If the surface states of STO as described above are present unaltered at the LAO/STO interface, then the next occupied level will be of the d_{zx} character. However, some theoretical work suggests that it is the second TiO_2

layer d_{xy} band that is occupied after the lowest energy, first layer d_{xy} band [**48**, **67**, **68**]. Some of the factors that influence this hierarchy in energy of the various bands near the interface are screening from the electrons already present, dielectric constant of STO and its dependence on an external field (as generated by the confining potential, for example). In any case, it is generally agreed that the Fermi surface at the LAO/STO interface, like in bare STO, has contributions from all the three Ti t_{2g} sub-bands.

Another similarity between the bare STO surface and the LAO/STO interface is the importance of Rashba-type spin-orbit interactions in determining the 2DEG properties. It is useful to recall that the Rashba-type spin-orbit interactions arise due to the breaking of inversion symmetry by the surface/interface in such materials. The confining electric field at this boundary acts as a magnetic field in the rest frame of the electron, and hence couples to its spin. This explanation is similar to the one given for atomic spin-orbit coupling, except that at surfaces/interfaces the strength of the electric field can be quite large and has a significant effect on the electron energies. It was shown by Rashba [**59**,**60**], that the inclusion of spin-orbit interactions in the Hamiltonian ($H_R = \alpha(\sigma \times k) \cdot \hat{z}$, with the interface plane being perpendicular to $\hat{z}$) of an electron at a surface/interface results in a spin-splitting of is bands into two different branches,

$$E^{\pm}(k) = \frac{\hbar^2 k^2}{2m} \pm \alpha k = \frac{\hbar^2 k^2}{2m} \pm \Delta_{SO} \tag{2.1}$$

where, α is a constant dependent on the strength of the electric field and other material parameters. Here each branch is locked to a particular spin and thus in materials with a large α, one can have a large spin splitting at the Fermi surface. Both STO [**21**] and

LAO/STO [**32**, **33**] have been reported to show a sizable spin-orbit coupling term.

While there are a lot of similarities in the 2DEG found on the surface of bare STO and that found at the LAO/STO interface, there are also some crucial differences. First, the sources of electrons in the 2DEG at the LAO/STO interface are multiple, as described above, whereas on the surface of STO it is the oxygen vacancies that are thought to provide the electrons [**18**]. Second, although magnetism has recently been reported on the surface of bare STO [**21**], the coexistence of superconductivity and magnetism has not been observed yet, the study of which is one of the principal foci of this thesis.

In the next section, I discuss the theoretical models proposed to explain the coexistence of superconductivity and magnetism at this interface.

2.4. Proposed models for the coexistence of superconductivity and ferromagnetism

Ever since the discovery of the 2DEG in this system, various theoretical efforts have focused on explaining the observed electronic transport behaviour in it. These include the initial band structure calculations [**41**, **42**, **48**, **69**–**71**], all of which strove to explain the creation of charge at the $n-$ type interface as seen experimentally. It was also found in these initial calculations that the electrons occupy the Ti $3d$ bands in STO at the interface, whose degeneracy is lifted by the crystal field (into e_g and t_{2g} orbitals) and also due to the quantum-confined nature of the gas, as described above. Consequently, in these models of the interface gas, the lowest energy band is formed by the $3d_{xy}$ orbitals followed by the two higher energy bands $3d_{xz}$ and $3d_{yz}$, whose increased energy relative to the $3d_{xy}$ band is due to their lobes oriented perpendicular to the interface [**48**]. This band picture is shown schematically in the inset of Fig. 2.9. Finally, in these models, the d_{xy} band in the TiO_2 layer nearest the interface is distinct from the d_{xy} bands in the bulk, in that it is confined to the interface, whereas the d_{xz} and d_{yz} bands extend further into the STO. The two e_g orbitals are even higher in energy, and are not populated. While all of the theoretical efforts cited above tried to explain the mechanism of formation and the associated band structure of charge in this system, not much effort was devoted to explaining the nature of the superconducting state that had been observed in some of the samples until then [**5, 6**]. For the magnetism, the calculations of Pentcheva and Pickett [**41**] predicted a ferromagnetic state at the $n-$type interface which was subsequently also observed [**7**].

There certainly was not any indication from theoretical studies for the coexistence of these two phenomena, and it was not until this coexistence was observed experimentally [**10–12**] that some theories were put forth to explain this. In order to explain this coexistence, some of the major questions that need to be answered are, (i) do the two phenomena originate in separate energy bands or the same band, (ii) is the ferromagnetism caused due to itinerant electrons, (iii) is the superconducting order parameter BCS-like [**38**] with $s - wave$ symmetry, or does it have more exotic symmetry, and (iv) how are both phenomena affected by the three principal mechanisms of charge formation at the interface discussed above. Given that the experimental results on different samples have shown different behaviour, the theoretical efforts to describe these experimental results also lead to different, and sometimes even contradictory, conclusions. Below I will go over two different theoretical efforts, one by Michaeli *et al.* [**72**] and another by Pavlenko *et al.* [**73**]. These two works present differing models of the system and also, unsurprisingly, arrive at differing conclusions about the nature of the two phenomena.

2.4.1. Model of Michaeli *et al.*

I will first summarize the results of Michaeli *et al.* [**72**]. In order to explain the coexistence of superconductivity and ferromagnetism at this interface, they propose a Fulde-Ferrel-Larkin-Ovchinikov (FFLO) [**74**] state for the Cooper-pair condensate, where the Cooper pairs exist at a finite momentum, which coexists with the ferromagnetism. Building on the theory first proposed for a 2D surface superconductor by Barzykin and Gor'kov [**75**], Michaeli *et al.*, show that the increased Rashba spin-orbit coupling at this interface gives rise to a FFLO state for the electronic system. They posit that the ferromagnetism and superconductivity arise in separate bands, and the effect of the ferromagnetism on the superconductivity is long-range and passive, i.e., the field due to the ferromagnet acts as an external field on the superconductor, which is sufficient to explain the observed experimental results [**10–12**]. I now give a brief overview of their theory.

In their model of the system, the electrons from the polar catastrophe mechanism reside in the first Ti $3d_{xy}$ band at the interface and are localized, whereas all the mobile electrons (arising due to any other means such as gate voltage, oxygen vacancies, etc) start filling up the d_{xz} and d_{yz} bands, which extend deeper into the STO (see Fig. 2.9).

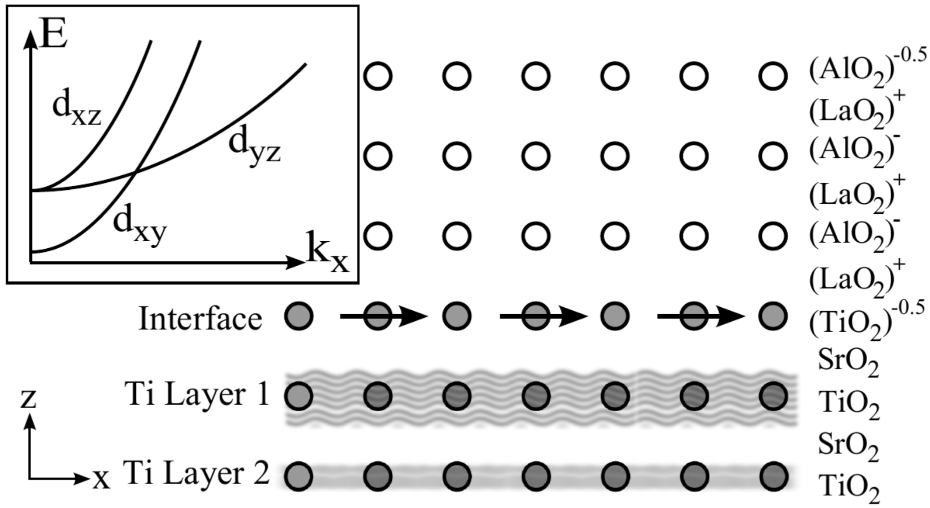

Figure 2.9. Schematic depiction of the LAO/STO oxide interface structure. Filled and empty circles depict Ti and Al ions. Half a charge per unit cell is transferred to the inter- face TiO_2 layer. This charge localizes and orders magnetically (shown as arrows on the interface layer) via exchange polarization of conduction electrons on the subsequent Ti layers (shown as wavy cloud in Ti Layers 1 and 2). Inset: Dispersion of electron bands arising from $3d$ orbitals on Ti layers near the interface. The d_{xy} bands are polarized via exchange with the localized interface layer. Superconductivity occurs in d_{xz} and d_{yz} bands which have lower magnetic exchange and stronger spin-orbit coupling. From Michaeli *et al.* [**72**].

A crucial part of their model relies on the reports of a large Rashba spin-orbit coupling term, Δ_{SO}, which can be tuned with a gate voltage [**32, 33**]. They also calculate this spin-orbit coupling to be enhanced in the d_{xz} and d_{yz} bands compared to the d_{xy} band. It is this increased Δ_{SO}, which causes an increase in the Pauli pair-breaking field in the 2D superconductor [**75, 76**] and hence can support the formation of a condensate despite the presence of a large exchange field due to the ferromagnet.

They show that the ferromagnetic state originates in the first $3d_{xy}$ band from the interface. The electrons in this band are localized on alternate Ti sites and form a very narrow band. The d_{xz} and d_{yz} bands form the conduction band of mobile electrons, which mediate the Ruderman-Kittel-Kasuya-Yosida (RKKY) interactions between the localized d_{xy} spins. The localized moments couple with their neighbours ferromagnetically via the Zener kinetic exchange mechanism [**77**] by polarizing the conduction electrons. Applying this mechanism to this system, Michaeli *et al.* find a highly spin polarized d_{xy} band which accounts for the ferromagnetism seen in this system. They also find that the d_{xz} and d_{yz} bands are also spin-polarized but to a much smaller extent than the d_{xy} band.

For the superconducting state, they assume the conventional electron-phonon coupling giving rise to a Cooper-pair condensate. As mentioned above, for a stable superconducting state they rely on the increased Pauli pair-breaking field due to the large spin-orbit coupling in this system [**75, 76**] to sustain superconducting correlations, despite a large Zeeman splitting field from the ferromagnet. This increase in Pauli field is arrived at within the BCS framework by Barzykin and Gor'kov [**75**] by incorporating a strong Rashba spin-orbit term in a 2D surface superconductor. (For the full details of the calculation, one is referred to their paper [**75**].) Due to the large spin polarization of the d_{xy} band, this effect is still not strong enough to support superconducting correlations in that band. However, in the d_{xz} and d_{yz} bands, they find that Cooper pair correlations can be sustained due to the enhanced Pauli pair breaking field, owing to their much smaller spin polarizations and exchange fields. As found by Barzykin and Gor'kov [**75**], Michaeli *et al.* also find a FFLO state with a finite Cooper-pair momentum. They show that this FFLO state is robust

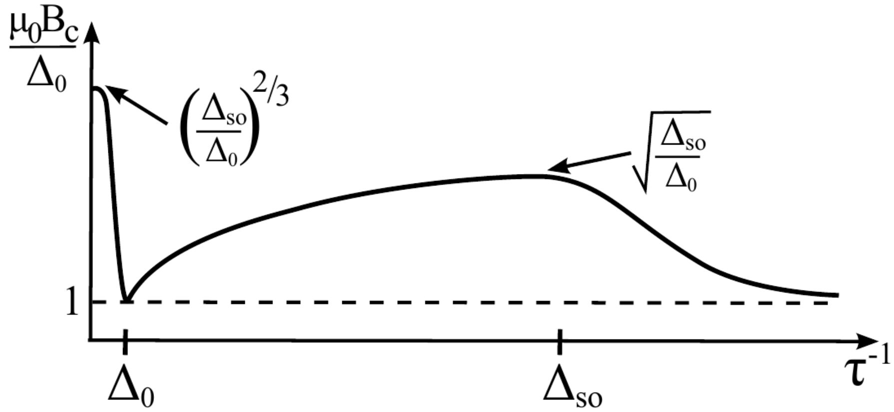

Figure 2.10. Pauli pair breaking filed measured in units of bare SC gap Δ_0 as a function of disorder strength τ^1. The dome in the pair-breaking filed arises due to the change in disorder strength, which can be tuned by a gate voltage. From Michaeli *et al.* [**72**].

against disorder, which in this system can be tuned by the application of a gate voltage. They also explain the observed superconducting dome in this system [**6**, **10**] based on the dependence of Δ_{SO}, and hence the Pauli pair breaking field, on the gate voltage (See Fig. 2.10).

The main conclusion from the work of Michaeli *et al.* is that they predict uniform ferromagnetic and superconducting phases, which exist throughout the sample. The ferromagnetism and the superconductivity reside in separate bands, with separate origins of charge for both the bands.

I will now summarize the results of Pavlenko *et al.* [**73**], which propose a highly non-uniform ferromagnetic phase, which is thought to arise from the inhomogeneous distribution of oxygen vacancies at this interface.

2.4.2. Model of Pavlenko *et al.*

As mentioned above, the central hypothesis of Pavlenko *et al.* is the origin of ferromagnetism being attributed to electrons arising from oxygen vacancies in the system. Employing density functional theory calculations, they show that the ferromagnetism is induced in the Ti $3d$ bands due to the spin splitting of the bands caused by the excess charge density introduced locally by an oxygen vacancy [**78**]. This spin splitting is thought to occur due to a ferromagnetic interaction between the localized moments associated with the excess localized electrons created by the oxygen vacancies, mediated by a super-exchange like mechanism [**78**]. They do the DFT calculations of LAO/STO/LAO supercells with 4 unit cell thick LAO and varying thicknesses of STO from 1.5 to 6 unit cells. They artificially introduce oxygen vacancies in the structure (see Fig. 2.11) and calculate the density of states (DOS) for the various Ti $3d$ orbitals. These are shown in Fig. 2.12. As can be seen in the figure, there is a net spin polarization in the system with oxygen vacancies (the difference in up- and down-spin DOS gives rise to a net spin polarization), compared to the pure system. In their model, this is the cause for a robust ferromagnetic state in this system. This difference arises due to the exchange splitting of the spin bands due to the enhanced charge density, contributed by the oxygen vacancy.

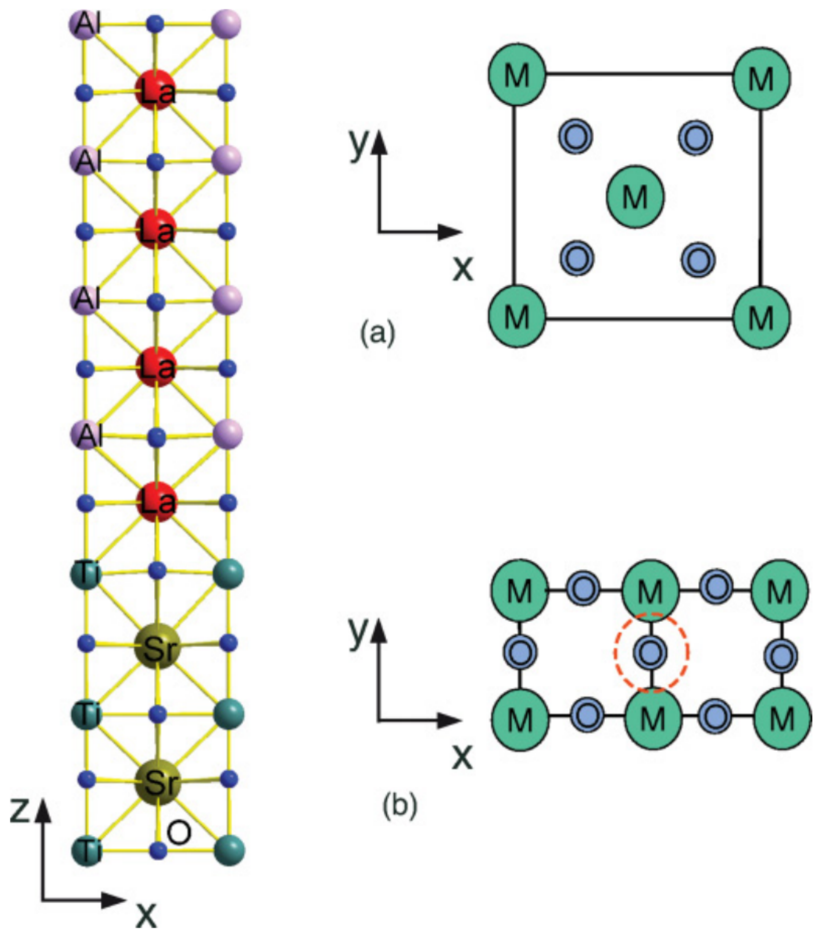

Figure 2.11. Schematic view of the LAO/STO heterostructure. The supercell contains a 4-unit-cell-thick LAO layer deposited on a 2.5-unit-cell-thick STO slab. The full supercell consists of two symmetric parts of the depicted structure and a vacuum layer of 13 Å. The structures on the right-hand side show (a) a projection of the supercell of STO/LAO on the (x,y) plane of TiO_2, and (b) a M_2O_4 (M = Ti,Al) plaquette generated for the study of the system with O vacancies. The position of an O vacancy is identified by a red dashed circle. From Pavlenko *et al.* [**73**].

Pavlenko *et al.* introduce the oxygen vacancies in the first TiO_2 plane at the interface. They find that this induces a moment of $\sim 0.33\mu_B$ on the Ti atom next to the vacancy

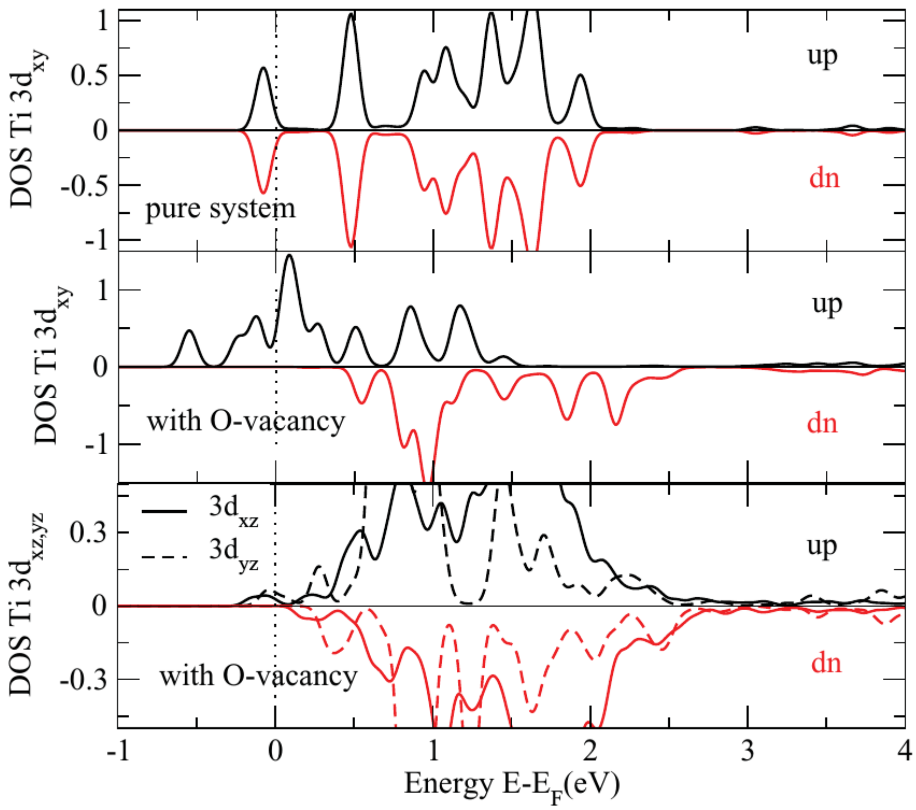

Figure 2.12. Projected DOS (in eV^{-1}) for $3d$ (t_{2g}) states of the interfacial Ti in the supercell containing 4-unit-cell-thick LAO layers and a 4-unit-cell-thick STO layer. DOS in the pure system and in the system with one O vacancy (25%) per supercell area in the interfacial TiO_2 layer are shown for comparison. The vertical gray line denotes the Fermi level. From Pavlenko *et al.* [**73**].

and a moment of $\sim 0.34\mu_B$ in the next nearest Ti atom. They also find a magnetic moment on the AlO_2 surface plane of $\sim$-$0.18\mu_B$, aligned anti-parallel to the interface Ti moments. Due to the nature of their supercell, they over-estimate the density of their oxygen vacancies compared to that found in actual samples. However, they claim that the ferromagnetic coupling of the Ti atoms at the interface will be maintained in areas of the sample which are rich in oxygen vacancies. An important finding of their calculations is the energetic favourability of an "inhomogeneous" distribution of oxygen vacancies. They get that by calculating the energies of a system with a homogeneous arrangement of oxygen vacancies, i.e., one vacancy per each Ti atom, and that of a system with one vacancy near one Ti atom in a 2×1 plaquette and no vacancy near the adjacent Ti atom (see Fig. 2.11). They get an energy gain of 0.25 eV per interface unit cell for the inhomogeneous configuration. This corroborates the observed ferromagnetic puddles as seen by Bert *et al.* [**11**]. However, this fails to explain the observed hysteresis in the magneto-resistance as seen by us [**10**, **79**] and others [**80**].

They analyze their ferromagnetic ordering in terms of the Stoner model of ferromagnetism. According to the Stoner criterion, ferromagnetism is observed in those systems for which the product,

$$I\rho(\epsilon_F) > 1,$$

where $I = \Delta/m$ (Δ being the exchange splitting and m the moment of Ti in μ_B), and $\rho(\epsilon_F)$ is the paramagnetic DOS at the Fermi level. They find that the Stoner criterion is satisfied in the oxygen deficient system for all the thicknesses of STO analyzed. Like Michaeli *et al.*, Pavlenko *et al.* also find that the majority of the ferromagnetism resides in the $3d_{xy}$ band at the interface, with some minor spin polarization of the $3d_{xz}$ and the $3d_{yz}$ bands. The metallic behaviour of the charge carriers seen in transport measurements, they ascribe to the electronic reconstruction of the interface which populates the various Ti $3d$ bands. It is this metallic state that undergoes a superconducting transition below $\sim$ 300 mK as seen by various groups [**5**, **6**, **10**–**12**, **33**]. However, they do not say anything about the nature of the superconducting state.

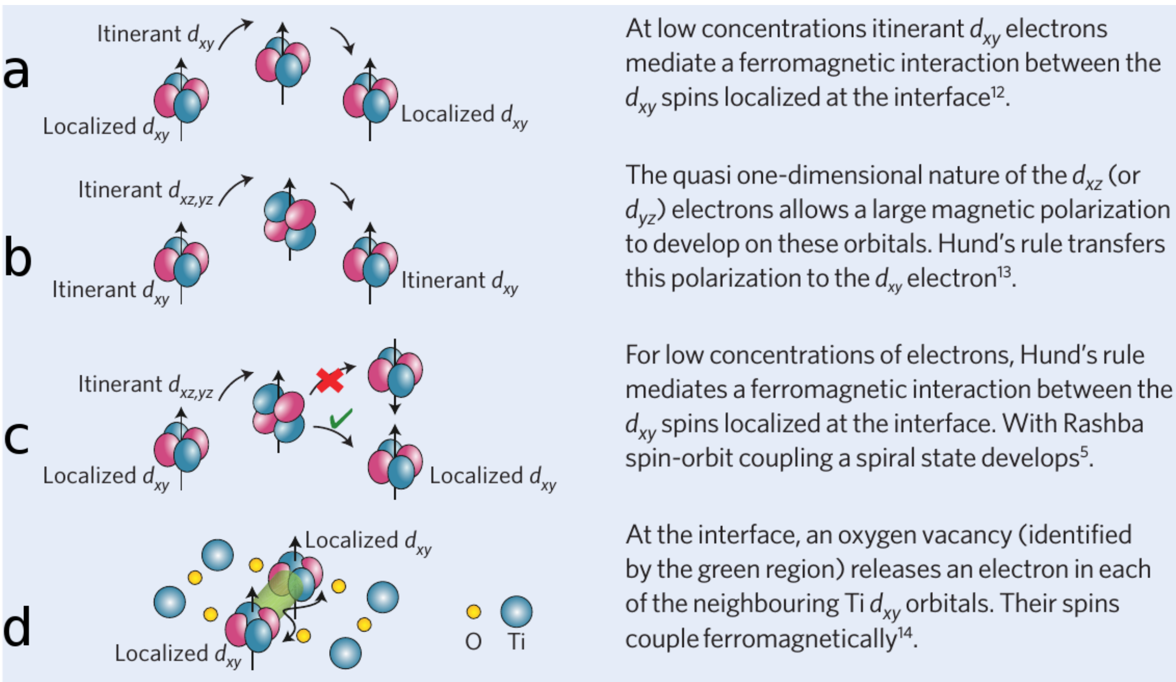

Figure 2.13. Various mechanisms proposed to explain the ferromagnetism in the LAO/STO system. Adapted from Gabay and Triscone, Ref. 82.

In conclusion to this section, I would say that one of the major challenges that face theorists is the origin of ferromagnetism at this interface. While superconductivity is thought to be arising from the mobile charges that populate the conducting Ti bands at the interface [**41**, **42**, **48**, **71**–**73**], it is still unclear which electrons take part in the ferromagnetism. This is because ferromagnetic behaviour has been reported in a variety of samples, from those that exhibit superconductivity at low temperatures, to those with relatively lower carrier densities, which show no superconductivity and even in the insulating $p-$ type interfaces [**81**]. In addition to the two mechanisms discussed above, other mechanisms have also been proposed to explain just the ferromagnetism at the interface. Figure 2.13, which is taken from Ref. 82, shows a summary of a few of those. Mechanisms labeled **a** and **d** have already been discussed above. In the work summarized by **b** in the figure, the authors propose the magnetism resulting from the quasi-one dimensional nature of the d_{yz} and d_{zx} bands, which get polarized due to Hund's rules on Ti atoms at the interface [**83**]. Banerjee *et al.*, whose work is summarized in part **c** of the figure, propose an exotic spiral state, which is enhanced by the strong spin-orbit coupling in this system [**84**]. I will not discuss these models in detail, as they do not have much to say about the superconductivity in the system, and how it coexists with the ferromagnetism.

Ferromagnetism seems to be a more general feature of the LAO/STO system, whose origin appears to be independent of whether the interface is conducting, much less superconducting. This suggests that any influence of ferromagnetism on superconductivity, in samples that show their coexistence, is electromagnetic and extrinsic, with the field due to the ferromagnet acting like an external field for the superconductor. However, given the complexity of the band structure in the vicinity of the interface, it is not difficult to imagine that in a particular sample which *does* exhibit the coexistence of superconductivity and ferromagnetism, a more exotic state for the two phenomena exists. Such a state, while not observed yet, could be the focus of future theoretical and experimental efforts.

2.5. The superconductor-insulator transition at the interface

I will now review the physics of the superconductor-insulator transition (SIT) in two dimensional electron systems. Two dimensional SIT's have been studied extensively in the past [**85**–**96**], since experimentally they are one of the more easily accessible candidates for the study of quantum phase transitions (QPT) [**97**, **98**]. In the following few paragraphs, I will go over what quantum phase transitions are, along with discussing the scaling analyses employed to study such QPT's. I will then discuss the different models used to describe the QPT in a 2D-SIT system, namely the bosonic [**86**] and the fermionic [**99**] pictures. Essentially the difference between the two pictures is that in the bosonic picture, it is assumed that long range phase coherence of the superconducting order parameter is destroyed on the insulating side, but Cooper pairs can still exist in small pockets; while in the fermionic picture the assumption is that the superconducting order parameter vanishes completely, everywhere in the sample, on the insulating side of the transition. During the course of that discussion, I will also introduce the concept of duality [**13**] as applied to the 2D-SIT, a novel manifestation of which is seen in my MR data.

2.5.1. Quantum phase transitions

Quantum phase transitions are characterized by the fact that they occur at zero temperature, $T = 0$ K [**97**, **98**]. For this section, I follow the treatment as developed in Ref. 97. Unlike classical phase transitions (CPT), which are caused due to thermal fluctuations of the order parameter near a certain temperature, called the critical temperature, T_C, QPT's are caused due to the quantum mechanical fluctuations of the order parameter at

$T = 0$ K. It should be noted that the thermal fluctuations of a quantum mechanical order parameter, such as the many-body wave function of electrons in a superconductor, say Ψ, will *still* give rise to a *classical* phase transition, which in our example is the superconducting transition. As mentioned above, the main distinguishing factor between a CPT and a QPT, is the quantum mechanical nature of the *fluctuations*, which are essentially driven by the Heisenberg uncertainty principle [**97**], in a QPT. Examples of systems which show QPT's include quantum Hall systems, Heisenberg anti-ferromagnets, heavy-fermion systems, and, as stated above, the 2D SIT.

Figure 2.14 shows a typical phase diagram of a system undergoing a QPT. QPT's are caused by the quantum mechanical fluctuations of the order parameter of a system as a parameter, say p, that appears in the Hamiltonian of the system is varied. For the case of a 2D SIT, such a parameter can be the degree of disorder in the 2D superconductor or an external magnetic field. Consider the state of the system at $T = 0$ K in Fig. 2.14. A QPT in such a system is characterized by a change in the quantum mechanical ground state of the system as p is tuned through a particular value, p_C, as shown in Fig. 2.14. (In the figure the point labeled "QCP" represents p_C.) For values of $p < p_C$, the system is in an ordered state, meaning the order parameter is finite and robust, while for $p > p_C$, it is in a disordered state with a vanishing global, phase-coherent order parameter. p_C is a quantum critical point (QCP), and the system exhibits critical behaviour in the vicinity of p_C. By critical behaviour, I mean the system exhibits power law scaling of certain

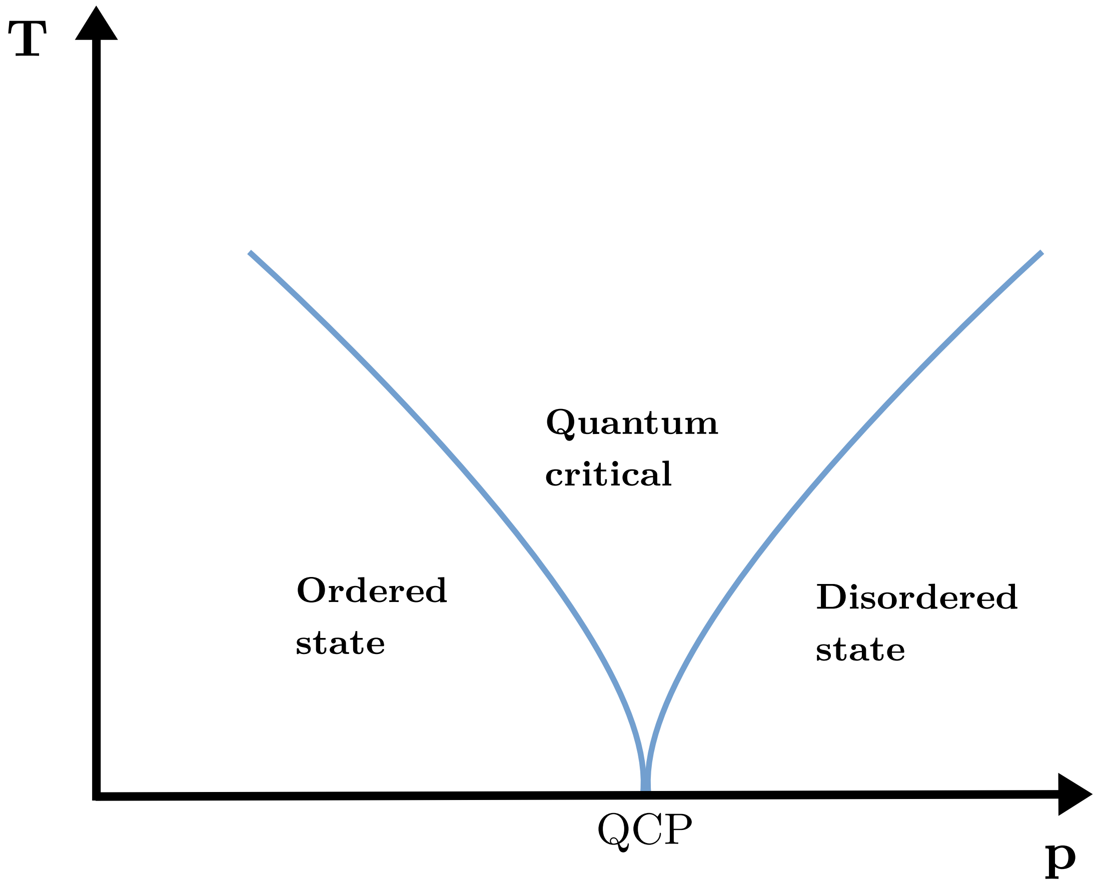

Figure 2.14. Typical phase diagram for quantum phase transition. The $x-$axis represents a parameter, p, in the Hamiltonian of the system, while the $y-$axis is the temperature.

length scales, called the correlation lengths ξ and ξ_τ, in the following manner,

$$\xi \sim |\delta p|^{-\nu}$$

$$\xi_\tau \sim \xi^z.$$

Here, ξ is the spatial correlation length of fluctuations of the order parameter, ξ_τ is the dynamical or temporal correlation length, $\delta p = p - p_C$, and ν and z are the correlation length and the dynamical critical exponents respectively. In the theory of phase transitions, ν and z are two among several universal constants characterizing a particular universality class of the transition. The values of these universal constants, called critical exponents, govern the behaviour of thermodynamic quantities, like the specific heat and the susceptibility, of the system near the transition. From the scaling relations above, one can see that near the QCP, both the correlation lengths diverge, implying long-range correlation of the fluctuations of the order parameter. Note that this kind of critical behaviour is also observed in CPT's, and hence the techniques for studying QPT's borrow heavily from the already well developed techniques for studying CPT's.

The above was a brief description of a system exhibiting a QPT at $T = 0$ K, an experimentally inaccessible temperature. Of course, if the effects of QPT's were only manifest at the absolute zero of temperature, then they would merely remain in the realm of the theoretician's efforts, with the experimentalist not having much to say about them. However, many systems that do undergo a QPT at $T = 0$ K, also demonstrate its effects at finite temperatures. As mentioned above there is a solid framework, derived from the study of CPT's, within which QPT's are studied at finite temperatures. This is made possible by considering a d dimensional quantum system at finite temperatures, as a $d+1$ dimensional classical system as $T \to 0$. The extra dimension is actually provided by the temperature itself, which acts as an imaginary time,

$$1/k_B T = \tau = -it/\hbar.$$

The reason this works is because the partition function for a classical system,

$$Z = e^{-H/k_B T}$$

maps onto the time evolution operator for the quantum system in imaginary time,

$$U = e^{-iHt/\hbar}.$$

If one can now show that a phase transition occurs in the $d + 1$ dimensional classical system, then it can be mapped onto the d dimensional quantum system. The analysis of the critical behaviour in the $d + 1$ dimensional classical system, also carries over into the d dimensional quantum system.

From the discussion above, it is clear that at finite temperatures the $d+1$ dimensional classical system on which the quantum system is mapped, does not strictly remain a proper, infinite $d+1$ dimensional system, but instead acquires a finite size in the imaginary time dimension. One of the ways to study such a system is by analyzing the finite size scaling behaviour of a certain physical quantity of the system near the QCP. For a 2D SIT, our system of interest, such a quantity is typically the resistance of the 2D electron system. By scaling behaviour, I mean that the resistance of the system is some universal homogeneous function of the variable $|\delta p|/T^{1/\nu z}$ in the following manner,

$$R(p, T) = R_C f[|\delta p|/T^{1/\nu z}]$$

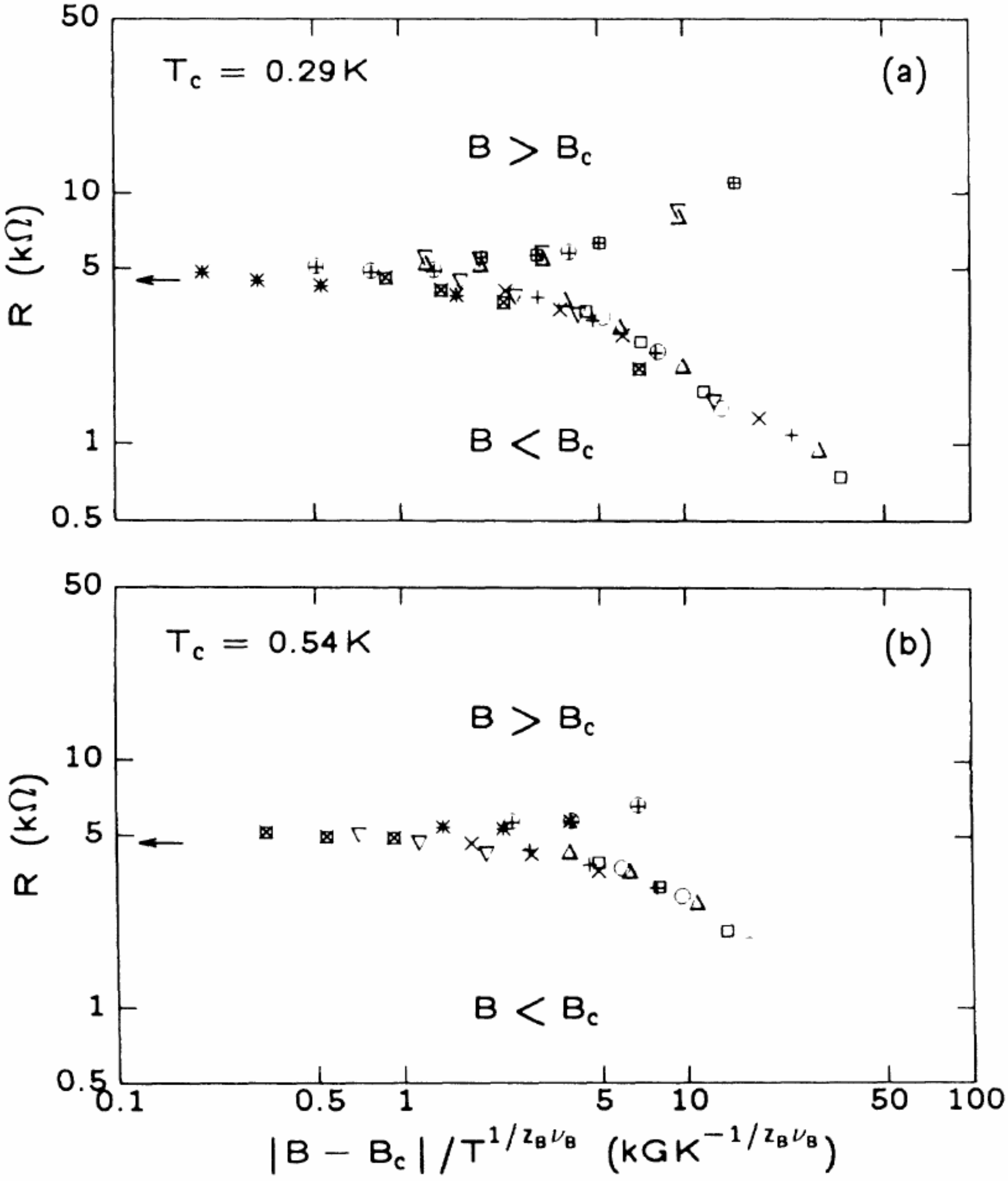

Figure 2.15. Scaling of the resistance of 2D InO_x films. Such scaling analysis is usually performed to show the existence of a QPT in a system. The extracted values of the critical exponents, ν and z (more precisely of the product νz), shed light on the universality class of the transition. Figure from Ref.89.

where f is a homogeneous function of p and T, and R_C is a constant. An example of such scaling as applied to an experimental system is shown in Fig. 2.15. This plot is taken from the work of Hebard and Paalanen [**89**], where they analyzed the magnetic field tuned SIT in InO_x films using finite-size scaling as described above. This was one of the first experimental reports to employ such a technique to study this transition. By plotting the experimental data in such a way, one can show the existence of a QPT in the system. Also, from the extracted values of the critical exponents, ν and z (more precisely of the product νz), one can determine the universality class of the particular QPT. We will be using similar scaling behaviour to study the magnetic field tuned transition at the LAO/STO interface [**100**].

2.5.2. The superconductor-insulator transition in a 2D superconductor

In this section I will review the salient points of the 2D SIT as it has been studied until now. This is now a field of study which is over 30 years old, and there is still contention about much of the essential physics of the transition [**101**]. On the theoretical side, there are two major theoretical models proposed, the bosonic [**85**, **86**] and the fermionic [**99**] models; while on the experimental side, a wide range of transport behaviour is seen [**87–96**]. Much of this variability comes from the different materials used to study this transition, and material dependent properties, such as resistivity, crucially affect the nature of the transition observed. Added onto this is the variability in disorder for each sample, which is difficult to quantify, let alone control precisely.

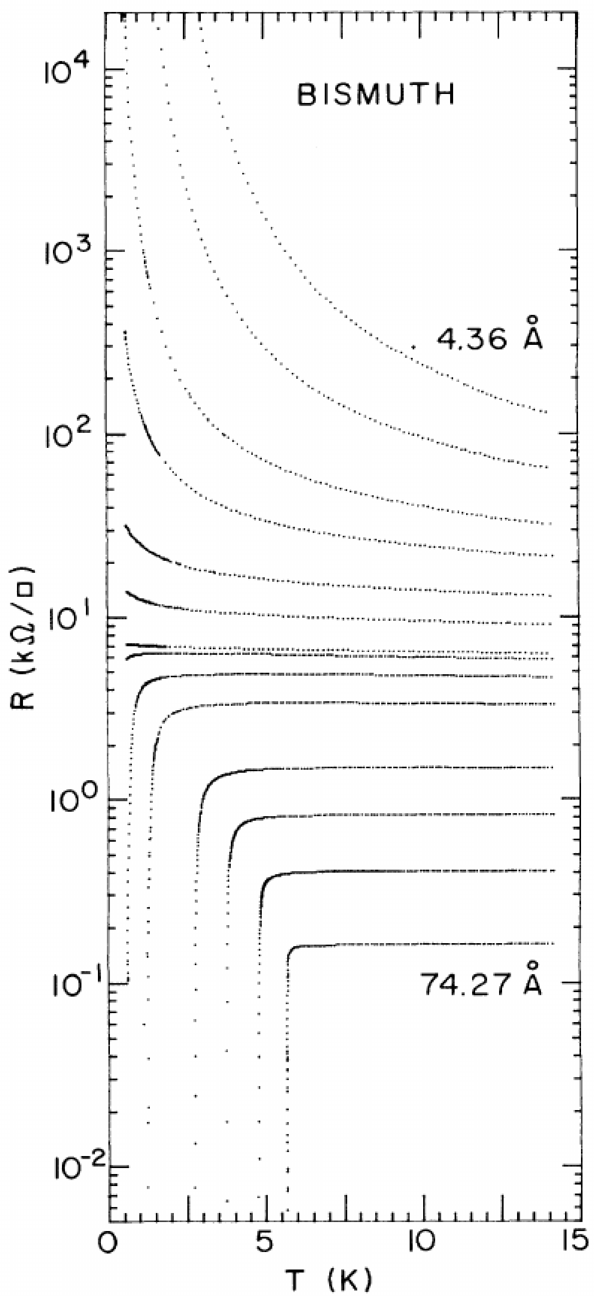

Figure 2.16. A classic example of the experimental demonstration of a SIT in 2D Bi films. As the film thickness is varied, the system transitions from a superconductor to an insulator. Figure from Ref.87

Nevertheless, there are some general characteristics of this transition which are observed across the different materials measured. One of the most ubiquitous data shown in experimental reports of SIT are the "fan" shaped curves of the temperature dependence of resistance, as the system is tuned through the SIT. A classic example of such data is shown in Fig. 2.16, which is from work published in 1989 by Allen Goldman's group [**87**], where they studied this transition in thin films of Bi. The figure clearly shows the transition of the system from a superconducting to an insulating state as the film thickness is varied. Most experimental studies of this transition show similar data, but beyond that there are differences in their detailed interpretation. Below I go over some of those phenomena whose experimental verification is still under debate within the community.

2.5.2.1. The BKT transition. It was shown by Peierls in 1935 that no long range order was possible in two dimensions [**102**], since the thermal fluctuations of long wavelength phonons increase logarithmically with the size of the system. However, it is possible to get an unconventional type of order in two dimensions, called topological order, due to a type of transition called the Berezinskii-Kosterlitz-Thouless (BKT) transition [**103**]. This is a phase transition between a state with free vortices to a state with bound vortex-anti-vortex pairs. Below the temperature at which this transition occurs, T_{BKT}, vortices and anti-vortices are bound to each other, while above this temperature, the thermal energy causes them to unbind. Such a transition was first shown on the 2D XY model [**103**], where the vortices are circulating spin structures, but has since been shown to apply to 2D superconductors as well [**104**]. The implication for the case of 2D superconductivity is that it introduces another important temperature scale below the superconducting transition temperature, T_C. From the theory of the BKT transition it can be shown that a 2D superconductor will still have a finite resistance below T_C, despite a non-zero order parameter having developed, due to the flux flow resistance caused by the free vortices. It is only when the temperature is lowered below T_{BKT} and the vortex-anti-vortex pairs are formed, that the resistance vanishes. Obviously, $T_{BKT} < T_C$.

The BKT transition is expected to be observed in all 2D superconductors. Experimentally, however, its observation is not universal [**101**]. This is because there are sample dependent length scales, for example due to granularity or disorder, that destroy the long range vortex interactions, precluding the BKT transition. Systems which have a sizable charging energy due to granular effects, also fail to show the evidence for a BKT transition. I should note that, we, in our samples, find that T_{BKT} is very close to the T_C.

2.5.2.2. Bosonic model of the 2D SIT. I will now discuss the bosonic model for the 2D SIT. As mentioned above, in this model it is assumed that as the system transitions from a superconductor to an insulator, Cooper pairs, which are charge $2e$ bosons, persist on the insulating side of the transition. However, there is no long range phase coherence between all the Cooper pairs, and the Cooper pairs are localized in small pockets of superconductivity. It is justified to treat Cooper pairs as point-like charge $2e$ bosons, because it has be shown that they Bose condense at the same temperature at which the superconducting order parameter becomes non-zero. This approach completely neglects any fermionic degrees of freedom of the system. So, for example, any quasiparticle excitations are not accounted for in this picture.

An important consequence of the bosonic picture is the concept of duality [**13**] being used to describe the superconducting and the insulating states in a SIT. Duality is a deep and unifying concept of physics. Examples of duality include the wave-particle duality of quantum mechanics or the electric and magnetic field duality of relativity. In the context of condensed matter systems, mathematically the duality transformations relate two different thermodynamic states of the system. In the case of a 2D SIT, duality transformations relate the superconducting and the insulating phases. Duality transformations are performed by considering the vortex as a bosonic particle, with a "charge" of $\Phi_0 = h/2e$, the superconducting flux quantum. Under this transformation then, the equations used to describe the superconducting state using Cooper pairs, are the same equations which can be used to describe the insulating state, if one replaces the Cooper pair wave function with that of the vortex. Of course, such a picture is only valid when there are vortices present in the system. This can be achieved using an external magnetic field; or, in our case from the effect of the magnetization dynamics of the ferromagnet, which induces vortices in the superconductor. Further discussion of how duality relates to our system is presented in Chapter 4, where I develop our model of the system.

It is possible to actually detect this duality experimentally. As mentioned above, the role of charge and flux interchanges between the two states, giving rise to an observable interchange of current and voltage, or resistance and conductance. An example of this is

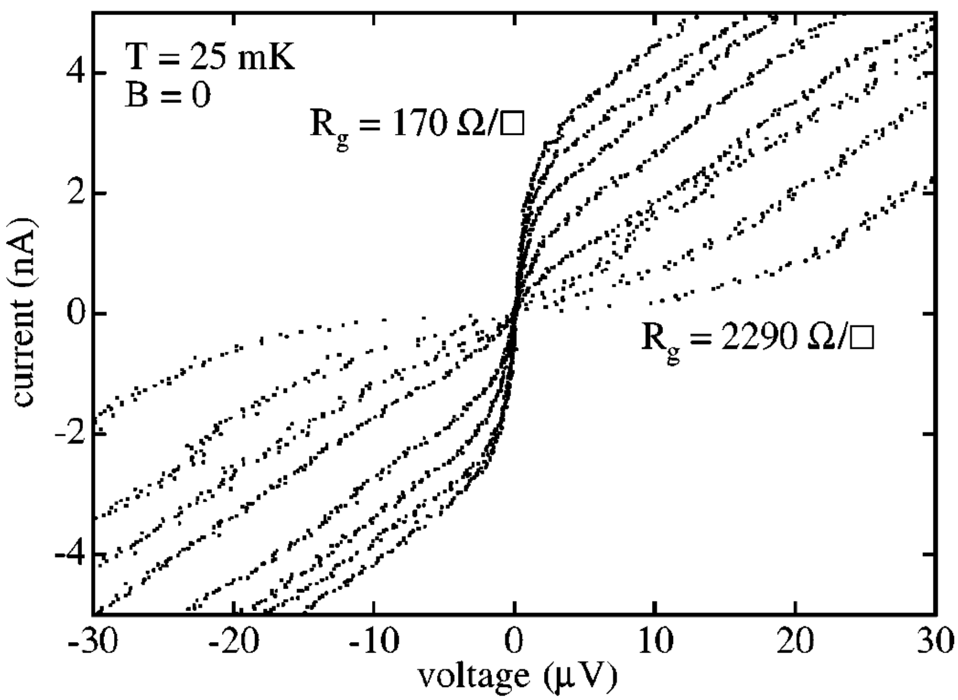

Figure 2.17. Duality of current and voltage in a 2D array of Josephson junctions. Figure from Ref. 105

shown in Fig. 2.17. In the figure, which is taken from Ref. 105, the I-V curve in the superconducting state maps onto the I-V curve in the insulating state if the roles of current and voltage are interchanged. In Ref. 105, the system is 2D array of Josephson junctions which acts as a model for a 2D superconductor. In our system, it appears difficult to tune the system into a deeply insulating state by the gate voltage. So, such observations of charge-vortex duality become difficult. But the very close proximity of the ferromagnet to our conduction gas makes possible the observation a unique manifestation of charge-vortex duality, as I will show in Chapter 4.

One of the more important predictions of the bosonic model is the existence of a universal sheet resistance at the transition [**85**, **86**]. This is predicted to be the quantum of resistance for charge $2e$ particles, $R_Q \equiv h/(2e)^2 = 6.45$ kΩ. However, this has become one of the more disputed claims experimentally, as the resistance at which the transition is observed in different materials, by different groups, is found to be wildly different [**87–93**, **105**]. Films with critical sheet resistances as low as $R_\square^C \sim 0.7$ kΩ, much less than R_Q, to films with critical sheet resistances approaching R_Q, all claim to have observed a SIT [**106**]. Moreover, it is also found that systems with different critical sheet resistances, show dissimilar critical exponents in the scaling analysis [**106**], implying that the SIT in these systems belong to different universality classes. More theoretical effort is needed in order to explain these findings.

2.5.2.3. Fermionic model. As opposed to the bosonic model, the fermionic model [**99**] assumes that Cooper pairs are destroyed everywhere in the system as the system transitions from a superconductor to an insulator. In this model the transition to the insulating state is caused by fluctuations in the amplitude of the superconducting order parameter as opposed to fluctuations in its phase. Arguments in favour of the fermionic model are, (i) that the bosonic model completely ignores the role of single particle excitations in the SIT, (ii) as mentioned above, a universal critical sheet resistance has not been observed, and (iii) some experiments have shown a suppression of the superconducting gap on the insulating side of the transition [**107**]. The role of fermionic excitations is expected to become more important in the presence of larger magnetic fields or very large amounts of disorder, as under these conditions the Cooper pairs are more likely to break apart.

In conclusion, I would say that in any given sample, it is expected that both the fermionic and bosonic pictures contribute to varying degrees. While the bosonic picture does explain many of the important features of the SIT, in order to completely explain the 2D SIT, a more unified picture, incorporating the physics of both, the fermionic and the bosonic degrees of freedom of the system is required.

CHAPTER 3

Experimental Techniques

As the name suggests, in this chapter I will cover the experimental techniques I have utilized to gather the data presented in this thesis. Since a lot of these techniques have been developed and utilized in Northwestern's Mesoscopic Physics group over several generations of graduate students, I will not dwell on the ones which have already been explained in the theses of these past students [1] [**108**–**113**]. I will only discuss those that have been newly employed, or are a refinement of previous techniques, for the experiments on the LAO/STO system.

I will begin this chapter by briefly reviewing the sample growth process, which is actually done in Prof. Chang-Beom Eom's group at the University of Wisconsin-Madison. Since this is the first thesis in our group focusing on a complex oxide system, I will spend some time in explaining the growth process, on which a lot of the sample properties depend. For a more detailed account of the growth process, one should consult the publications from Prof. Eom's group [**114**–**116**]. I will then go over the lithography techniques employed to make the patterned Hall-bars used for the transport measurements discussed here. Photolithography was used to make the samples, and I will outline the steps of the process to get the final, measurable device. I will conclude the chapter with a review of the cryogenic measurement techniques and the electronic instruments/apparatus that I

[1] At the time of writing all the theses are available at http://www.nano.northwestern.edu

have used to make the low-noise, sensitive measurements presented in this thesis.

3.1. Growth of $LaAlO_3/SrTiO_3$ heterointerfaces

The growth of novel and multi-functional oxide materials, including thin films and heterostructures like the LAO/STO interface, is in itself a very active field of research. The challenges include, (i) maintaining stoichiometry for complex, multi-element materials such as $SrTiO_3$, (ii) maintaining uniform thickness over a large area in the case of thin films (like LAO on STO), (iii) maintaining epitaxy in cases where there are lattice constant mismatches, and (iv) as with any manufacturing process, getting an acceptable yield. There are many methods employed in the growth of such materials. Among them are molecular beam epitaxy (MBE), various forms of chemical vapour deposition (CVD) methods like plasma-enhanced chemical vapour deposition (PECVD), and forms of physical vapour deposition methods like pulsed laser deposition (PLD). Our samples are grown by PLD, whose working principle and advantages I describe in the following.

Figure 3.1 shows a schematic of a PLD setup. PLD is a type of physical vapour deposition technique, i.e., it relies on physical forces, as distinct from chemical forces, to cause the growth of a thin film material on a substrate. Its first use is believed to be by Smith and Turner in 1965, when they used a Ruby laser to successfully deposit a number of materials onto different substrates [**118**]. Since then, a lot of advances in the field have resulted in PLD being the technique of choice for the growth of thin films, especially complex oxide thin films [**119**]. PLD uses high intensity ultra-violet (UV) excimer laser

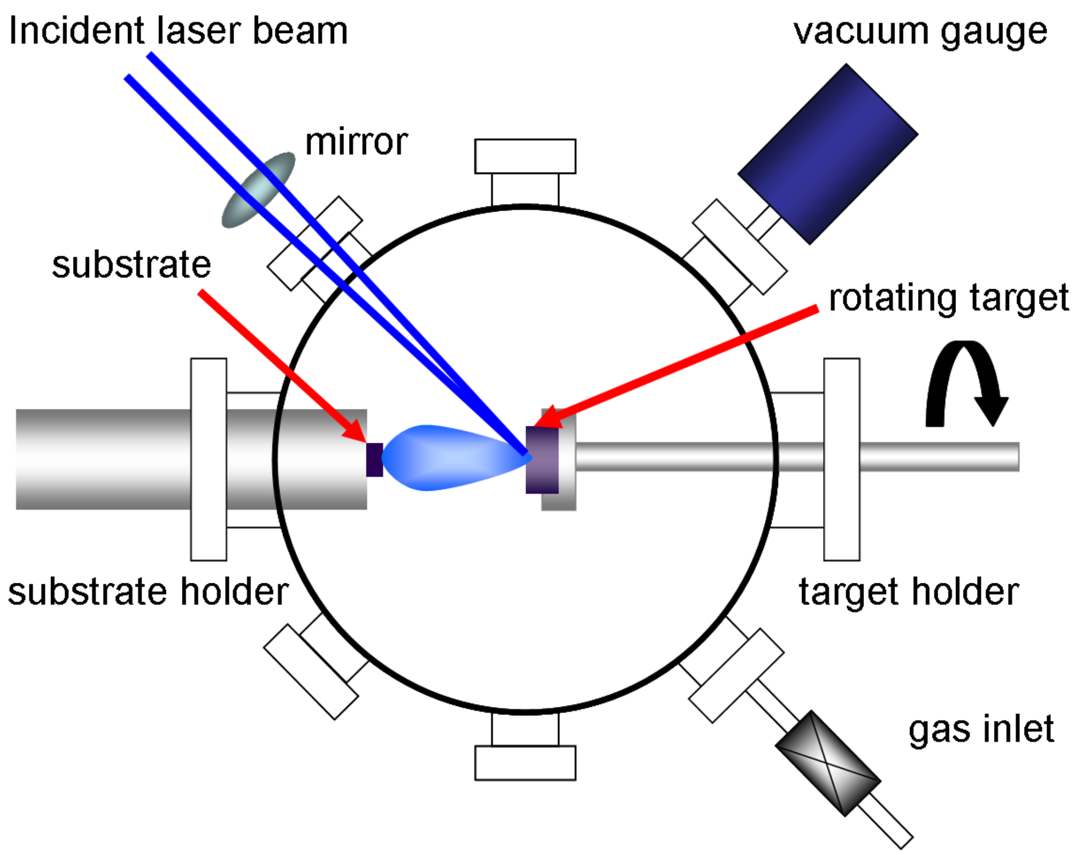

Figure 3.1. Schematic of a PLD system. From Kai Wang, [**117**].

pulses (pulse length $\sim$ 10 to 50 ns, energy density $\sim$ 1–5 J/cm^2 [**114**, **119**]) to ablate the surface of a target material (LAO in our case) which is to be deposited on a substrate (STO). The striking of a high energy laser beam on the surface of a target material causes its vaporization. This creates a luminous plasma plume of ions, electrons and atoms from the target material which rapidly expands away from the target surface (initial velocities can be as high as 10^6 cm/s [**119**]) as shown in Fig. 3.1. On reaching the substrate material, the constituents of this plume recondense to form a layer of material on the surface.

PLD is found to have a number of significant advantages over other complex oxide thin film deposition techniques. Firstly, it maintains stoichiometry, even for chemically complex multi-element compounds like YBCO ($YBa_2Cu_3O_{7-x}$) [**15**, **119**], which distinguishes it from other forms of physical vapour deposition techniques like sputtering and thermal evaporation. Second, due to the high initial velocities of the constituents of the plume, there is sufficient energy in the plume to overcome activation energy barriers for chemical reactions, on the substrate or in the plasma itself [**119**]. Third, since there is no reactive element like a hot filament in the growth chamber, the use of ambient gases, like oxygen, is readily permissible in PLD. This tremendously facilitates the growth of oxide films. Additionally, by fine-tuning the laser pulse frequency, an epitaxial growth with uniform thickness can be achieved in relatively quick time (growth rates for the LAO/STO samples presented here are ~ 10 Å/minute). Finally, with most modern PLD systems being equipped with reflection high-energy electron diffraction (RHEED) systems (consult the book by Ichimiya and Cohen for a review of the RHEED technique [**120**]), an *in situ* characterization of the film becomes possible. From the RHEED pattern acquired during growth, the epitaxiality and the uniformity of the deposited film can be ascertained, without breaking vacuum. Figure 3.2 shows the RHEED intensity acquired *in situ* during the growth of the LAO/STO samples presented in this thesis. The oscillatory pattern is evidence for the fact that the film grown is epitaxial, with a total of 10 atomic layers of LAO having been deposited, i.e., a 10 unit cell thick LAO film.

Although conceptually the technique of PLD is quite simple to understand, in practice a lot of factors affect the quality of films obtained. These include energy density of

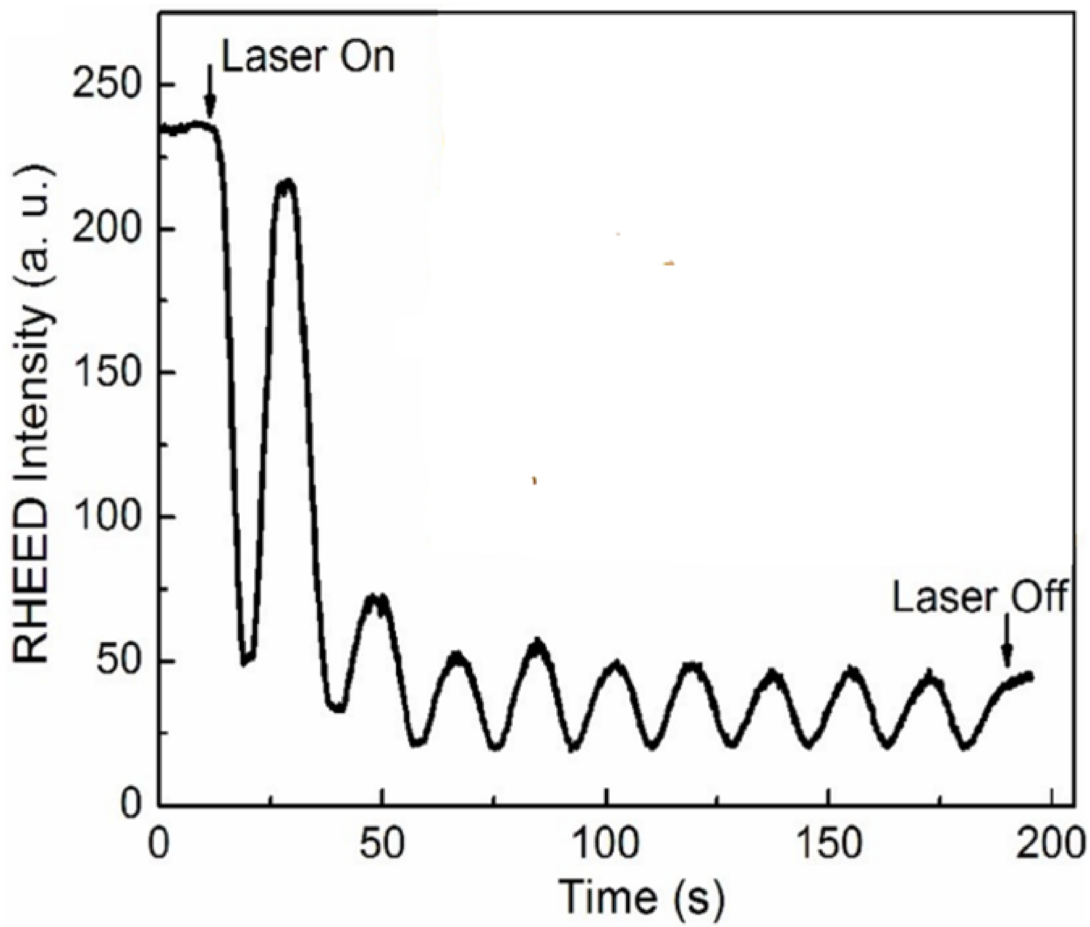

Figure 3.2. RHEED intensity acquired *in situ* during the growth of the samples used for the measurements presented here. The data is from Prof. Eom's group.

the laser beam (called fluence), the temperature of the substrate and the gas pressure in the chamber. For the LAO/STO system, for instance, the oxygen partial pressure during growth (P_{O_2}) plays a critical role in determining the sample properties as discussed in Chapter 2. Similarly the temperature of the substrate can have an effect on the stoichiometry and epitaxiality of the film being deposited. Another important factor that affects the properties of the films, especially in LAO/STO, is the termination of the substrate, STO. We know that only TiO_2 terminated STO gives rise to an $n-$type

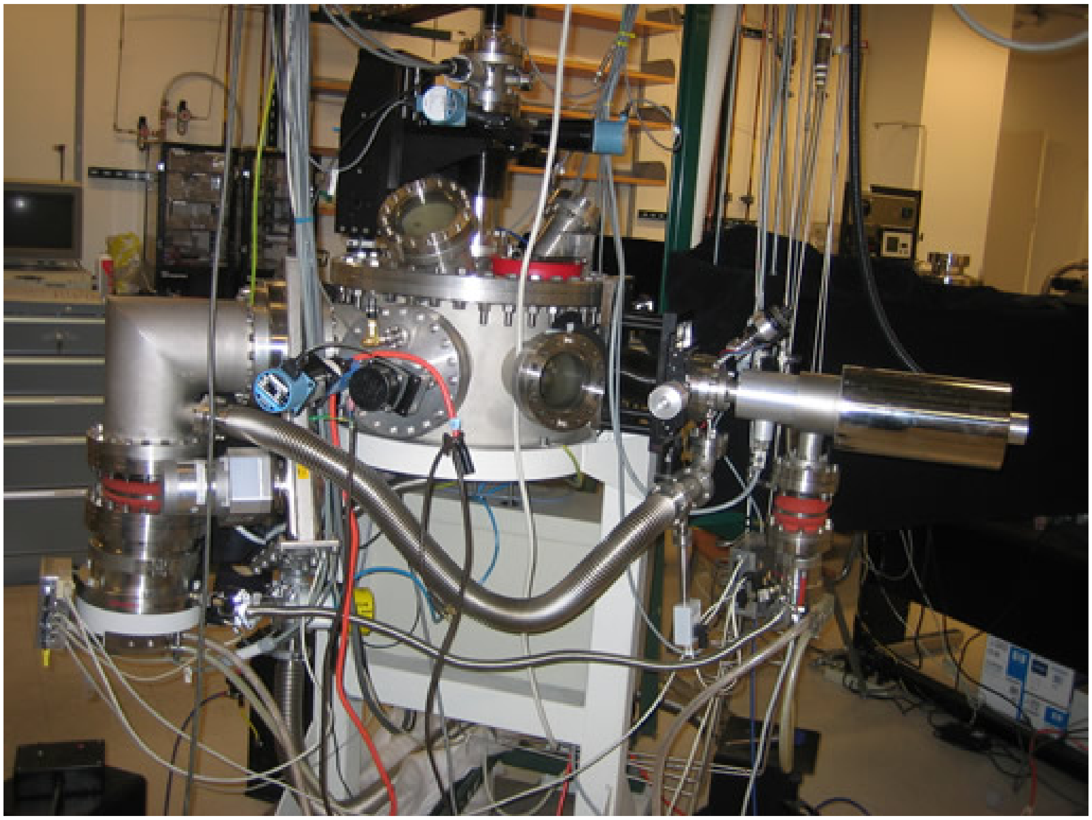

Figure 3.3. A photograph of a PLD system in Prof. Chang-Beom Eom's lab at the University of Wisconsin-Madison. At the time of writing, the image can be found at http://oxide.engr.wisc.edu/facilities-growth.htm

conducting interface [**2**]. Thus the surface of the (001) STO has to be etched in order to get a TiO_2 terminated surface. The details of the sample growth process are contained in publications from Prof. Eom's group [**114**, **115**]. Figure 3.3 shows a photograph of the PLD setup in Prof. Eom's lab at the University of Wisconsin-Madison.

The samples studied here were grown on 500 μm thick (001) STO substrates. The STO substrate was treated in a buffered hydrofluoric acid etchant solution for $\sim$90 s to maintain the TiO_2 termination. The substrate was heated by a resistive heater to a temperature of 550 ℃ and placed 5−6 cm away from the target. A KrF excimer laser (wavelength, $\lambda = 248$ nm) beam was focused on a stoichiometric $LaAlO_3$ target. The laser was pulsed at a rate of 3−5 Hz and the energy density was kept at 2−2.5 J/cm^2. 10 unit cell thick LAO films (thickness, $t \sim 4$ nm) were grown using PLD, in an oxygen partial pressure of $P_{O_2} = 10^{-3}$ mbar, with the substrate temperature maintained at 550 ℃.

I will now discuss the sample fabrication and characterization techniques.

3.2. Sample fabrication and characterization

After the as-grown samples are received by mail from Wisconsin, the samples are cleaned to remove any surface contamination that may have occurred during transportation. The cleaning procedure employed is (i) ultrasonicating in acetone for 1 minute, (ii) ultrasonicating for 1 minute in 2-propanol (iso-propyl alcohol, IPA) immediately after step (i) to prevent the the acetone from drying on the surface, which leaves behind organic residue, and (iii) blow drying in a jet of nitrogen to evaporate the IPA. Once the samples are cleaned, their surface is characterized by a room temperature atomic force microscope (AFM)[2]. One looks for atomic terraces in the AFM image as evidence for the epitaxial nature of the as-grown samples (this is in addition to the the evidence from the *in situ* RHEED). The terraces result from a small miscut (miscut angle $< 0.05°$ [**116**]) in the substrate crystal, causing a slope on the surface of the substrate which results in a terraced surface. For an atomically flat surface, the terrace heights are unit cell heights. Therefore, the observation of terraces on the surface of LAO with unit cell heights is

[2]Park XE-150, http://www.parkafm.com/

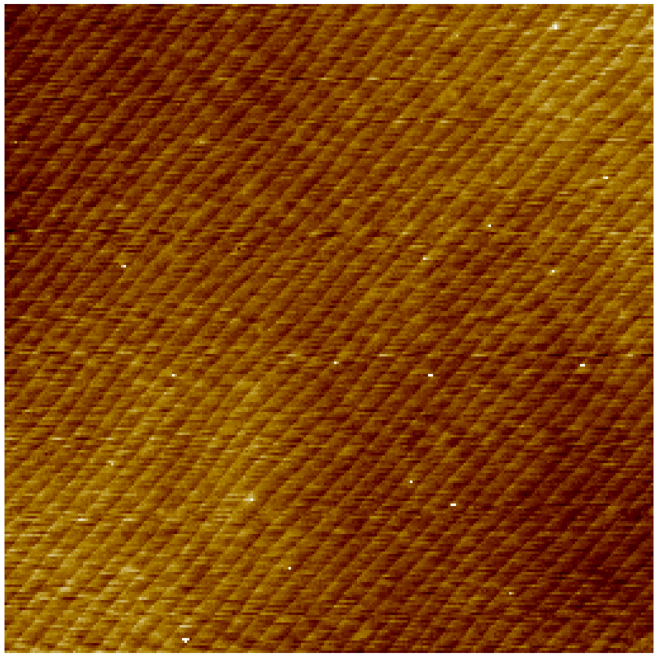

Figure 3.4. AFM image of an as received 10 unit cell thick LAO/STO sample showing the atomic terraces. The size of the imaged area is 6×6 μm^2. Image acquired by Varada Bal.

evidence for the epitaxial growth of LAO on STO. We do observe these terraces on our samples. Figure 3.4 shows an AFM image of an as-grown sample (this sample is not the one on which measurements are reported here, but a later sample).

Photolithography is used to fabricate the Hall-bar devices that I have measured. The process can be broadly divided into two parts: (i) creating the Hall-bar pattern on LAO/STO, and (ii) the deposition of metal pads around the Hall-bar for wire-bonding. Figure 3.5 shows a schematic of the first part of the process, creation of the Hall-bar pattern on the as-grown sample. Below I detail the steps of the process:

(i) The samples are cleaned with the procedure described above.

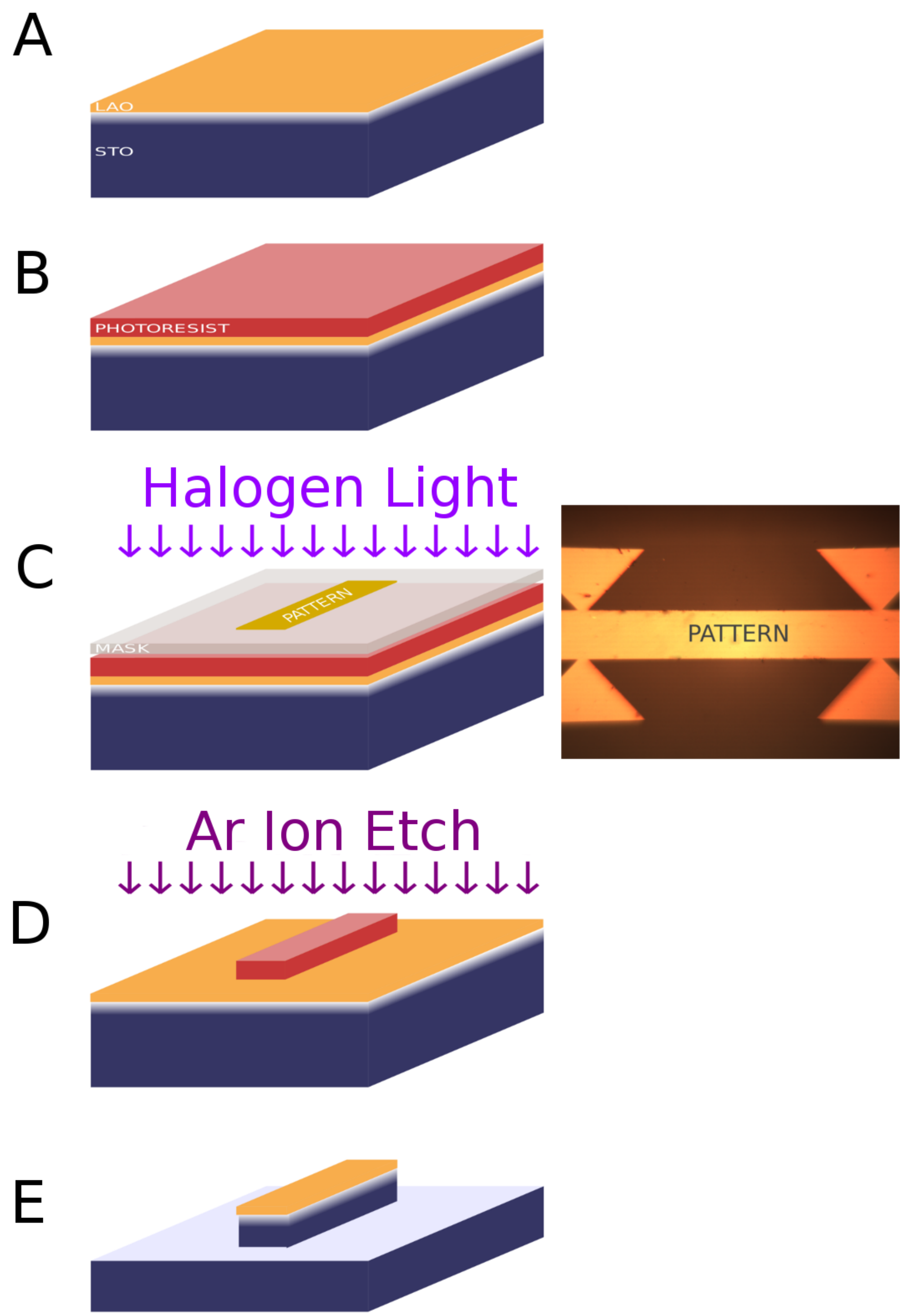

Figure 3.5. Schematic of the process to produce a Hall bar on an as-grown LAO/STO sample. Details in the text.

(ii) S1813[3], which is a positive photoresist, is spin coated onto the sample using a clean glass pipette. Here S1813 is used as an etch mask, i.e., as a protection for parts of the sample that are not to be etched away in the etching step (step no. (vii)). Note that if the lithography were being performed for the deposition of metals, as has usually been the case in our group, one would use an underlayer of LOR 7B[4], before the S1813 layer. This bilayer technique creates an undercut in the resist [**111**], which helps in a cleaner lift-off process for the metals. We do use this bilayer technique for the next part of the lithography process (step no. (x) onwards), where we deposit the metal contact pads. The sample is spun at 3,000 rpm for 40 seconds on a Headway Research[5] spinner, resulting in a uniformly coated resist film of thickness $\sim 1.5\ \mu$m. The result of this step is depicted in part B of Fig. 3.5.

(iii) The sample is placed in a Pyrex dish and baked at 110℃ for 30 minutes in a Clean 100 oven from Lab-Line Instruments[6] to evaporate the solvent from the resist.

(iv) After baking, the sample is exposed to a 120 W halogen lamp through a home-made contact printer [**111**] for 7 minutes. The lamp is placed about 1 m from the contact printer. The photomask[7] is made of a pattern of chromium coated on a plate of soda-lime glass. This step is depicted in part C of Fig. 3.5. The area labeled "PATTERN" is in the shape of a Hall-bar, and is not exposed to the

---

[3]Microposit series S1800 resists from Microchem Corp., Westborough, MA http://www.microchem.com/
[4]Microchem Corp., Westborough, MA http://www.microchem.com/
[5]Headway Research, Inc., Garland, TX, http://www.headwayresearch.com/
[6]Lab-Line Instruments, Inc., Melrose Park, IL.
[7]The photomask is acquired from Photoronics, Inc., Brookfield, CT, http://www.photronics.com/plab/photronics/

light. An optical image of section of the pattern is also shown in part C of the figure. The distance between the two voltage probes (between the two triangles in the horizontal direction) is 600 μm.

(v) After the exposure, the exposed area of the sample is washed away with a stream of MF-319[8] photodeveloper, applied through a squeeze bottle. The sample is kept under the stream for 55 seconds.

(vi) The sample is then rinsed in distilled water, and blown dry with a jet of nitrogen gas.

(vii) The next step is the Argon ion milling, shown in part D of Fig. 3.5, which etches away the area of the sample exposed to the light. For the measurements reported here, the sample was etched at Argonne National Lab by Dr. Dima Dikin. However, since then, for the later samples we have been using the ion mill in Prof. John Ketterson's lab at Northwestern. The parameters of the etch are critical because very high energy ions can introduce oxygen vacancies in the sample. Table 3.1 lists the parameters that have been optimized for the mill in Prof. Ketterson's lab. Whether the samples are etched at Argonne or at Northwestern, they show the same physics, including the coexistence of superconductivity and ferromagnetism [**121**].

(viii) After etching, the sample is ultrasonicated in acetone for 10−12 hours to wash off the resist. Once the resist has come off, the sample is rinsed in IPA and blown dry with nitrogen. This results in the desired Hall-bar pattern on the sample.

[8]Microposit photodeveloper, distributed by Microchem Corp., Westborough, MA http://www.microchem.com/

Parameter	Value
Ar pressure	8×10^{-5} Torr
Accelerating voltage	450 V
Beam voltage	600 V
Beam current	34−38 mA
Filament current	2.81 A
Time	90 s

Table 3.1. Etching parameters for argon ion milling.

The sample schematic at the end of this stage is shown in part E of Fig. 3.5. This completes the first part of the lithography process.

(ix) The sample is now again imaged using an AFM, to profile the height of the etched pattern. My samples, etched at Argonne, had a step height of 25 nm. With the etching parameters of Table 3.1, a step height of $\sim$ 20 nm is obtained. It should be recalled that the interface lies $\sim$ 4 nm below the surface. Figure 3.6 shows an AFM image of the edge of the Hall-bar acquired after the Ar-ion milling. The line-profile at the bottom shows a step height of $\sim$ 20 nm.

(x) The second part of the lithography, the laying down of the metal contact pads, is now carried out. A lot of the steps in this part of the process, like spin coating and baking, are carried out as outlined above; I will not describe them in great detail. First the sample is cleaned again, as described above. Although called contact pads, the real purpose of these metal pads is to act as a visual aid in locating the sample when making wire bond contact to it. The Hall-bar without the metal pads is not very reflective and hence difficult to distinguish from the viewing lens of the wirebonder. On the other hand, due to the high reflectance

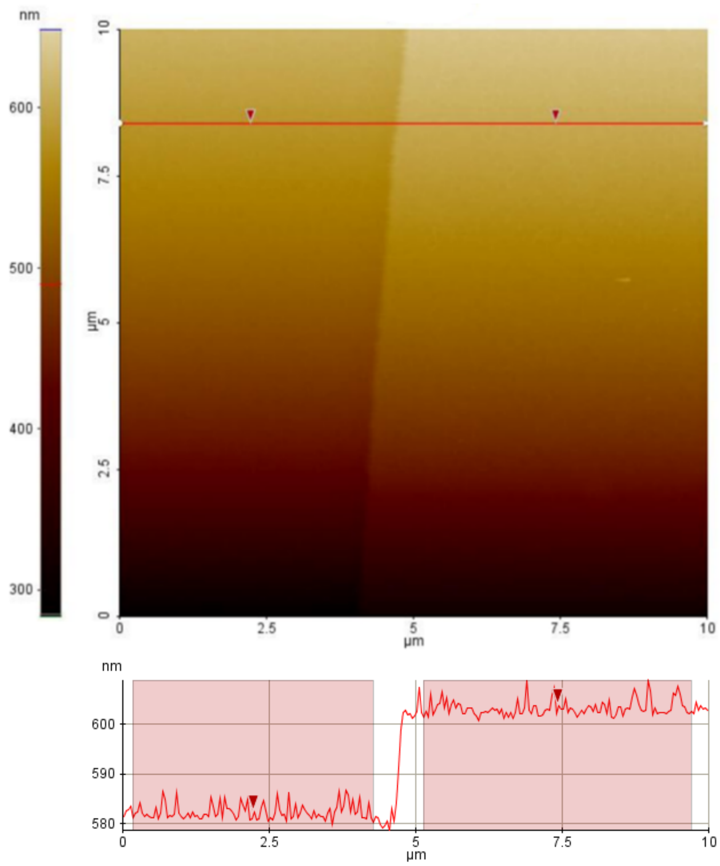

Figure 3.6. AFM image of the edge of the Hall-bar. The line-profile at the bottom shows a step height of $\sim$ 20 nm. The image was acquired after the Ar-ion milling step. Image from Varada Bal.

from the metal, its location becomes easy. In our samples, the actual contact is made directly to the 2DEG, as described below.

(xi) An underlayer of the photoresist LOR 7B is spin coated onto the sample at 4,000 rpm for 30 seconds. As mentioned above, this layer helps create an undercut, in order to aid the lifting off of the deposited metal.

(xii) It is then baked in the oven at 170 ℃ for 45 minutes.

(xiii) Next, an overlayer of S1813 is spin coated and baked as described above.

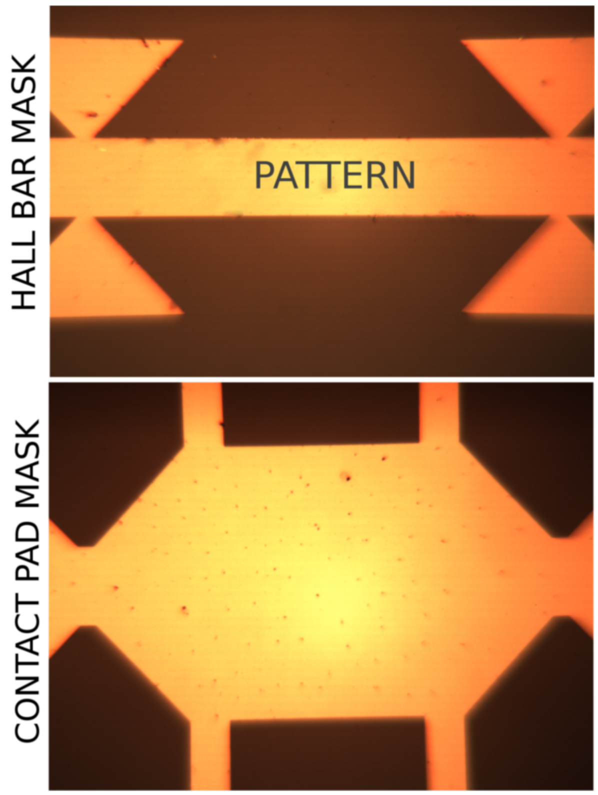

Figure 3.7. Sections of the two photomask patterns, one for making the Hall-bar on the sample and the other for making the contact pads around it. The dark parts are exposed to the light, while the bright parts, covered with chromium, block the light.

(xiv) The sample is now placed in the Süss MA/BA6[9] mask aligner and UV source, which is located in NUFAB[10] (Northwestern's clean room facility). The sample is aligned to a second, complementary photomask which exposes areas for contact pads around the Hall-bar. The two photomask patterns are shown in Fig. 3.7.

(xv) The sample is exposed to a UV lamp of wavelength, $\lambda = 365$ nm, and intensity, $I = 18$ mW/cm^2, for 12 seconds.

[9]SÜSS MicroTec AG, Garching, Germany, http://www.suss.com/en.html
[10]NUFAB, Evanston, IL,http://nufab.northwestern.edu/

(xvi) The sample is then developed in MF-319 for 55 seconds as described above. It develops both the photoresists, LOR 7B and S1813. The sample is then rinsed in distilled water, and blown dry with nitrogen.

(xvii) Once the sample is developed, it is ready for the evaporation of metal contact pads. This is done in an e-beam evaporator, JoeTek, built by one of the former graduate students of the group, José Aumentado [**110**]. The sample is loaded into the deposition chamber, along with two crucibles of the metals to be evaporated, 99.95 % purity Au[11] and 99.95 % purity Ti[12]. The chamber is then pumped down to its base pressure of $\sim 5 \times 10^{-7}$ Torr.

(xviii) Before evaporation, the sample is first etched in a 60 Hz Argon plasma to get rid any remaining organic residue, by applying a voltage between the sample stage and a metal shutter (the shutter blocks the line of sight of the sample stage from the crucibles). The etching is carried out in a background Ar pressure of 40 mTorr for 20 seconds, at a voltage of 512 VAC.

(xix) After etching, the chamber is again pumped down to its base pressure. Then $3-4$ nm of Ti is deposited, as this helps in adhesion of Au layer. The Ti is deposited at a rate of 0.4 Å/s. After the Ti layer, about 40 nm of Au is deposited at a rate of $1-2$ Å/s. Before each evaporation, a sacrificial thickness of $\sim$ 4 nm is evaporated onto the shutter to avoid the surface contaminants on the crucibles from being deposited on the sample.

(xx) After the deposition, the chamber is pumped for 20 minutes to cool the crucibles.

[11]APMEX, Oklahoma City, OK, http://www.apmex.com/

[12]Kurt J. Lesker Company, Jefferson Hills, PA, http://www.lesker.com/newweb/index.cfm

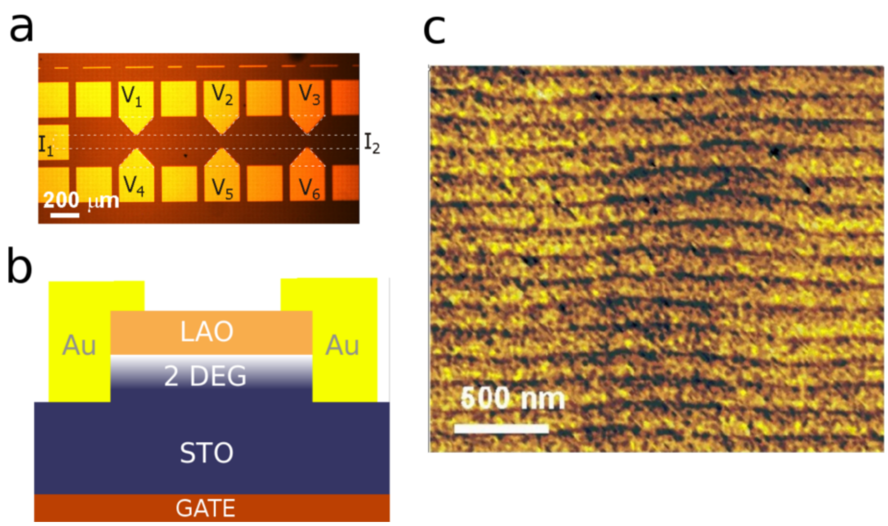

Figure 3.8. **a)** An optical image of the sample after the fabrication. **b)** A side-view schematic of the sample. **c)** An AFM image of the sample after it has been through the sample fabrication process. It shows the atomic terraces, implying that epitaxy is maintained even after processing.

(xxi) The "lift-off" is done next. This involves soaking the sample in acetone for ~ 10 minutes, followed by ultrasonication for 10 seconds, again in acetone. This gets rid of the S1813 and any metal that was on it. Care must be taken to ensure that the acetone does not dry on the surface of the sample. After the ultrasonication the sample is rinsed in IPA and blown dry with nitrogen gas.

(xxii) The penultimate step is the removal of the LOR 7B layer, achieved by soaking the sample in Microposit 1165[13] remover, at an elevated temperature of $60-65$ ℃ for ~ 10 minutes. Care should be taken to not raise the temperature of the remover much beyond 70 ℃ as it has a flash point of 88 ℃.

(xxiii) The final step is again a cleaning step, performed in the manner described above.

[13]See footnote 8.

Figure 3.8a shows the an optical image of an LAO/STO sample, taken after the photolithography steps described above have been performed. The bright areas are where the Ti/Au has been deposited, while the dark areas are either bare STO or LAO/STO. The LAO/STO part, which is the Hall bar, is marked by a white dashed line. The leads marked I_1, I_2, $\mathrm{V}_i, i = 1..6$, are the current and voltage leads in a typical measurement geometry. I_2 is usually grounded (the contact pad for I_2 is not shown due to the limited view field of the optical microscope on which this image was acquired). Figure 3.8b shows a side-view schematic of the sample; the shaded region in STO depicts the 2DEG. The height of the Hall-bar is, as mentioned above, ~ 25 nm, while the thickness of the Ti/Au (Ti not shown) is ~ 43 nm. After the sample is fabricated it is once again characterized with an AFM. This is done to check if the sample epitaxy has been affected by the processing. Figure 3.8c shows an AFM image of the top of the LAO layer in the sample after it has been through all the processing steps. The atomic terraces are clearly visible, indicating that the sample has indeed maintained epitaxy. Another check performed to rule out the effect of the Ar-ion milling on the properties of the sample is to measure the conductivity through the bare STO which has been exposed by the milling process. There are pads in the Hall-bar pattern which allows one to measure the conductivity through the STO (these are the square pads adjacent to the voltage leads in Fig. 3.8a, which lie directly on the bare STO, thus making contact only to the surface of STO, not the LAO). We indeed find in our samples that the STO remains insulating ($R > 1$ GΩ) after the sample has been fabricated at all measured temperatures.

3.3. Transport measurement techniques

In this section I describe the techniques used to make the electrical transport measurements on the sample. A lot of these have been in use in the group for more than two decades. These include cryogenic techniques for operating the two dilution refrigerators in the group, the older Kelvinox-300 and the newer Kelvinox-100, on which most of the measurements presented here were taken. The group also has significant expertise in performing low-noise, sensitive electrical transport measurements on a variety of samples. I will not be describing these techniques in detail, and will only limit the discussion to certain important parameters of the measurements which may affect the physics at the LAO/STO interface. A detailed discussion of these techniques, as they have been developed in the group, through the years, can be found in the theses of past students [**108**–**113**]. I will conclude by describing two relatively more involved techniques employed for making two different measurements: the mapping of the $T_C - H$ phase diagram of the superconductor and the determination of the critical field in the magnetic field tuned superconductor-insulator transition at the interface.

3.3.1. Cryogenics

After the sample has been fabricated, it is wire bonded to the sample holder using a Kulicke & Soffa 4123 Universal wedge bonder[14] and mounted on one of the two dilution refrigerators [**122**] in the lab. As mentioned above, the wire bonds are made by punching

[14]Kulicke and Soffa Industries, Inc., Fort Washington, PA, http://www.kns.com/en-us/Pages/Home.aspx

directly into the 2DEG through the LAO (in the areas enclosed by the white dashed triangles of Fig. 3.8a), as bonding to the the contact pads does not produce a good contact with the 2DEG. The older Kelvinox-300[15] has a base temperature, $T_{base} < 15$ mK, and is equipped with a 12 T superconducting solenoid magnet. The newer Kelvinox-100[15] also has a base temperature, $T_{base} < 15$ mK, and is equipped with two superconducting magnets, a solenoidal magnet which can apply a 3 T axial field, and a split coil magnet which can apply a 1 T in-plane field. Both these magnets can be run simultaneously, making it possible to apply a 2D vector field on the magnet. Both the fridges have RuO_2 resistance thermometers mounted on their respective mixing chamber plates. The thermometry is done via a commercial TRMC2[16] multi-probe regulator on the Kelvinox-300, while on the Kelvinox-100, the temperature is read by Oxford's "Femtopower" system. Both fridges also have rf-filters on each electrical line at the top, which shield the fridge from rf-radiation transmitted through the electrical lines. On Kelvinox-300 the cut-off frequency of the filters is 5 MHz, while on Kelvinox-100 it is 800 kHz.

3.3.1.1. Magnetic field control. The superconducting magnets are typically run by flowing a large DC current through them. A range of power supplies have been used to power the magnets. On Kelvinox-300, a Lakeshore 622[17] bipolar superconducting magnet supply which can source 120 A current is used for large magnetic fields ($H > 2.5$ T), and a Kepco BOP 20-20M[18]bipolar power supply capable of sourcing 20 A is used for smaller

[15]Oxford Instruments, Concord, MA, http://www.oxford-instruments.com/
[16]From AIR LIQUIDE (subsidiary of ABB), France. The company no longer sells this product.
[17]Lakeshore Cryotronics, Inc., Westerville OH, http://www.lakeshore.com/Pages/Home.aspx

magnetic fields ($H < 2.5$ T). On the Kelvinox-100, a Kepco BOP 20-50MG[18] digital bipolar power supply (capacity 50 A) is generally used to generate an axial field, while the in-plane field is generated by a Kepco BOP 100-1M[18] bipolar power supply (capacity 1 A).

3.3.2. Electronics and instrumentation

Much of the data presented here is the variation in the resistance of the sample, measured as some external parameter, like temperature or magnetic field, is changed. Measuring this resistance is usually done by a four probe ac lock-in technique, which actually measures dV/dI, the first derivative of voltage with current (also called differential resistance), as a small ac current is sourced to the sample. This technique has been discussed in most of the previous group theses [**108**,**111**,**113**] and will not be described in detail here. Only a brief overview is given in the following.

In sourcing the small ac current mentioned above, call it I_o, typically two different methods are employed, (i) through an ac resistance bridge,[19] and (ii) through a homemade current source employing the AD549[20] chip (for a circuit diagram of the current source see Jonghwa Eom's thesis [**108**]). In either case, the voltage from the sample is amplified by an instrumentation amplifier, either AD624[21] or INA110[22]. The output of the instrumentation amplifier is fed into the lock-in amplifier (LIA), the reference oscillator of which

[18]Kepco, Inc., Flushing, NY, http://www.kepcopower.com/
[19]This is an Adler-Jackson type bridge, modified based on a General Radio 1433-X or 1433-F bridge.
[20]Analog Devices, Norwood, MA, http://www.analog.com/en/index.html
[21]Analog Devices, Norwood, MA, http://www.analog.com/en/index.html
[22]Texas Instruments, Inc., Dallas, Texas, http://www.ti.com/. Formerly made by Burr-Brown Corp.

also provides the input to the current source. Two types of lock-in amplifiers were used, an analog PAR 124[23] and a digital EG&G 7260.[24] The output from the lock-in amplifier, which is basically a dc voltage proportional to the differential resistance of the sample, is read by a HP 34401A[25] digital multimeter (HP DMM), which in turn is interfaced with the measurement computer via GPIB.

A schematic of the measurement setup for recording dV/dI vs. I_{dc} is shown in Fig. 3.9. In this setup, two voltages, a dc voltage, V_{dc}^{in}, from an HP3325A synthesizer and an ac voltage, V_{ac}^{in}, from a PAR 124 LIA, are summed using a homemade voltage summer (for a circuit diagram of the summer see Jonghwa Eom's thesis [**108**]). The output of the summer is supplied to the input of the above mentioned homemade current source. The current source generates the current $I_{dc} + I_{ac}$ which is sourced to the sample. The voltage dropped across the sample is amplified by an AD624 instrumentation amplifier with a gain, G (typically G = 100, 200 or 500). The dc component of the output of AD624, V_{dc}, is read by a HP DMM, while the ac component, V_{ac}, is read by the LIA. The LIA's phase is set to be in phase with the source current I_{ac} in order to measure the full voltage drop across the sample. The output of the LIA, which is proportional to dV/dI, is read by another HP DMM which communicates with the measurement computer via GPIB. The source current also passes through a sense resistor, and the voltage dropped across it is amplified by another AD624 whose output is read by an HP DMM. This provides

[23]From Ametek Princeton Applied Research, Oak Ridge, Tennessee, http://www.princetonappliedresearch.com/index.aspx

[24]Ametek Signal Recovery, Oak Ridge, Tennessee http://www.signalrecovery.com/index.aspx

[25]Keysight Technologies, Inc., Santa Rosa, CA http://www.keysight.com. Formerly made by Hewlett Packard.

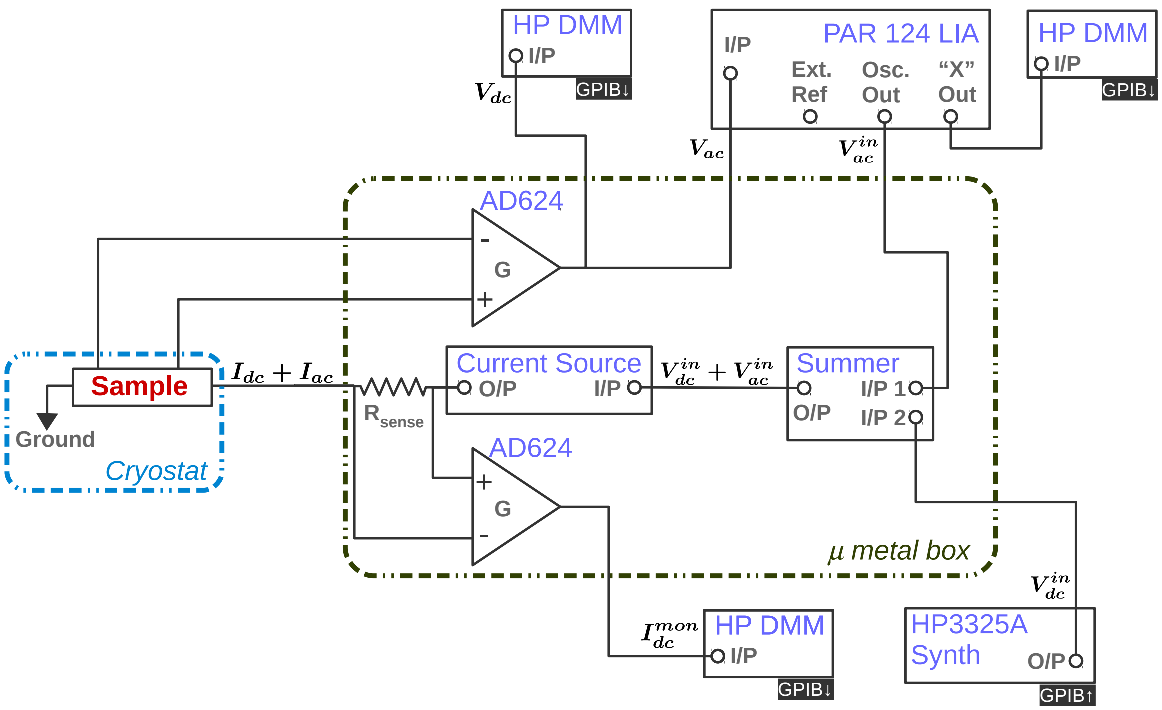

Figure 3.9. A typical measurement setup schematic employing the home-made current source and summer. This measurement setup is used for making dV/dI vs I_{dc} measurements.

a measure of the dc current, I_{dc}, being sourced to the sample. Finally, the dc current is varied by sweeping the voltage V_{dc}^{in} from the synthesizer, which is controlled from the computer via GPIB, as shown in the figure. The summer, the current source, and the instrumentation amplifier are powered by batteries and placed in a shielded $\mu-$metal box in order to reduce EMI (electromagnetic interference) effects from mixing with the small measurement signals.

In choosing the value of the source current I_o, care should be taken that the Joule heating of the sample due to the current, $P_J = I^2R$, does not cause an increase in the temperature of the electrons [**108**]. On the other hand, a larger source current results in a larger magnitude of the signal, leading to a better signal to noise ratio. Also, in the case of a measurement of dV/dI as a function of the dc bias current I_{dc}, the magnitude of I_o should not exceed the minimum step size of I_{dc}, to avoid the broadening of any features in the dV/dI vs I_{dc} curve. The values of I_o used in my experiments varied from 10 nA to 100 nA for different measurements. These values were chosen to ensure that the signal strength is optimized within the constraints listed above.

Apart from the instruments mentioned previously, several other instruments were typically used in my measurements. A Keithley 230[26] voltage source, which can apply ± 100 V, is usually used to apply a back gate voltage to the sample. Since the Keithley 230 is a noisy source, a low pass filter of cutoff frequency ~ 1 Hz was used at its output. For measurements involving the application of a dc bias current to the sample, an HP3325A[27] or an Agilent 33509B[28] waveform generator is used as an input to the current source, which in turn sources the bias current I_{dc}. Another very vital instrument used is the SR760 FFT[29] spectrum analyzer. This instrument is used to characterize the magnitude and the spectral distribution of noise in the signal. Typically the noise floor (the noise at all frequencies where there are no peaks in the spectrum) on the output of the lock-in (referred to input) as measured by the SR760 is $6-8\ \mathrm{nV_{rms}}/\sqrt{\mathrm{Hz}}$, near the expected noise level of $4\ \mathrm{nV_{rms}}/\sqrt{\mathrm{Hz}}$ for the instrumentation amplifier AD624. It should be noted that despite the relatively high resistance of the insulating state in the LAO/STO samples

[26]Keithley Instruments Inc., Cleveland, OH, www.keithley.com
[27]See footnote 25
[28]See footnote 25
[29]Stanford Research Systems Inc., Sunnyvale, CA, www.thinksrs.com

($R \sim 16$ kΩ), the Johnson noise due to the sample resistance is still smaller than the noise due to AD624. The Johnson noise of a resistor per unit bandwidth is given as, $V_n = \sqrt{4k_BTR}$, where T is the temperature, R is the resistance, and k_B is the Boltzmann constant. The highest Johnson noise in my measurements is estimated to be ~ 1 nV/$\sqrt{\text{Hz}}$ at $T = 1$ K, the highest measurement temperature. Since independent noise sources add in quadrature, the largest Johnson noise contribution from the sample is still $1/16^{th}$ the contribution from AD624.

Sometimes a 60 Hz signal and its harmonics are present in the spectrum, and in such cases the measurement signal frequency is chosen in the flatter parts of the noise spectrum. We also found a strong frequency dependence of the resistance of the system as shown in Fig. 3.10 for two different gate voltages, V_g = -20 V and V_g = -60 V. The resistance was found to decrease with increasing frequency for frequencies greater than ~ 9 Hz for both the gate voltages, while it decreased sharply in the range $2-9$ Hz for V_g = -20 V and increased sharply for V_g = -60 V as shown in the inset of Fig. 3.10. The decrease in resistance with increasing frequency is a signature of capacitive behaviour (the capacitive impedance, $Z_C = 1/2\pi fC$; in our case, however, the dependence is much slower than $1/f$, indicating an equivalent circuit with both L (inductor) and C type behaviour). Below the "transition" frequency of ~ 9 Hz, the behaviours of the two gate voltages are completely opposite, which we do not yet understand. In order to minimize the effect of the strong frequency dependence, all of our measurements were performed at a frequency of $f = 11.3$ Hz, just above the "transition" frequency of ~ 9 Hz. I should also mention that the 60 Hz and harmonics were particularly large in Kelvinox-100; however, subsequently a new Ufer ground has been installed outside the lab, which seems to have taken care of this problem.

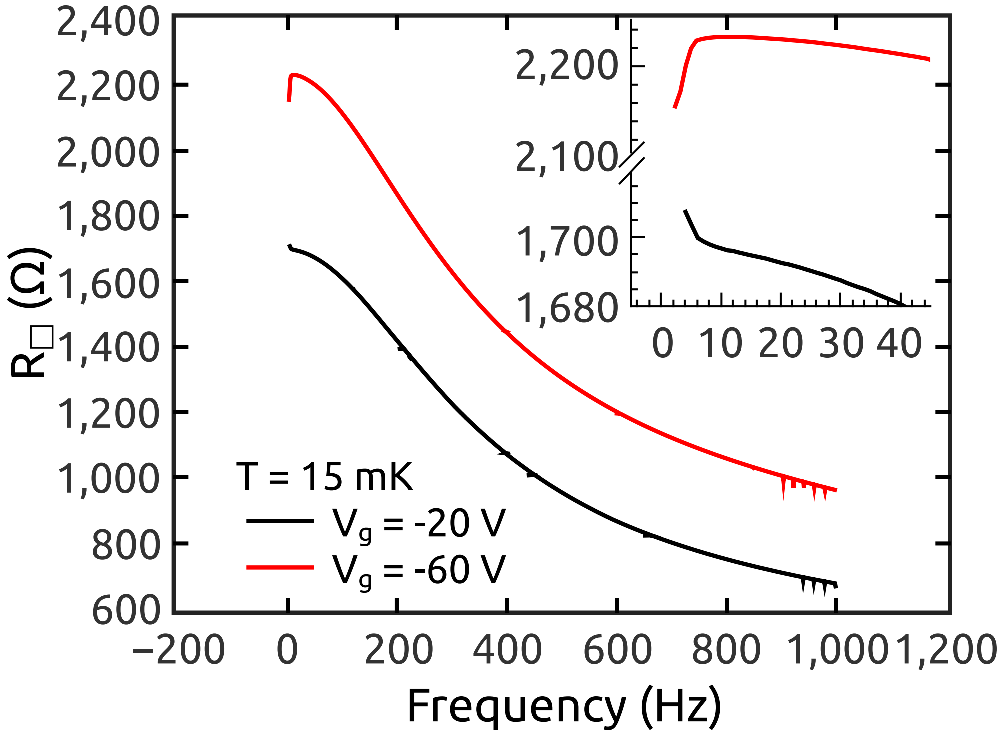

Figure 3.10. Frequency dependence of the resistance of the sample. Inset shows the zoomed in region at low frequencies.

3.3.2.1. $T_C - H$ **measurement using the PID.** While a majority of the measurements reported here are of the variation of dV/dI as a function of an external parameter, a couple of more involved measurements are also reported. Among them is the mapping out of the magnetic field−critical temperature, $H - T_C$, phase diagram of the superconducting state of the system, in perpendicular and parallel fields. This was done continuously as a function of the applied field by inserting a proportional-integral-differential (PID) control loop into the path of the dilution fridge's mixing chamber heater. A schematic of such a measurement setup is shown in Fig. 3.11, as it was implemented on the Kelvinox-100.

This technique involves the use of a modified Adler-Jackson resistance bridge (for a circuit diagram and a description of the working of the bridge see Jonghwa Eom's thesis [**108**]). The bridge circuit sources an equal current, I_o, through its two arms, one of which has the sample, and the other has a tunable balance resistor, R_{bal}. When the two resistances are equal, the bridge outputs a zero voltage at its two output terminals. However, if there is an imbalance in the resistances of the two arms, say due to a change in the sample resistance, the bridge outputs a voltage differential proportional to the difference in the resistances, $\Delta V = I_o \Delta R$, which is measured by the LIA. The polarity of the output voltage is determined by the polarity of the resistance change. In this way the sample resistance is measured by computing, $R_{sample} = R_{bal} + \Delta R$, facilitating the measurement of small changes in resistance to great precision.

To map out the $T_C - H$ phase diagram, we begin with zero externally applied field. The temperature of the sample is set to the critical temperature, T_C, typically defined as the mid-point of the resistive transition, by applying power to the mixing chamber heater. In practice we can sit anywhere along the resistive transition, say 80 % of the way down, and map out the phase diagram of the transition temperature at that point vs. the field with this technique, i.e., a $T_{@0.2R_{normal}} - H$ phase diagram. As shown in the results chapter, we do indeed map out the $T - H$ phase diagram along various points on the resistive transition. For the explanation of this technique, however, we take the specific case of T_C defined as the midpoint of the resistive transition, i.e., at T_C, $R_{sample} = R_{normal}/2$. Now, with the temperature of the sample at T_C, the balance resistor in the bridge is set to half the normal state resistance. Therefore, at T_C, $R_{sample} = R_{bal}$, and the bridge

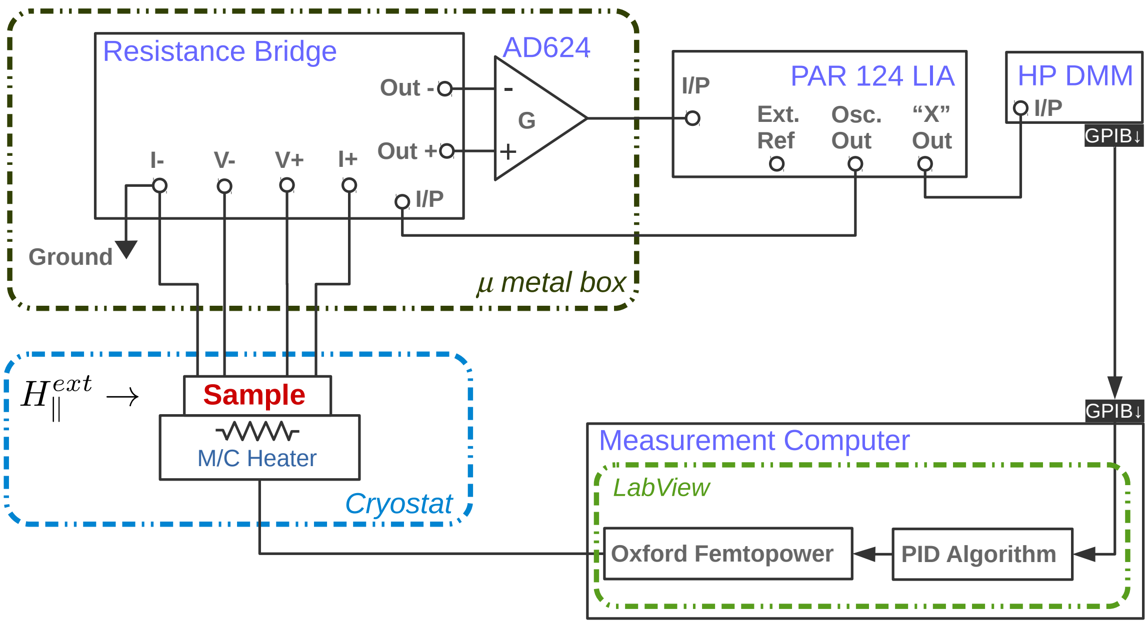

Figure 3.11. Schematic of the instrument configuration for mapping out the T_C-$H_{\parallel}$ phase diagram in the superconducting phase.

outputs a zero voltage. Now the external field, say parallel to the sample, $H_{\parallel}^{ext}$, is varied. This causes a change in the resistance of the sample. The bridge outputs a voltage proportional to this change, which is read by the LIA (through an AD624). The output of the LIA is the "error" signal to be controlled which is read by the HP DMM and sent to the measurement computer via GPIB. We implement the PID loop in NI LabVIEW[30] in the computer[31]. As mentioned above, for the Kelvinox-100 the fridge thermometry is controlled by the Oxford Femtopower module, which is also implemented in LabVIEW. The output of the PID algorithm is sent to this Femtopower module. If the change in external field causes an increase in the resistance, i.e., $R_{sample} > R_{bal}$, a non-zero error

[30] LabVIEW System Design Software, National Instruments Corp., Austin, TX, http://www.ni.com/labview/

[31] The LabVIEW file for the PID algorithm is called PID_ForMCHeater.vi and was co-written by me and Varada Bal.

signal appears at the input of the PID. In response the PID output acts to reduce the power of the mixing chamber heater, which lowers the temperature of the sample. This results in a concomitant decrease in the resistance (remember, $dR/dT > 0$ for the superconducting transition) and a re-establishment of $R_{sample} = R_{bal}$, a condition for T_C. Thus, while the PID loop is on, one always sits at the midpoint of the resistive transition, enabling one to map out the T_C vs. H phase diagram continuously. Needless to say, this technique is very sensitive to the P, I, and D values due to the sharpness of the superconducting transition. If these values are not set carefully, the output of the PID may saturate leading to a runaway heating of the fridge. In the case of the Kevinox-300, which does not have the Femtopower module, an analog PID circuit is used (diagram in Jonghwa Eom's thesis [**108**]), whose analog output can be used to power mixing chamber heater on that fridge. This measurement technique is also described Prof. Venkat Chandrasekhar's Ph.D. thesis [**123**].

3.3.2.2. The third derivative, d^3V/dI^3, measurement. Another type of measurement made is the determination of the critical field in the magnetic field tuned superconductor to insulator transition (SIT) in the system. This was achieved by measuring the third derivative of voltage with current, d^3V/dI^3, as a function of the external magnetic field. Measuring d^3V/dI^3 requires the use of the EG&G 7260 lock-in amplifier operating in its "Dual Harmonic" mode. In this mode, the 7260 can not only measure the fundamental reference frequency (ω) that it outputs, but also any one of the higher harmonics ($n\omega,\ n = 1, 2, 3, ...$) of the reference frequency. For the third derivative measurement, we choose to measure the third harmonic (3ω). The reason for this can be seen mathematically, if the voltage is expressed as a function of the current: $V_{signal} \equiv V(I) = V(I_{dc}+I_{ac})$. Here, V_{signal} is the signal from the sample that is fed into the input of the lock-in and contains the fundamental and all the higher harmonics. Then one can Taylor expand the function $V(I)$,

$$\begin{aligned} V(I_{dc} + I_{ac}) &= V(I_{dc} + I_o \mathrm{sin}(\omega t)) \\ &\approx V(I_{dc}) + I_o \frac{dV}{dI} \mathrm{sin}(\omega t) + \frac{I_o^2}{2!} \frac{d^2V}{dI^2} \mathrm{sin}^2(\omega t) + \frac{I_o^3}{3!} \frac{d^3V}{dI^3} \mathrm{sin}^3(\omega t). \end{aligned}$$

Since

$$\mathrm{sin}^3\theta = \frac{1}{4}(3\mathrm{sin}\theta - \mathrm{sin}3\theta)$$

one can see that the third derivative can be obtained from V_{signal} at the third harmonic, 3ω. In fact,

$$\frac{d^3V}{dI^3} \mathrm{sin}(3\omega t) = \frac{-24}{I_o^3} \times V_{signal}|_{3\omega}$$

and by measuring at 3ω, the lock-in "picks out" the the third derivative signal from V_{signal}. Note that the third derivative signal is 180° out of phase with the reference signal. In practice, the measurement of the third derivative is very sensitive to noise and drifts since the signal is very small.

Figure 3.12 is presented here to explain how the third derivative technique works in determining the critical field in a magnetic field tuned SIT. The figure shows the dV/dI vs. I_{dc} curves of the system at different magnetic fields. While this data and its implications are discussed in detail in the results chapter, here I would like to draw attention

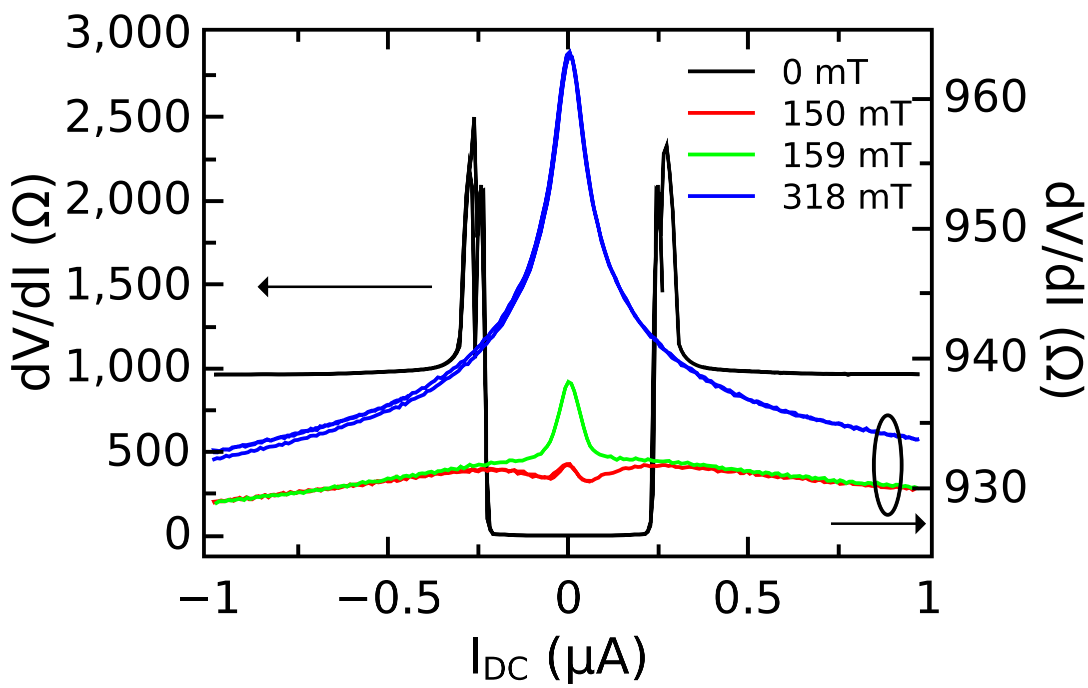

Figure 3.12. dV/dI vs. I_{dc} of the system in different magnetic fields at a gate voltage of 60 V, showing the superconductor to insulator transition. The temperature was 50 mK.

to just one aspect of the data: the shape of the different curves at $I_{dc} = 0$ μA. In the superconducting state (black curve, $H = 0$ mT), $dV/dI = 0$, and so are d^2V/dI^2 and d^3V/dI^3. As the magnetic field is increased, the shape of the curve at $I_{dc} = 0$ changes. At $H = 150$ mT (red curve), the system is still in the superconducting state, and $dV/dI > 0$, $d^2V/dI^2 = 0$ while $d^3V/dI^3 > 0$. At $H = 159$ & 318 mT, the system is insulating, and $dV/dI > 0$, $d^2V/dI^2 = 0$ while $d^3V/dI^3 < 0$. Table 3.2 summarizes the values of the three derivatives at different fields. It is clear that the only distinguishing factor between the superconducting and the insulating states, is the sign of the third derivative. Thus in order to measure the field at which this transition occurs, one simply monitors the sign of the third derivative: the field at which the sign of d^3V/dI^3 goes from positive to negative, is the critical field of the transition. Further details of this measurement are described at the appropriate place in the results (next) chapter.

System state	Field (mT)	dV/dI	d^2V/dI^2	d^3V/dI^3
Superconducting	0	0	0	0
Superconducting	150	> 0	0	> 0
Insulating	159	> 0	0	< 0
Insulating	318	> 0	0	< 0

Table 3.2. dV/dI, d^2V/dI^2, and d^3V/dI^3 values in the magnetic field tuned superconductor-insulator transition at discrete fields.

CHAPTER 4

Results and Discussion

In this chapter, I present the results of transport measurements on LAO/STO. The layout of this chapter is as follows: (i) I will first present the electrical characterization of the sample, (ii) I will then describe our model of the system, which can explain the observed behaviour of the magnetoresistance (MR) of the system, especially in relation to the coexistence of superconductivity and ferromagnetism, (iii) this is followed by a discussion of the observation of a novel manifestation of the phenomenon of charge-vortex duality, and (iv) finally, I will present data showing the magnetic field tuned superconductor-to-insulator transition (SIT) at the interface.

All the measurements presented here are taken on one LAO/STO sample grown in the lab of Prof. Chang-Beom Eom at the University of Wisconsin-Madison. Two Hall bars were fabricated on the sample, of the type shown in Fig. 3.8a, b. Although the measurements presented here were taken on one sample, subsequent measurements on other similar samples by other members of the group, Varada Bal and Sam Davis, have yielded results similar to the ones described here. In fact, some of the more striking phenomena reported here for the (001) sample, like the coexistence of superconductivity and ferromagnetism, have also been observed in (111) oriented samples in the group [**124**].

4.1. Electrical characterization

In this section I outline the electrical characteristics of the sample, through the results of measurements of the gate voltage dependent properties of the 2DEG at the interface. Before presenting the data on the gate voltage dependence of the properties, I describe the sample and measurement configuration used for acquiring the electrical transport data. As mentioned above, the sample had two Hall bars fabricated. Despite the fact that both the Hall bars were on the same substrate, and fabricated simultaneously, we observed dissimilarities in the values of some physical quantities, like resistance, of the two Hall bars. To demonstrate this, Fig. 4.1 shows the superconducting transition in R vs. T in both the Hall bars for a back gate voltage, $V_g = 80$ V (more on the gate voltage dependence below). As seen in the figure, the normal state sheet resistances, $R_\square$, of the two Hall bars, labeled 1 (blue circles) and 2 (red squares), differ by a factor of about 2. Sheet resistance, defined as $R_\square \equiv \rho/t$, is usually used for 2D materials of uniform thickness, t, as it gives a measure of the resistivity, ρ, independent of the sample size. Expressed in terms of the sheet resistance, the total resistance just becomes a function of the aspect ratio of the device and is specified by the number of "squares" in the device. We use the terms resistance and sheet resistance interchangeably in the following, with the quantity being referred to made clear by the context.

In fact, not only were the resistances of the two Hall bars different from each other, but two different sections on the *same* Hall bar had different resistances. This is seen in the data labeled "Hall Bar 1, 6 squares" (green diamonds), which is the superconducting transition of the section of the Hall bar between the leads V_1 and V_2 (see optical image

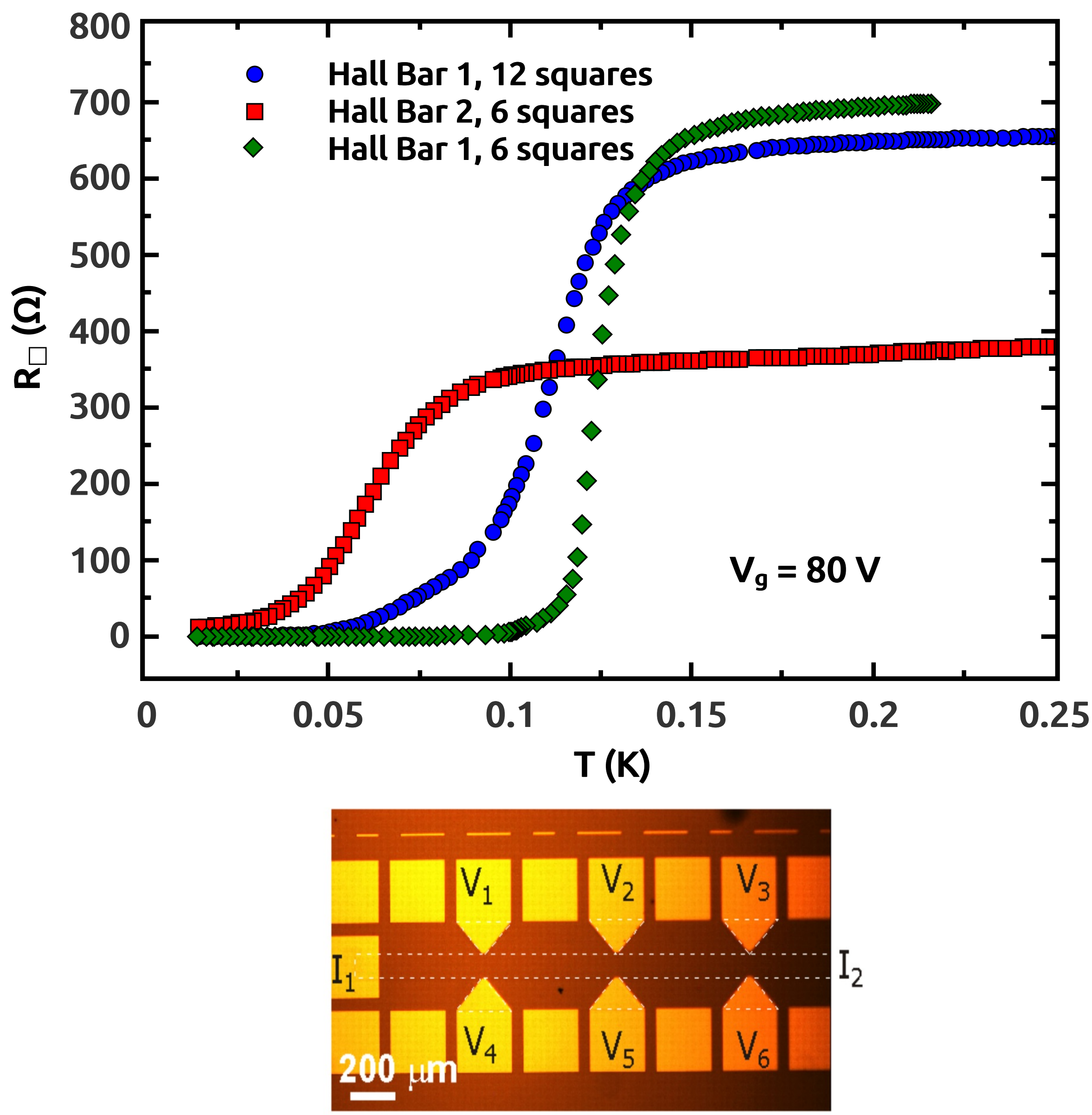

Figure 4.1. $R_\square$ vs. T for three different sections of the Hall-bars as described in the text. Different normal state resistances, $R_\square^N$'s, and different critical temperatures, T_C's, are observed for the three sections. An optical image of the Hall bar is shown at the bottom.

at the bottom of the figure), while the data labeled "Hall Bar 1, 12 squares" is the superconducting transition for the section between the leads V_1 and V_3.

Apart from the normal state resistances, the superconducting critical temperatures, T_C's, of the three sections are also quite different, as seen in the figure. What is truly surprising about the data is that the T_C of a lower resistance section is smaller and broader than the T_C of a higher resistance section. While there is no explanation for such behaviour at present, a detailed theory of superconductivity in this system may shed light on this odd behaviour. Such differences in the properties suggest an inhomogeneous distribution of electron density over the area of the sample. As explained in the theory chapter, such an inhomogeneous charge density could be caused due to an inhomogeneous distribution of oxygen vacancies or through a surface reconstruction resulting in a non-stoichiometric interface [**50**, **53**]. Another possible explanation for this is an intrinsic electronic phase separation in the system, of the kind observed in manganites [**125**, **126**] or cuprates [**127**, **128**]. Such an electronic phase separation has been proposed to explain some anisotropic magnetoresistance data in the LAO/STO system [**129**].

An important parameter that characterizes the observed inhomogeneity is its length scale, which is determined by the nature of interactions between the correlated electrons of the system and is not easy to quantify. For the LAO/STO system a range of length scales have been proposed, ranging from nanometers to micrometers [**11**, **50**, **129**–**131**], based on various local probe and X-ray diffraction experiments and theoretical studies. In our measurements of a globally averaged quantity like resistance over the sample dimensions that we have (100s of μms), we can cannot probe local variations over all such length scales. However, since we see variations in the transport properties for two sections on the same Hall bar which are separated by only a few μms, it is reasonable to assume that the length scale of inhomogeneities in our samples is at least of the order of a few μms. In addition, there could be variations over smaller length scales as well which we might be insensitive to, except through their effect on the resistance. In fact, inhomogeneities play a crucial role in our model of the system, which we develop later in the chapter.

The differences between the various sections of the Hall bars persisted up to room temperature, although the discrepancy in the values of the resistance showed a reduction. Table 4.1 summarizes the values of the two probe resistances at room temperature for the three sections shown in Fig. 4.1.

	Two probe resistance kΩ
Hall Bar 1, 6 squares	121
Hall Bar 1, 12 squares	225
Hall Bar 2, 6 squares	107

Table 4.1. Two probe resistance of the three sections of Hall bars measured at room temperature.

Since one of the sections of one of the Hall bars showed the sharpest transition and the highest T_C, we performed most of our subsequent detailed transport measurements on that section. However, we did confirm that the other sections also showed evidence for the salient transport features, like the superconducting transition, seen in this section. The dimensions of a section of the Hall bar with 6 squares were 600 μm (long) $\times$ 100 μm (wide). In reference to Fig. 4.1, the longitudinal voltage was measured between probes V_1 and V_2, while the transverse voltage (for Hall measurements) was measured between probes V_2 and V_5.

Another characteristic of the sample was a hysteresis in the resistance of the sample when a back gate voltage is swept. This is shown in Fig. 4.2 at a temperature of 24.8 mK. Such hysteresis has also been observed by other groups [**6**]. A possible source of this hysteresis is believed to be charge trapping in STO near the interface. Charge trapping has been proposed to explain the observed hysteresis in the polarization of STO thin films on the application of an electric field [**132**]. For the LAO/STO case, this mechanism can be understood as follows. As the applied electric field from a back gate voltage is increased, an increasing number of charges are induced at the interface. As described in the theory chapter, these charges are induced in STO due to its polarization in the applied electric field. Some of these charges may reside in localized defect states in STO near the interface, while others go into the mobile Ti 3d bands and contribute to conduction. When the electric field is reversed, some of these charges may still populate the defect states, modifying the local electric field and giving rise to the observed hysteresis. In the case of bare STO, the hysteresis vanishes at temperatures $>$ 260 K [**132**]; however, the observed hysteresis survives up to room temperature in our samples. While the hysteretic curve shown in Fig. 4.2 is independent of the gate voltage sweep rate at T = 24.8 mK, at room temperature the hysteresis is sweep rate dependent, with a larger hysteresis loop for faster sweep rates (data not shown). The size of the hysteresis may be reduced by "training" the interface with repeated sweeps of the gate voltage from one extreme to the other (± 100 V in our case). In view of the hysteresis, most of our gate voltage dependent measurements of magnetoresistance were performed as the gate voltage was decreased from +80 V to -100 V (in the direction of the up arrow in Fig. 4.2).

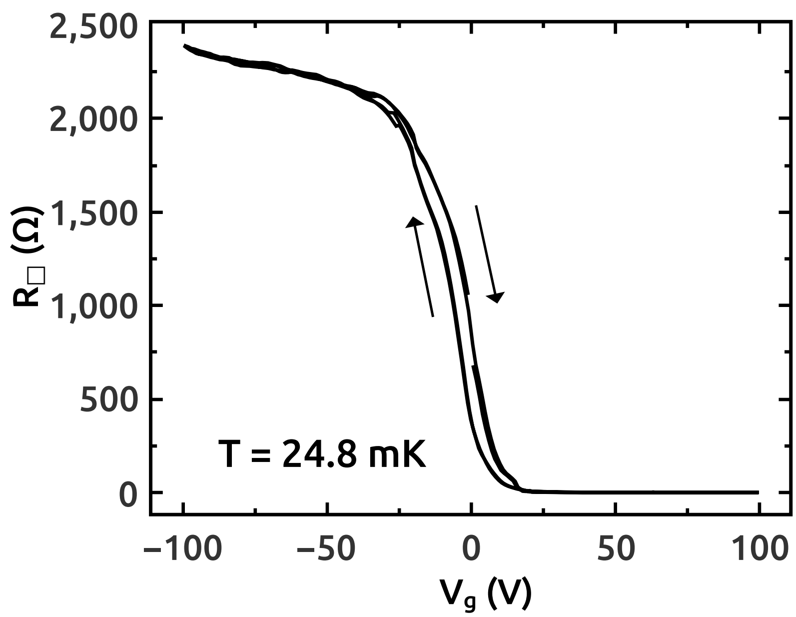

Figure 4.2. Hysteresis in the resistance of the sample as a function of the applied back gate voltage.

4.1.1. Hall measurements

As is seen above, the properties of the 2DEG at the LAO/STO interface can be tuned by the application of a back gate voltage, V_g [**4**, **6**, **10**, **79**, **100**]. The effect of the electric field due to V_g is to induce charges at the interface. As mentioned above, some of these charges occupy the itinerant Ti 3d bands in STO and contribute to the conduction charge density. One of the principal methods used experimentally to measure the charge density of a conducting system is a measurement of the Hall effect [**133**]. Our sample geometries are specifically designed to measure the Hall voltage generated in the LAO/STO 2DEG (our devices are actually called Hall bars for this very reason). For the measurement of the Hall voltage a magnetic field is applied perpendicular to the plane of the sample, while an electric current flows along the long axis of the Hall bar. The resultant voltage developed across the short axis of the Hall bar is the Hall voltage. According to the Hall effect, the ratio of the induced Hall voltage, V_{Hall}, to the product of the current and the applied magnetic field, IH, is a constant dependent on the density of charge carriers. This constant is called the Hall coefficient, and for conduction through a single band is given by, $R_H = 1/nq$, where n is the density of the charge carriers and $q = \pm e$ is the charge of the carrier ($q = +e$ for holes and $q = -e$ for electrons). The same relation holds for 2D materials, with n representing the areal density, which is how we use it.

Experimentally the Hall coefficient is determined from the slope of the transverse Hall resistance, R_{xy} (dV/dI) vs. H curve ($R_H = \text{slope}(R_{xy}, H)$). Figure 4.3 shows the measured Hall resistance, R_{xy}, as a function of the applied field $H_\perp$ for different V_g's. Figure 4.3**a** shows data taken at $T = 50$ mK, while Fig. 4.3**b** shows data taken at $T = 270$ mK. Since the sign of the Hall coefficient is determined by the sign of the slope of R_{xy} vs. H, it is important to accurately know the direction of the field generated by the superconducting magnet in relation to the direction of current flow, and the polarity of the differential voltage probes. An error in this knowledge would result in an erroneous sign of R_H giving the wrong sign of the charge carrier. In order to figure out the direction of the field generated by the superconducting solenoid magnet, we used a Hall probe magnetometer to measure the polarity of the magnetic field generated by the solenoid.

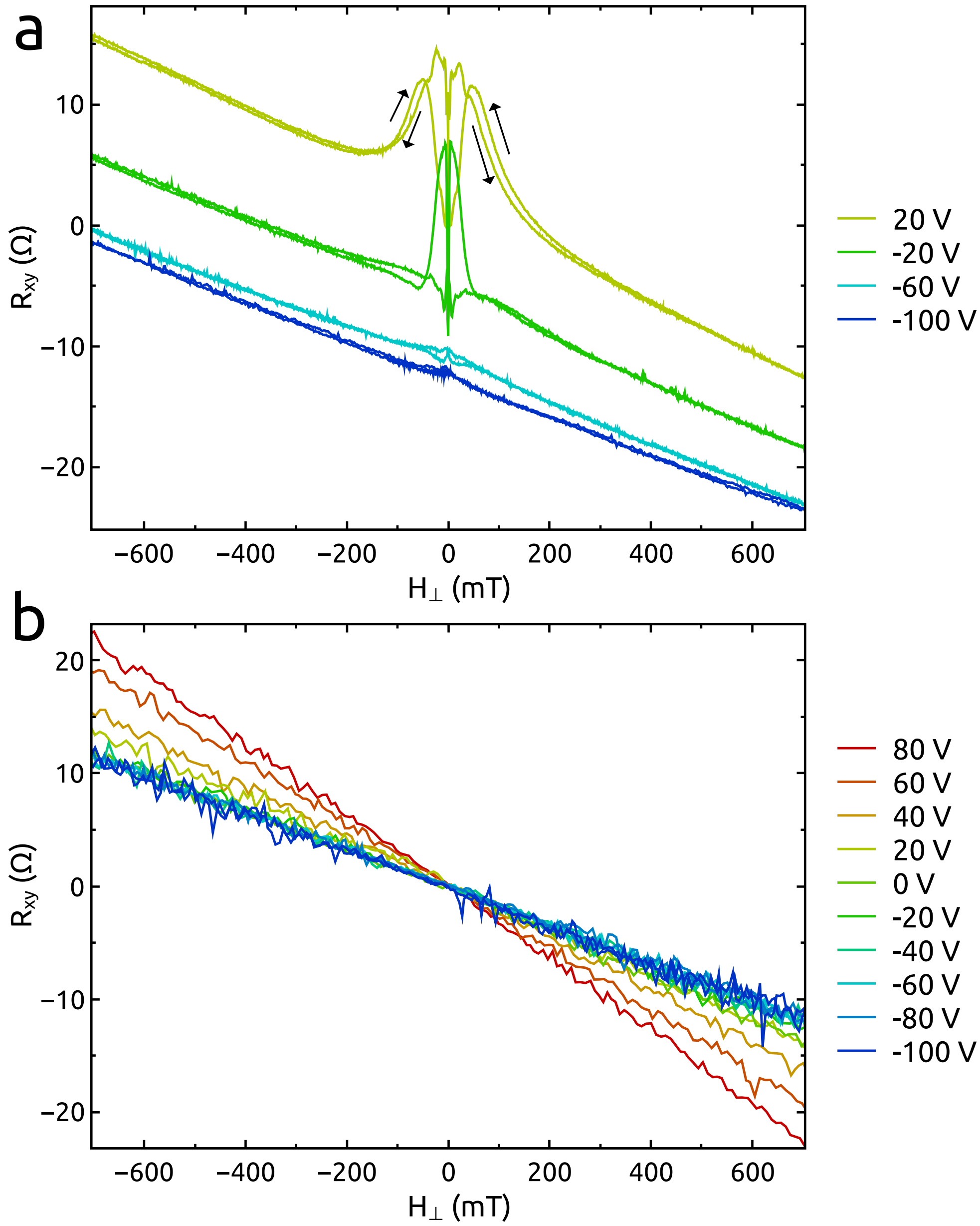

Figure 4.3. The Hall resistance, R_{xy}, as a function of the field for different gate voltages at **a)** 50 mK and **b)** 270 mK. The arrows indicate the direction of field ramp in **a)**. The low field non-linear, hysteretic Hall is present at 50 mK but not at 270 mK. Therefore, in **b)** data are shown for field swept in only one direction. The offset in R_{xy} has been subtracted for all the curves in **b)** (see text for details). The slope of the high field linear background at 50 mK is equal to the slope of the linear curves at 270 mK for the corresponding gate voltages.

Knowing the direction of the current flow and the polarity of the voltage probes, and with the knowledge of the polarity of the field, we are confident of the negative sign of the slope of the curves presented in Fig. 4.3.

As seen in Fig. 4.3**a**, the low field R_{xy} is highly non-linear and hysteretic for V_g = 20 and -20 V, while both, the non-linearity and the hysteresis reduce significantly for V_g = -60 and -100 V. The non-linear, hysteretic behaviour in R_{xy} is attributable to magnetization dynamics of the ferromagnet of the system inducing magnetic flux in the electron system. The model of how ferromagnetic dynamics cause hysteresis in magnetoresistance in this system is discussed later in the chapter. For now, we only concentrate on the high field linear part of R_{xy}, from which we can obtain the density as described above. Another aspect of Fig. 4.3**a** is the value of R_{xy} at $H_\perp$ = 0 mT. Ordinarily, one would expect the zero field Hall resistance to be zero. We, however, see a finite offset value of R_{xy} even for V_g = -60 and -100 V, where the hysteresis is small. (Note that any offsets in the measurement instruments were much smaller than the offsets seen in the data in R_{xy}.) The reason for this is a small misalignment between the transverse voltage leads (leads V_2 and V_5 from Fig. 4.1), which gives rise to a small contribution of longitudinal resistance, R_{xx}, to the Hall resistance. The misalignment also accounts for a large fraction of the hysteresis seen in R_{xy}. About 90 % of the hysteretic MR in R_{xy} is due to similar hysteretic behaviour in the longitudinal resistance. From the magnitude of the offset in R_{xy} at $H_\perp$ = 0 mT, we estimate a misalignment of less than 1 μm between the two transverse voltage probes. By imaging the fabricated Hall-bars using a scanning electron microscope (SEM), we see that the misalignment of the voltage probes is less than $\sim$ 1.5 μm (although such a measurement was not done on the sample presented here, subsequent samples fabricated using the same Hall bar pattern yielded the misalignment reported here).

If the temperature of the system is raised to $T = 270$ mK, well above the highest superconducting critical temperature in the system ($T_C^{max} \sim 140$ mK), it is found that the hysteresis in R_{xy} vanishes at all V_g's, or even if it is present, it is buried in the noise, and only a linear R_{xy} remains as shown in Fig. 4.3**b**. The corresponding R_{xx} might still show some small hysteresis (hysteretic longitudinal magnetoresistance data is discussed in detail later). While the hysteresis disappears at $T = 270$ mK, one still has the offset in R_{xy} at $H_\perp = 0$ mT. However, in Fig. 4.3**b**, we have artificially made the offset zero at zero field in order to clearly show the dependence of the slope of R_{xy} vs. $H_\perp$ as V_g is varied. It should be noted that the slopes obtained from fits to the high field linear background of Fig. 4.3**a** are the same as the slopes from the linear fits to curves of Fig. 4.3**b** for the respective V_g's. One can see a clear trend in the evolution of the slope, which is the Hall coefficient R_H, as V_g is varied, if one fits the curves in Fig. 4.3**b** with lines, extracts the slopes and plots them as a function of V_g.

This is done in Fig. 4.4, which shows R_H as a function of V_g at $T = 270$ mK. The sign of R_H suggests electron like carriers. The figure also shows the measured sheet resistances of the 2DEG, tuned by V_g at $T = 250$ mK. Both these temperatures are close and it is assumed there is not much difference in the properties of the system between these two temperatures. (Also, as mentioned above, this temperature scale is above the highest measured T_C in the superconducting state, ~ 140 mK, so superconducting fluctuations

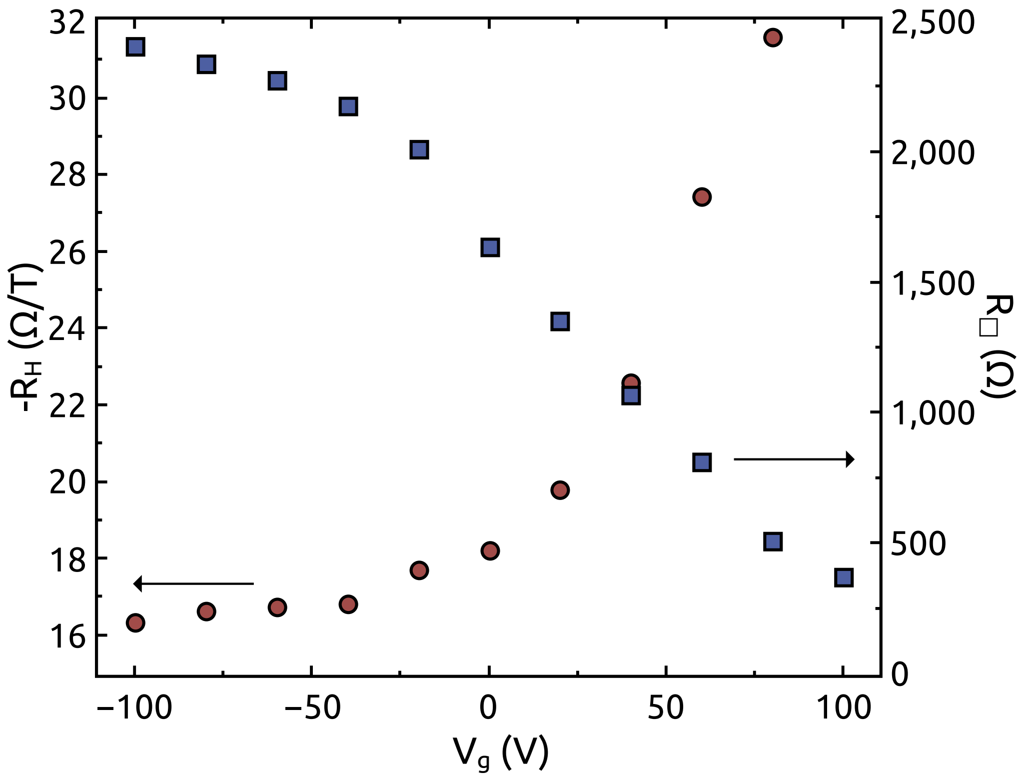

Figure 4.4. Dependence of the slope of the Hall coefficient, $-R_H$ (red circles), and the sheet resistance, $R_\square$ (blue squares), on the gate voltage. The line is a fit to the Hall data calculated from the two band model. The temperature for the Hall data was $T = 270$ mK, while the sheet resistance was measured at $T = 250$ mK.

can be neglected.) It is seen that the two curves have opposite dependences on V_g. If only electron like carriers were present at the interface, one would expect an increasing V_g would result in a proportional increase in the density of electron at the interface. Thus, for only electron like carriers, one would expect a decrease in both $R_\square$ and R_H. However, as is seen in the figure, while $R_\square$ does indeed decrease, R_H increases with increasing gate voltage.

It will be recalled from Chapter 2 that the electron like carriers in this system occupy multiple Ti 3d bands. However, since all of those bands are electron like they cannot explain the observed trend of R_H with V_g, unless one assumes a non-monotonic dependence of the induced charge density on the gate voltage. It is not clear what such a mechanism could be, so we do not consider it. However, there are groups which do postulate a non-monotonic dependence of the electron density on the gate voltage in order to explain their Hall data [**134**]. Such contrasting behaviours of $R_\square$ and R_H can be understood if one assumes the presence of at least one hole band that contributes to the transport. Therefore, in order to explain the R_H vs. V_g trend, we propose the existence of a hole band whose density and mobility contributes to the transport in such a way as to give rise to the observed trend in R_H. Table 4.2 shows the calculated electron charge density, n_e, extracted from the R_H values, assuming transport through a single electron-like band. The densities extracted match well with those reported by other groups [**4**–**6**, **33**, **135**].

4.1.2. The gate voltage tuned superconductor-insulator transition

One of the more interesting effects of tuning the charge density of the system by the gate voltage is the inducement of a superconductor-insulator transition (SIT) in it. As discussed in Chapter 2, the SIT is a type of quantum phase transition (QPT), and has been studied extensively in the past for a variety of 2D superconductors [**85**–**96**]. It continues to remain a topic of research even today due to a lot of unresolved issues relating to the nature of the insulating state. Although the nature of the state reached on destroying superconductivity by the gate voltage in this system is still being debated, we call it

V_g V	n_e $\times\ 10^{13}$ cm^{-2}
80	1.97
60	2.27
40	2.76
20	3.16
0	3.43
-20	3.53
-40	3.71
-60	3.74
-80	3.76
-100	3.83

Table 4.2. Densities extracted from the Hall data assuming a single electron-like band.

the insulating state since to the lowest measured temperature we find $dR/dT < 0$ (more on the insulating state below). An advantage of the gate dependent properties of the LAO/STO interface is the relative ease with which the SIT can be studied in it. Unlike in some of the other systems studied, where the SIT is induced by varying the physical thickness of the superconducting film through an involved film deposition process in the dilution fridge [**87**, **88**], in the LAO/STO system one just turns a knob controlling the applied gate voltage to the sample. Below I present our observation of the gate tuned SIT in this system.

4.1.2.1. Nature of the superconducting state. Figure 4.5 shows the gate voltage tuned SIT in two different types of measurements: Fig. 4.5**a**, **b** and **c** show the temperature dependence of the resistance, $R_\square$ vs. T, of the system as V_g is varied, while Fig. 4.5**d** shows the dc current-voltage, $I-V$, characteristics. Using the terminology of Fig.

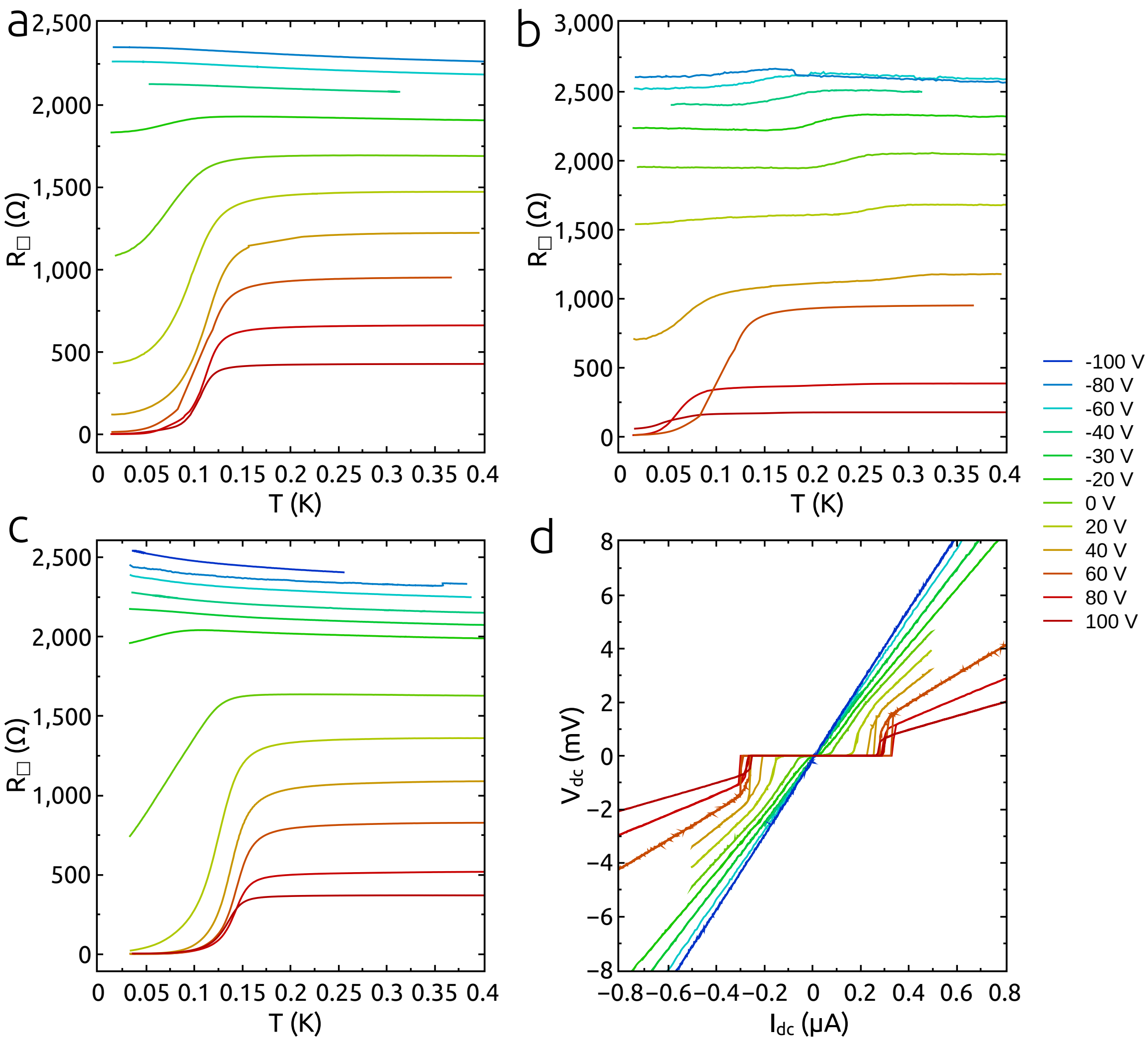

Figure 4.5. Back gate voltage tuned SIT in the system as seen in the $R_\square$ vs. T dependence (**a**, **b** and **c**) and V_{dc} vs. I_{dc} dependence (**d**). Using the terminology of Fig. 4.1, **a)** is for "Hall Bar 1, 12 squares", **b)** is for "Hall Bar 2, 6 squares" and **c)**, **d** are for "Hall Bar 1, 6 squares." The temperature for the data in **d)** is 15 mK. The legend shows the different V_g's.

4.1, Fig. 4.5**a** is for "Hall Bar 1, 12 squares", **b** is for "Hall Bar 2, 6 squares" and **c** is for "Hall Bar 1, 6 squares." As mentioned earlier, the three different sections have different $R_\square$'s and T_C's. To study the SIT we will focus on the section "Hall bar 1, 6 squares."

The $I-V$ characteristics in **d** are for that section.

In Fig. 4.5**c** it is seen the the superconducting state of the SIT is induced for $V_g >$ -30 V, while below that gate voltage the system is insulating. As can be seen the gate voltage not only tunes the normal state sheet resistances, but also tunes the superconducting critical temperatures, T_C's (following convention, we define T_C as the mid-point of the resistive transition). However, while the sheet resistances decrease monotonically with increasing gate voltage, the critical temperature has a non-monotonic dependence and peaks at a certain gate voltage, $V_g \simeq 70$ V. It will be recalled that even in the case of reduced STO discussed in Chapter 2, T_C showed similar dependence on the carrier density (Fig. 2.3). That was attributed to an increased "$N(0)V$" term of the BCS theory, due to the multiple conduction bands in the system (see Chapter 2). It is reasonable to believe that a similar scenario occurs in the LAO/STO system, which gives rise to the "dome-" shaped behaviour of T_C. This dependence is shown in Fig. 4.6. Such a "dome-" shaped behaviour is also observed in the measured I_C's, where we define I_C as the current at which a non-zero voltage ($= 20\ \mu$V) appears across the sample, as the current is increased. Theoretically it is predicted that the resistance at which the SIT occurs, i.e., the resistance which separates the superconducting and insulating states, is the quantum of resistance for pairs, $R_Q \equiv h/(2e)^2 = 6.45$ kΩ [**85, 86**]. However, like for many low resistance systems [**90, 136**], we find that the resistance at which we see the transition is smaller than this resistance, $R_{\square}^{SIT} \simeq 2.1$ kΩ.

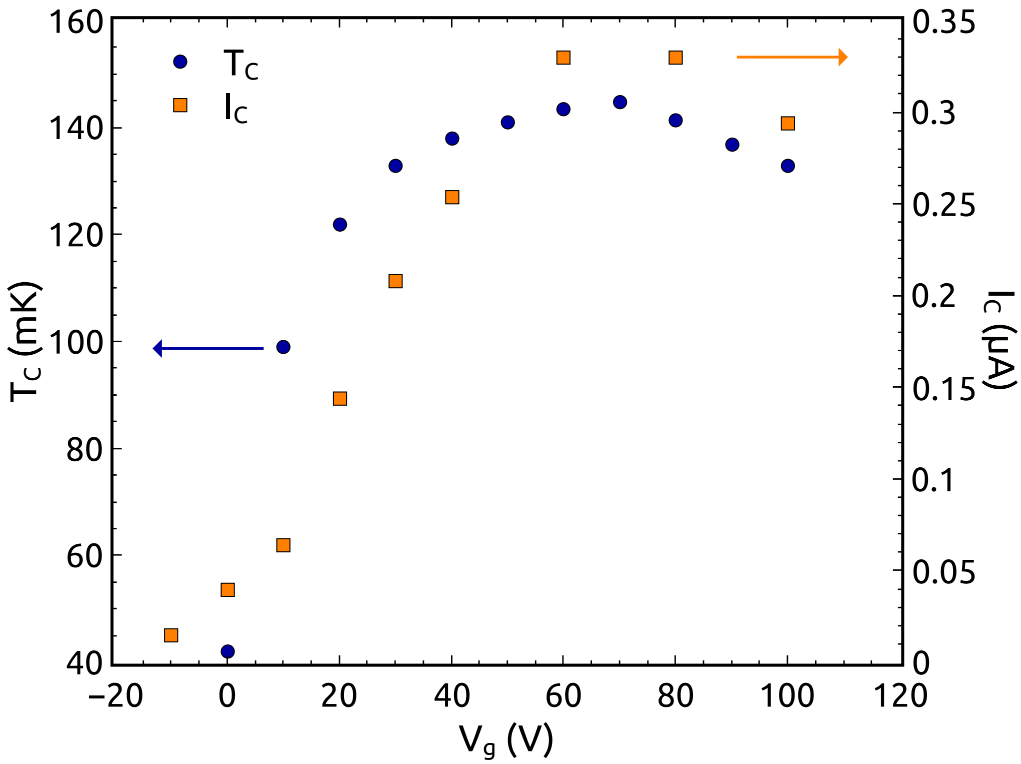

Figure 4.6. Non-monotonic ("dome"-shaped) dependence of T_C and I_C on the gate voltage extracted from the data in Figs. 4.5**a** and **b**. T_C is defined as the mid-point of the resistive transition, and I_C is defined as the current at which a non-zero voltage appears across the sample, as the current is increased.

As mentioned in Chapter 2, a 2D superconductor usually shows a Berezinskii-Kosterlitz-Thouless (BKT) transition [**103**], which is basically a transition of the system from a state of frozen bound vortex-antivortex pairs at a lower temperature to a state with mobile vortices and antivortices at a higher temperature. The temperature at which this transition occurs is called the BKT transition temperature, T_{BKT} which is less than T_{C0}, where T_{C0} is the Ginzburg-Landau transition temperature below which the order parameter value becomes non-zero. The experimentally determined T_C, defined as the mid-point of the resistive transition, is usually less than T_{C0}, with the difference determined by the material properties [**137**]. Due to the movement of vortices above T_{BKT} a finite resistance develops in the system even though there is a fully formed gap in the system, as discussed in Chapter 2. The BKT transition is characterized by the following dependence of the resistance of the system on temperature [**5**],

$$\left(\frac{d\ln R}{dT}\right)^{-2/3} = b\left(\frac{T}{T_{BKT}} - 1\right)$$

where b is some material dependent parameter. Using the data of Fig. 4.5**a**, we find that $T_{BKT} \lessapprox T_C$ in our system for all gate voltages at which the system is superconducting and which lie below the gate voltage at which the T_C peaks in Fig. 4.6, i.e., for $V_g < 70$ V. For gate voltages, $V_g > 70$ V, we find that $T_{BKT} \gtrapprox T_C$. Such behaviour is surprising and may have to do with the definition of T_C as the midpoint of the resistive transition. For T_C defined as the temperature at which one starts to see a downturn in resistance, we find $T_{BKT} \lessapprox T_C$ for all V_g's. In any case, such a close match in T_{BKT} and T_C is expected for a low resistance system like ours [**138**]. At $V_g = 40$ V, the lowest measured gate voltage at which one sees a zero resistance superconducting state (see Fig. 4.5), the normal state resistance, $R_\square^N \sim 1$ k$\Omega < R_Q$, the quantum of resistance for pairs, which sets the scale for resistance in 2D superconductors. Figure 4.7 shows $(d\ln R/dT)^{-2/3}$ vs T for $V_g = 60$ V, as a representative curve to show how T_{BKT} is determined.

4.1.2.2. Nature of the insulating state. Unlike in the case of highly resistive systems which show the 2D SIT [**87**, **88**, **92**], in the LAO/STO system the insulating state is relatively "weak." This is seen in the R vs. T dependence in Fig. 4.5a for V_g = -30, -40,

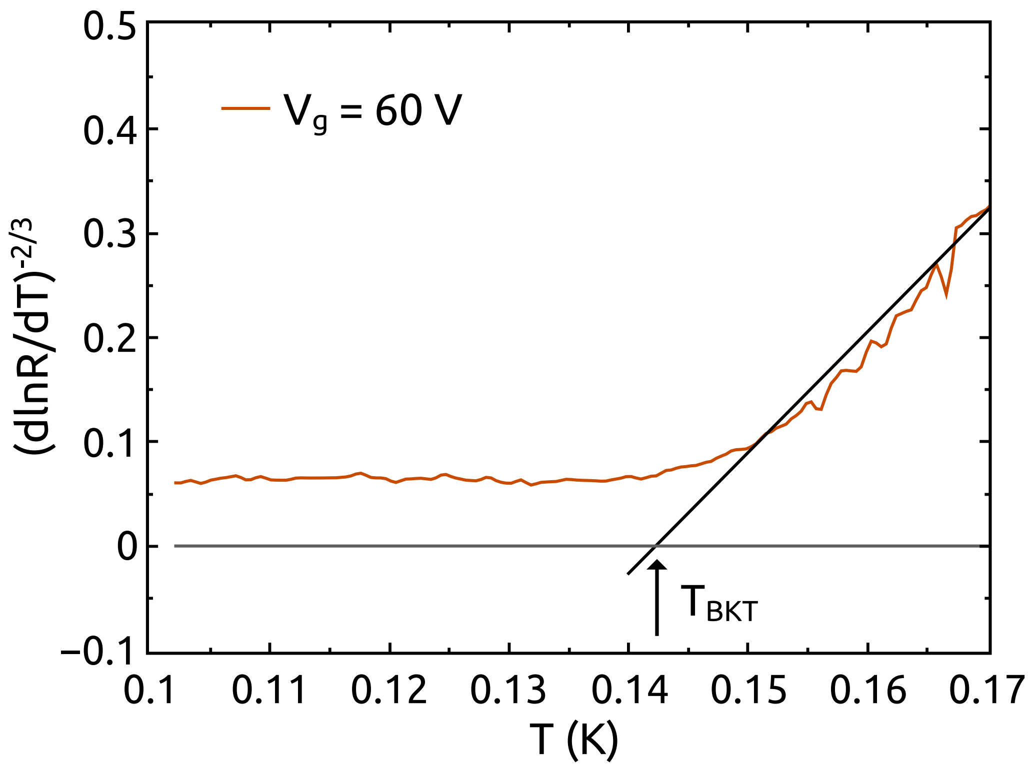

Figure 4.7. $(d\ln R/dT)^{-2/3}$ vs T for V_g = 60 V for the determination of T_{BKT}. The black line is a linear fit to the data in the temperature range above the upturn in $(d\ln R/dT)^{-2/3}$. T_{BKT} is identified as the temperature at which a linear fit to $(d\ln R/dT)^{-2/3}$ intersects zero as shown.

-60, -80, and -100 V. Although it is possible that a strongly insulating state lies beyond our minimum applied gate voltage of V_g = -100 V, such a scenario is ruled out by data from other groups. A weak dependence of resistance on the temperature in the insulating regime has also been observed by other groups in this system [**6**, **135**, **139**], even for gate voltages as low as V_g = -300 V [**6**, **139**]. A possible explanation for this is the non-linear dependence of the permittivity of STO at higher fields. As reported by Neville *et al.* [**22**], the permittivity of STO reduces by an order of magnitude under the application of large electric field of the sort applied in our samples ($\sim 10^5$ V/m). Thus the effective field at the interface may be reduced, resulting in a weakly insulating state. However, similar experiments performed in the LAO/STO (111) samples in our group do show a strongly insulating phase [**124**], implying that the reduction of the permittivity may not be a sufficient cause to explain the weak insulating behaviour.

In order to analyze the weakly insulating state, one can estimate the contribution to resistance due to weak localization (WL) [**140, 141**]. As an example, we take the gate voltage, V_g = -100 V. The change in resistance in the presence of magnetic field from weak localization effects in 2D is given by [**79, 142**],

$$\frac{\delta R^{loc}}{R}(H) = \frac{R_\square}{2\pi^2\hbar/e^2}\left[-\frac{3}{2}f_1(H_2) + \frac{1}{2}f_1(H_\phi)\right] \tag{4.1}$$

where

$$f_1(H_i) = \psi(1/2 + H_i/H) - \ln(H_i/H)$$

and ψ is the digamma function, $H_2 = H_\phi + (4/3)H_{so}$, $H_\phi = \Phi_0/8\pi L_\phi^2$ and $H_{so} = \Phi_0/8\pi L_{so}^2$ are the various magnetic field scales dependent on the lengths L_ϕ and L_{so}. Here, L_ϕ is the electron phase coherence length and L_{so} is the spin-orbit scattering length. Note that the equation above is an implicit function of temperature through the dependence of L_ϕ and L_{so} on temperature. Fitting the above equation to the magnetoresistance data at different temperatures, one can obtain the values for the two length scales. Figure 4.8 shows the measured $\Delta R/R$ vs. $H_\perp$ at V_g = -100 V for two temperatures, T = 400 mK and T = 50 mK. (In order to obtain the data shown in the figure, a small parallel field of $H_\parallel$ = 100 mT was applied to suppress magnetization dynamics in the ferromagnet which cause hysteresis in the perpendicular field magnetoresistance as explained later.) The figure also shows a fit to the data using the equation above. From the fitted curves one obtains at T = 50 mK, L_ϕ = 93 nm and L_{so} = 53 nm, and at T = 400 mK, L_ϕ = 60 nm and L_{so} = 42 nm. From a knowledge of the fit values and the temperature dependence of L_ϕ, $L_\phi \sim (T\ln T)^{-1/2}$, a positive contribution to the resistance of $\sim$ 200 Ω is calculated as the temperature is decreased from a reference temperature, T_{ref} = 400 mK to T = 50 mK. However, the observed rise in resistance at V_g = -100 V between these two temperatures is $\sim$ 800 Ω (see Fig. 4.5**a**). Hence the increase in resistance cannot be accounted for by the weak localization corrections alone. One must take into account other mechanisms that contribute to the increase in resistance.

For highly resistive systems that show the 2D SIT, the temperature dependence of the resistance in the insulating state is usually characterized by (i) Mott variable range hopping behaviour, $R = R_0 \exp(T_0/T)^{1/d+1}$, where d is the dimension of the system (d = 2 for 2D) and R_0 and T_0 are constants [**143, 144**] or (ii) activated behaviour over some form of Coulomb charging gap, $R \sim \exp(\Delta_C/k_B T)$ [**145**]. Both of these dependences give rise to a rapid rise in the resistance at lower temperatures, unlike what we see (Fig. 4.5a). We were unsuccessful in trying to fit our data to any of the dependences above.

Another possible source for the rise in resistance that we see may be electron-electron interactions (EEI) as understood in the context of disordered electronic systems [**140,146**]. EEI contributions to the resistance result in a logarithmic dependence of the resistance on the temperature, much slower than the two mechanisms above. However, we find that the

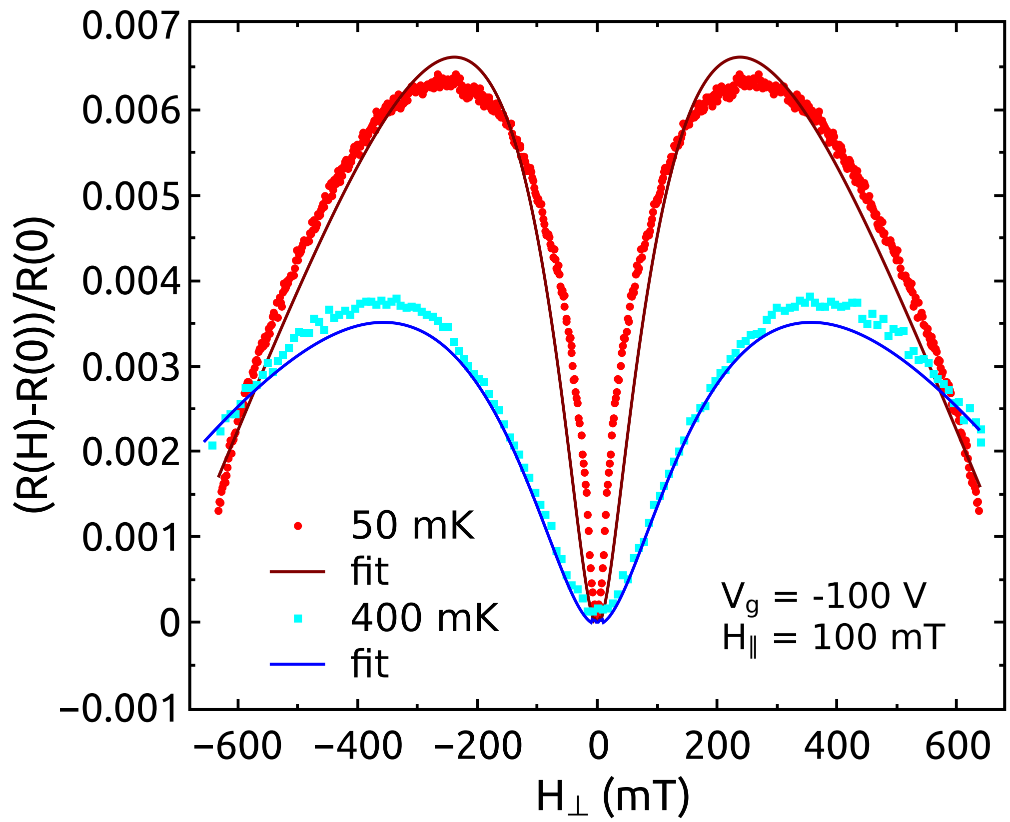

Figure 4.8. $R(H) - R(0)/R(0)$ vs $H_{\perp}$ for V_g = -100 V at T = 50 (red circles) and 400 (cyan squares) mK in a constant parallel field, $H_{\parallel}$ = 100 mT. The solid lines are the fits to the two curves using Eqn. 4.1.

resistance of our sample in the insulating regime, has an even slower dependence than $\ln T$ at low temperatures. This is shown in Fig. 4.9a, where we plot $R_{\square}$ vs $\ln T$ for V_g = -100 V. We find that for $T <$ 70 mK, the resistance deviates from the $\ln T$ behaviour as shown in the figure. Such behaviour might indicate the effects of superconducting fluctuations on the resistance which result in a lowering of the resistance from the logarithmic increase expected with decreasing temperature. In fact we do see evidence for superconductivity in the insulating regime, i.e., for gate voltages at which one observes $dR/dT < 0$ in the R vs. T dependence for the lowest measured temperatures (see Fig. 4.5a). This is shown

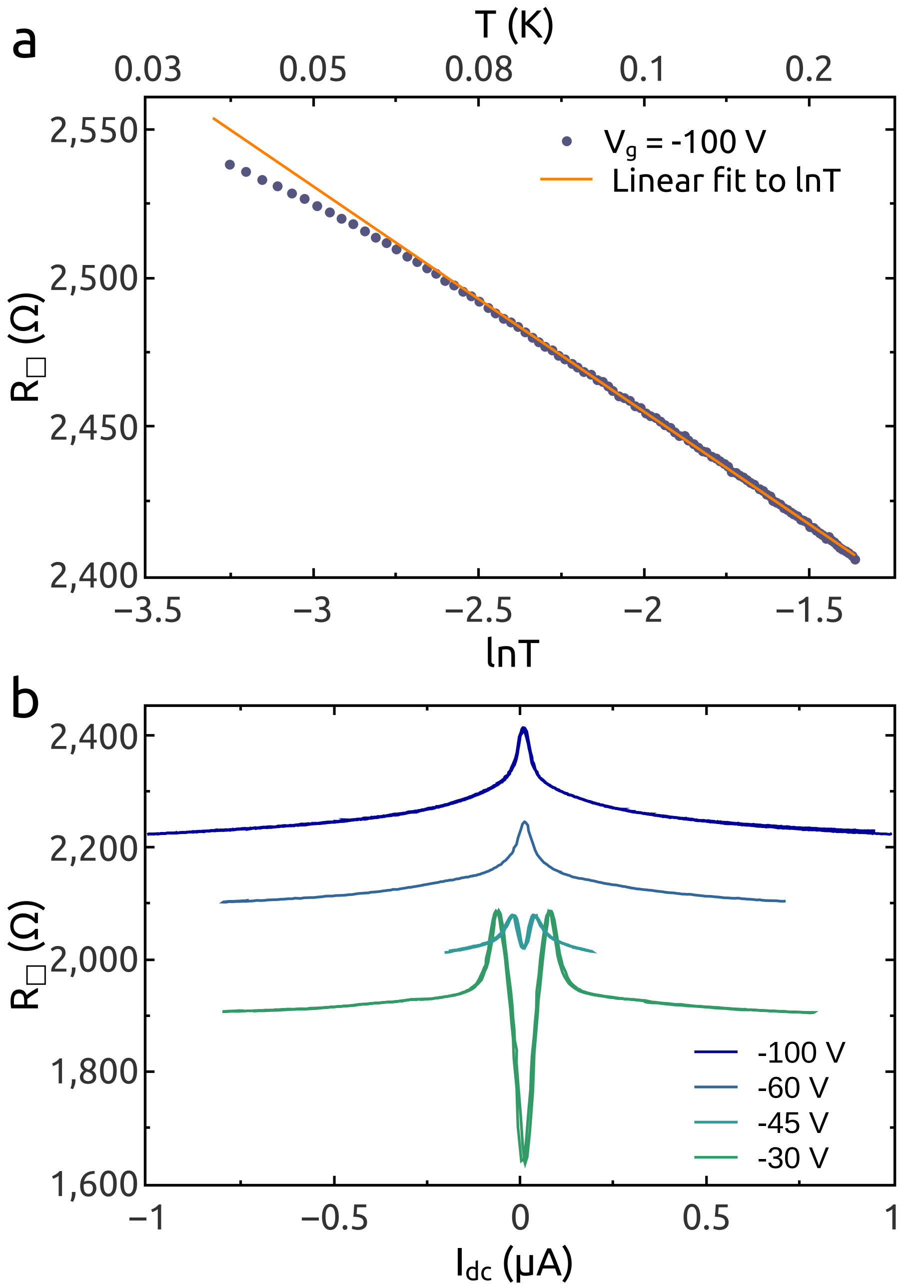

Figure 4.9. **a)** $R_\square$ vs $\ln T$ for V_g = -100 V. The top axis shows the corresponding temperature. The orange line is a linear fit to the data. The data deviates from the $\ln T$ dependence for T < 70 mK. **b)** Evidence for the existence of superconducting puddles in the insulating regime seen in dV/dI vs. I_{dc}. Details in the text. T = 50 mK.

in the dV/dI vs. I_{dc} dependence for various V_g's in the insulating regime in Fig. 4.9b. For V_g = -30 and -45 V, a dip in dV/dI at zero bias signifies the presence of some superconductivity, however no evidence for that is seen in the temperature dependence of the resistance since $dR/dT < 0$ at the lowest temperature measured. The dip in dV/dI probably arises due to localized superconducting islands weakly phase coupled by the Josephson effect, as described in the next section. For V_g = -60 and -100 V, the system is nominally in the insulating regime but superconducting fluctuations may still affect the transport properties and cause a decrease in resistance from the $\ln T$ behaviour as seen in Fig. 4.9a.

It appears from the above discussion of the insulating state that multiple mechanisms contribute to the resistance observed. It is difficult to estimate the proportion of each of them accurately, principally because of the inhomogeneous nature of the system, locally different mechanisms may contribute with different weights to the total resistance. Additionally, we do not know the size of the superconducting gap that survives into the insulating regime and whether it changes with V_g. Also, although we see no evidence for a macroscopic Coulomb charge gap in the insulating regime, the existence of the superconducting islands on the insulating side of the SIT implies that there would be a microscopic charging energy associated with these islands. Based on this we develop the $E_J - E_C$ model of the SIT in the next section.

Before presenting the next section, though, I would like to digress briefly to make a few comments on the analysis of the gate voltage tuned magnetoconductance as presented in Ref. 32. That work has been highly cited in the literature in this field, with its results forming the basis for some of the theories developed for the superconducting state in the system as discussed in Chapter 2 (model of Michaeli *et al.* [**72**]). However, it is possible that its conclusions may be misleading, as reasoned in the following. In Ref. 32 Caviglia *et al.* analyze their MR data using the Maekawa-Fukuyama theory [**147**] which is the same as the equation presented above for WL corrections if Zeeman effects are neglected. From the fits to their magnetoconductance (which is the inverse of MR), they obtain the inelastic scattering time τ_i, and the spin-orbit scattering time τ_{so} as functions of the gate voltage. Their fitted magnetoconductance data and the extracted parameters are shown in Fig. 4.10a and b. As seen in the figure, the shape of their magnetoconductance curve at V_g = -50 V and -100 V is very similar to the shape of our MR curve shown in Fig. 4.8, although the field scales are different (the MR curve has to be inverted in order to compare it to the magnetoconductance curve). (Note that what they call the inelastic time should actually be the dephasing time, $\tau_\phi = {L_\phi}^2/D$, where D is the diffusion coefficient.) Also, for reference, the spin-orbit time obtained from a fit to our data above is $\tau_{so} \approx 10$ ps for $L_{so} = 53$ nm, see above.

The most striking aspect of their analysis of the magnetoconductance is the more than 2 orders of magnitude change in τ_{so} as a function of V_g, which is the basis of the model of superconductivity by Michaeli *et al.*, while τ_i remains essentially constant (Fig. 4.10b). While it is possible that these two scattering times vary with the gate voltage as they report, there is reason to believe that the way they fit their curves using the theory may give misleading results. This is because they let both τ_{so} and τ_i act as free parameters for the

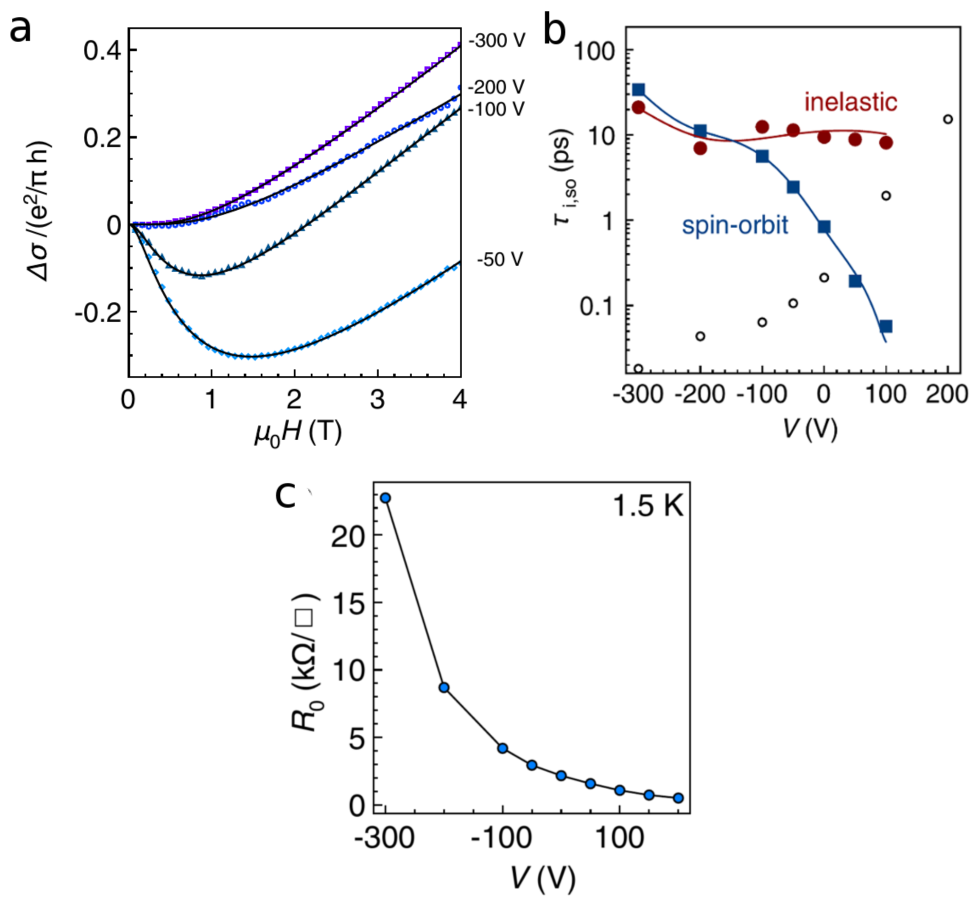

Figure 4.10. **a)** Best fits according to the Maekawa-Fukuyama theory of the variation of conductance, in units of $e^2/\pi h$, for different gate voltages. **b)** Inelastic relaxation time, τ_i (red circles) and spin relaxation time τ_{so} (blue squares) as a function of gate voltage plotted on a logarithmic time scale. The lines are a guide to the eye. The magnetoconductance data were obtained at $T = 1.5$ K. **c)** Sheet resistance modulation resulting from the field effect measured at 1.5 K. Figure and caption adapted from Ref. 32.

fit. However, it is expected that τ_i depends on the resistivity, $\tau_i \propto R_\Box$ at a fixed temperature [**123**]. Since their resistance changes by a factor of ~ 40 between the two extremes of their applied gate voltage (Fig. 4.10c), one should see a concomitant change in their τ_i between these two V_g's, which they do not obtain from their fits. Thus the large change in τ_{so} that they report may not be that large if a variation in their τ_i is taken into account.

We now look at the $E_J - E_C$ model of the SIT.

4.1.2.3. The $E_J - E_C$ model of the SIT. Although the disorder tuned 2D SIT is theoretically predicted to be a universal quantum phase transition [**85**, **86**], in practice different samples demonstrate different transition characteristics, like the resistance at which the transition occurs and the nature of the insulating state. These differences occur due to the effects of the details of the microscopic disorder on the SIT. It is difficult to quantify this microscopic disorder except though a sample-averaged macroscopic quantity like resistance. However, a useful model that can account for some of the microscopic interactions in the sample is the so-called $E_J - E_C$ model [**148–150**]. A schematic of the model is shown in Fig. 4.11. This model is especially useful to describe the SIT in granular and inhomogeneous systems, and as shown above, our sample is indeed inhomogeneous.

As shown in Fig. 4.11, the system is modeled as a random network of superconducting islands embedded in a non-superconducting matrix. The surrounding material can either be weakly or strongly insulating. There are two competing energy scales in the problem: the Josephson coupling energy between the islands, E_J, and the Coulomb charging energy, E_C, which is the energy cost of adding a Cooper pair on an island. Here by the Josephson coupling energy, I mean the strength of the interaction between neighbouring superconducting grains. This interaction is based on the Josephson effect, which in this

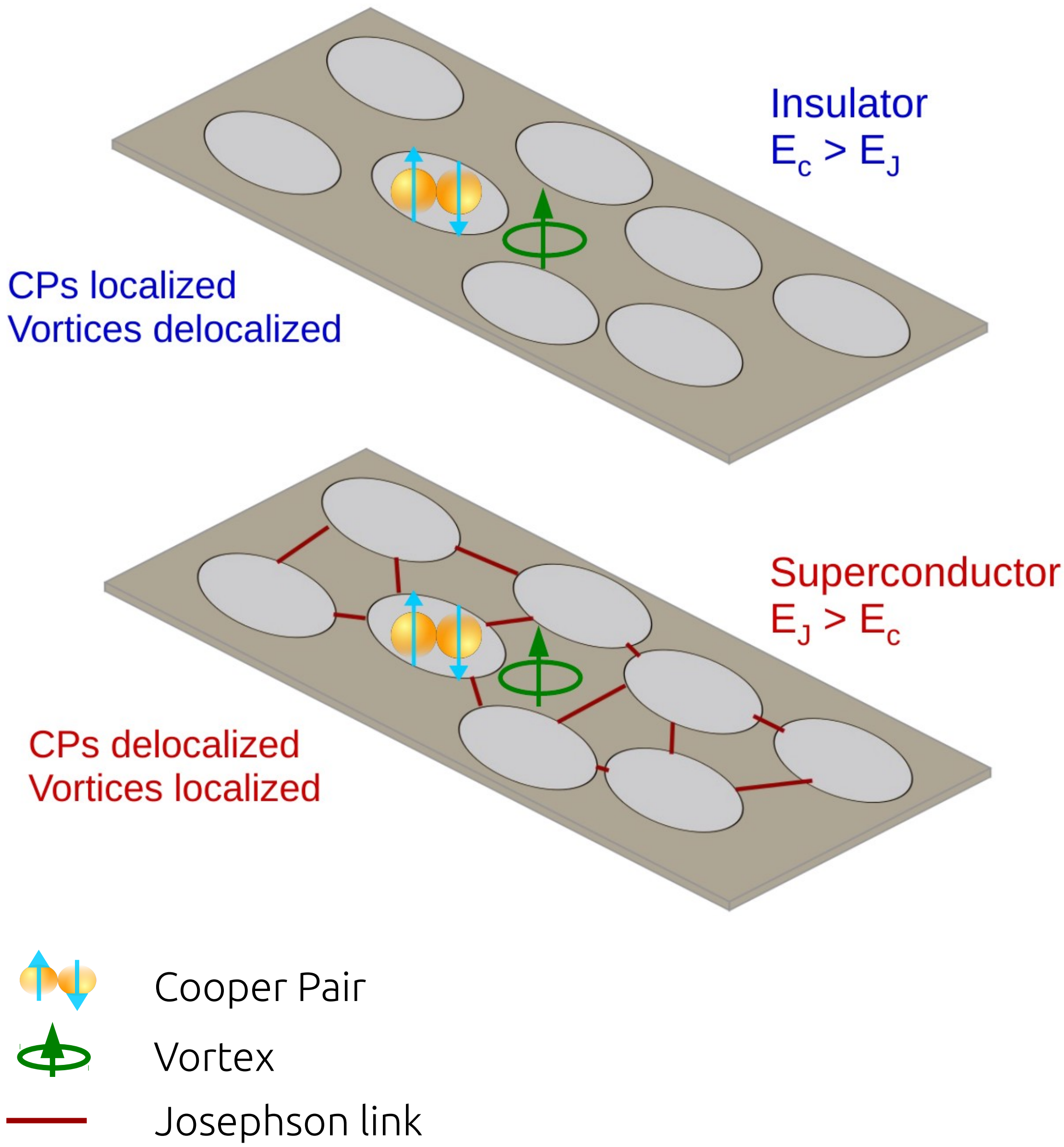

Figure 4.11. The $E_J - E_C$ model of the SIT. In the superconducting state $E_J > E_C$ and the Cooper pairs are delocalized through the sample, while in the insulating state $E_J < E_C$ and the Cooper pairs are localized on the individual superconducting islands.

case is basically the quantum mechanical tunneling of Cooper pairs between two superconductors separated by an insulating barrier. The ratio E_J/E_C determines the ground state of the system. When E_J is greater than E_C , the system is superconducting and the Cooper pairs are delocalized through the sample, and when E_J is less than E_C the system becomes insulating, with the Cooper pairs localized to the individual grains. In our case, the ratio E_J/E_C is tuned by the gate voltage giving rise to the observed SIT. In this model, E_J and E_C denote the macroscopic Josephson and Coulomb energies, which are averages over the sample for a distribution of these energies at the microscopic level (between individual grains). By construction, this model assumes a bosonic scenario for the SIT, i.e., pockets of superconductivity persist even on the insulating side of the transition (see Chapter 2 for an explanation of the bosonic scenario). As seen above, such an assumption is borne out by experimental data.

We later use this model to describe the phenomenon of charge-vortex duality in this system. In view of that, we describe what happens if magnetic flux is penetrating the sample. In the superconducting regime, the vortices are localized in the interstitials between the superconducting grains, whereas the Cooper pairs are free to move between the grains. However, in the insulating regime, the Cooper pairs are localized on the individual islands and the vortices are delocalized. This is the basis for charge-vortex duality in this system as described later in the chapter.

In the next section I discuss the data showing the coexistence of superconductivity and ferromagnetism in the system.

4.2. Coexistence of superconductivity and ferromagnetism

Superconductivity and ferromagnetism are rarely found to coexist naturally in any material system. This is primarily due to the pair breaking effects of the ferromagnetic exchange field on the singlet Cooper pairs in a conventional $s-$wave superconductor. There are very few examples of materials that have been reported to show these two co-operative phenomena existing in the same material [**151**–**154**]. The LAO/STO system joins these few materials in which a ferromagnetic state co-exists with the superconducting state. Evidence for the coexistence has come from multiple kinds of experiments performed by various groups. These include imaging of the magnetic response of both the superconducting and ferromagnetic orders by scanning SQUID microscopy [**11**, **81**], performing torque magnetometry of the ferromagnet while the sample is superconducting [**12**], and measuring the magnetoresistance (MR) of the sample in the superconducting state and observing ferromagnetic hysteresis [**10**, **79**, **80**]. Our paper on the results of our MR measurements, Ref. 10, was the first to report the coexistence of these two phenomena in this system. In this thesis I present the results of our measurements of the MR of the sample which show this coexistence. I also present data where we map out the $T-H$ phase diagram of the superconducting state of the sample.

Before showing the data, however, I present our model of the system which can help explain the MR data.

4.2.1. Model of the interaction between superconducting and ferromagnetic orders

We build our model of the system anticipating the MR data presented later. We expect the magnetization of the ferromagnet to lie in the plane of the sample since it minimizes the shape anisotropy energy, and also since there is experimental evidence for it [**11**, **81**]. A schematic of the sample depicting the state of the ferromagnet in the presence of an applied external field, say $H_{\parallel}$, is shown in the left panel of Fig. 4.12. In the right panel is shown a schematic of the corresponding state of the superconductor based on the $E_J - E_C$ model described above. Obviously in the real sample, the superconducting system lies below the ferromagnet (or above; the position does not really affect the physics), they are shown separately for clarity in the figure. We reasonably assume, based on the co-existence models discussed in Chapter 2, that the effect of the ferromagnetism on the superconductivity is passive, i.e., the field due to the ferromagnet acts as an external field on the superconductor.

To illustrate the effect of magnetization dynamics in the ferromagnet on the superconductor, we ramp the magnetic field from negative to positive values and see its effect on our system in Fig. 4.12. At a large external negative field (top schematic), all the moments of the ferromagnet are aligned with the field and since there is no mobile flux in the

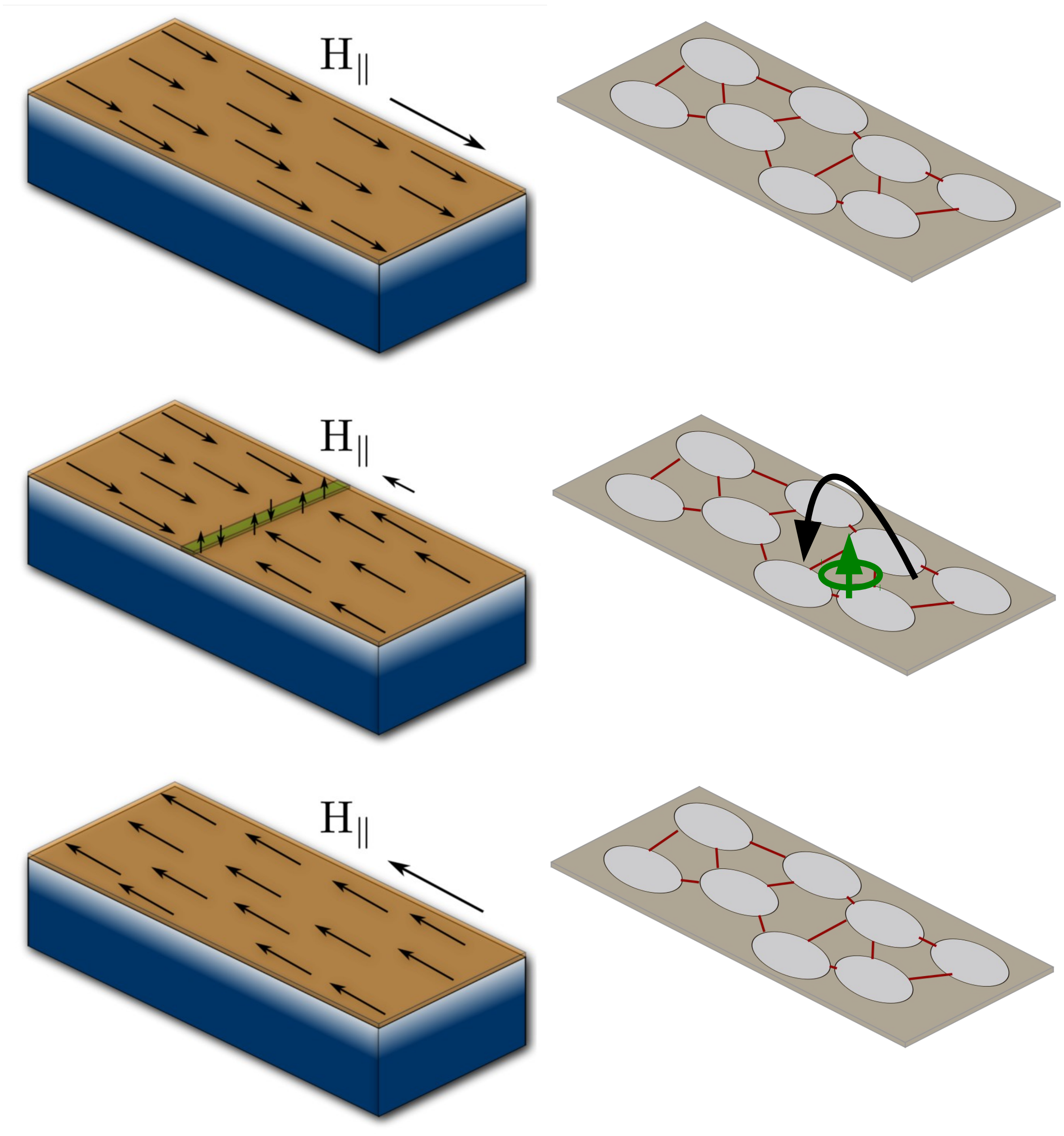

Figure 4.12. Schematic of the system at different parallel field values. The ferromagnet is at the top, the superconductor is shown as a gradient extending into the STO. The corresponding state of the superconductor is shown on the right for clarity. In this simplified picture, magnetization reversal occurs by means of domain wall propagation in the ferromagnet. The perpendicular component of the field due to the domain wall induces vortices in the superconductor.

superconductor, it is in a low resistance state (recall that voltage is generated in a superconductor by the Josephson relation, $V \sim d\phi/dt$). While ramping the field to a positive value, once zero field is crossed, the coercive field of the ferromagnet is reached (middle schematic). At that field, in a simplified picture, one thinks of a domain wall nucleating and propagating through the magnet. If the domain wall is a Bloch wall [**155**, **156**], it has a perpendicular component of field, which induces vortices in the superconductor. (In fact even a Néel wall can induce vortices in the inhomogeneous superconductor discussed above, if one considers the ferromagnetic layer embedded within the superconducting layer. The actual magnetization dynamics maybe even more complex with multiple walls of both kinds; all that is required for this model is the existence of a component of the field, which induces vortices in the superconductor.) These vortices are dragged along by the domain wall, and cause a resistance peak in the superconductor as the vortices cross the Josephson links (the vortex is depicted as the green arrow in the ring, the Josephson link is the red line between the superconducting grains). Once the domain wall has passed through there is no field to sustain the vortices and the system relaxes back to its low resistance state at high positive fields (bottom schematic). A similar situation also exists for the perpendicular field case. However, for perpendicular fields, due to the orbital pair-breaking effects of the external field, the resistance peaks are superimposed on a large background.

Note that in our model, the magnetization dynamics of the ferromagnet are induced and sustained by the external field sweep. In other words, when a domain wall is formed in the system, it does not travel though the system, unless being dragged along by the external field as explained above. Also, if the external field ramping is stopped mid-sweep at the coercive field where the resistive peak occurs, then there is no domain wall motion and consequently no vortex motion in the superconductor, resulting in a reduction of the resistive peak height. The reason for such behaviour of the domain wall is that there could be domain wall pinning sites in the sample due to the inhomogeneity and the associated disorder, which prevent the free motion of a domain wall. Evidence for this type of quasistatic behaviour of the magnetization dynamics is seen in the field sweep rate dependence of the MR which is discussed in a later section in the chapter. For now, we look at the MR data in the superconducting state with our model of the system in mind.

4.2.2. Hysteretic MR in the superconducting state

The coexistence of ferromagnetic order with superconductivity in the sample manifests itself through one of the classic signatures of magnetic behaviour: hysteresis. This is shown in Fig. 4.13. The top panel of the figure shows the MR of the sample in parallel magnetic field, $H_{\parallel}$, while the bottom panel shows it in a perpendicular magnetic field, $H_{\perp}$, at a gate voltage of V_g = 80 V, when the sample is deep in the superconducting state. The MR is hysteretic, suggesting the existence of ferromagnetism, with large peaks occurring in the MR at $H_{\parallel} \sim \pm$ 12 mT and $H_{\perp} \sim \pm$ 15 mT. (In the perpendicular field MR, there is also the existence of a secondary peak at $H_{\perp} \sim \pm$ 50 mT, which can be attributed to further magnetization dynamics in the ferromagnet.) As anticipated by our model of the system, we see peaks in the MR as the field is swept for both $H_{\parallel}$ and $H_{\perp}$. The background MR for $H_{\parallel}$ is small in the field range shown, while the background MR

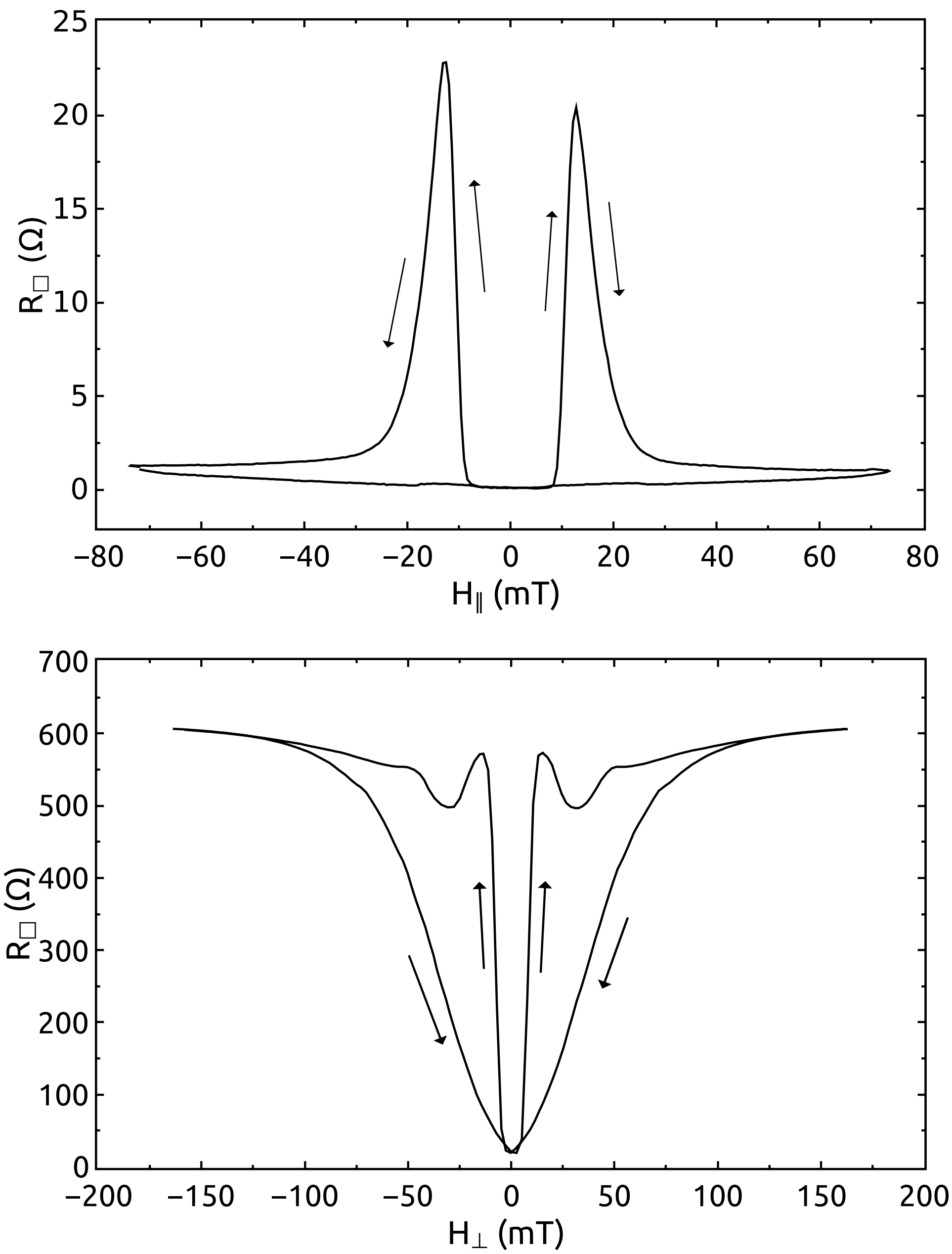

Figure 4.13. **Top:** Parallel field MR in the superconducting regime at $V_g =$ 80 V. Arrows indicate the direction of field sweep. **Bottom:** Perpendicular field MR for $V_g = 80$ V. $T = 50$ mK.

for $H_\perp$ is quite large as expected. From the direction of the arrows in the figure, it is seen that the peaks occur as the field crosses zero as it is swept from one extreme to the other. Consequently, we identify the field values at which the peaks occur with the coercive fields of the ferromagnet for the respective field directions. We see similar MR curves for all the gate voltages at which the sample is superconducting.

Note that such a hysteretic behaviour of the MR cannot be explained by vortex pinning in the superconductor, which also gives rise to hysteresis in type-II superconductors [**157**]. This is because the field scales of the hysteretic features (the peaks in the MR) are similar for both $H_\parallel$ and $H_\perp$. Since this is a 2D superconductor, conventional vortices are not generated by a field applied parallel to the film and cannot cause the peaks seen in our MR. Additionally, if vortex dynamics caused by the external field (not the intrinsic field from the ferromagnet as discussed above) played a part, one would not expect to see hysteretic MR in the insulating regime when the system is tuned through the gate voltage tuned SIT. In contrast, we do see robust hysteresis even in the insulting regime ($V_g < -30$ V). A detailed discussion of the evolution of the MR features as the system is tuned through the SIT gives rise to a manifestation of charge-vortex duality and is presented in the next section. For now, we focus our attention on the MR in the superconducting regime. From the discussion above we conclude that the observed behaviour of the MR has to be due to the presence of ferromagnetic order in the system. This behaviour can be understood based on the effect of magnetization dynamics in the ferromagnet on the superconductor as explained above.

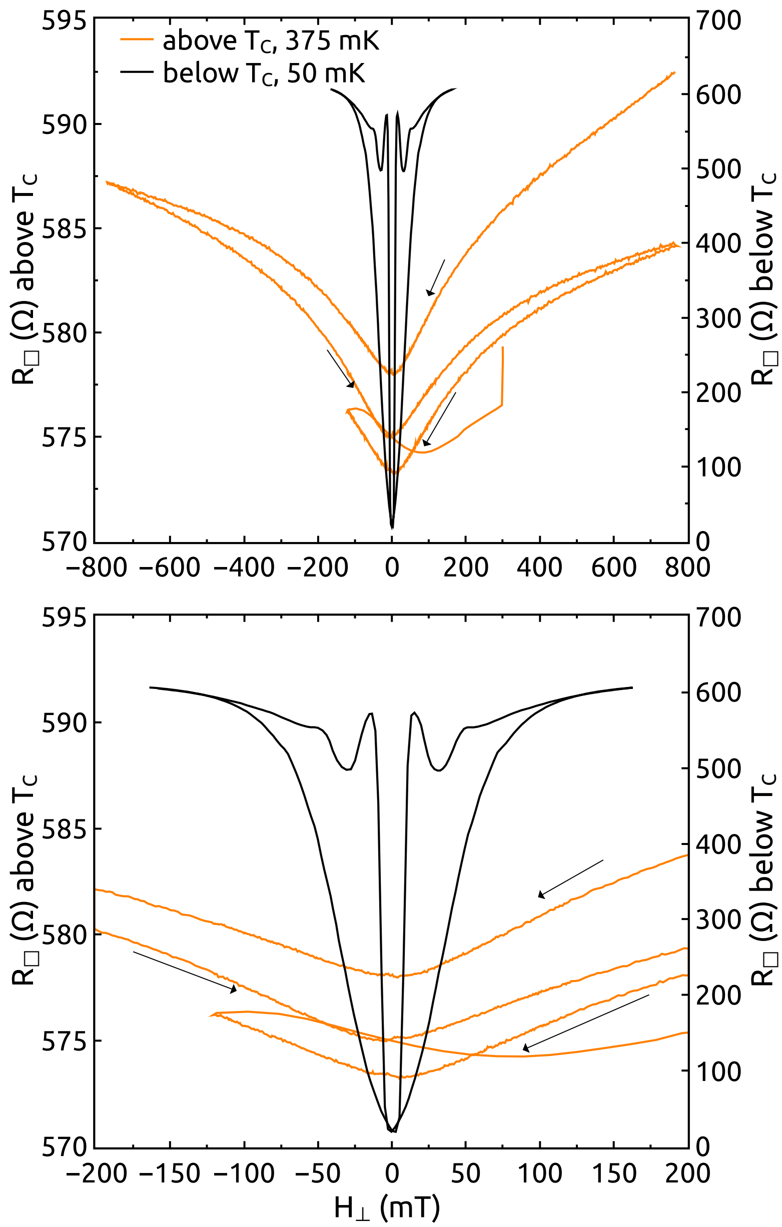

Figure 4.14. **Top:** Perpendicular field MR in the superconducting regime at $V_g = 80$ V at $T = 50$ mK and $T = 375$ mK. Arrows indicate the direction of field sweep. The MR at the higher temperature drifts as the field is swept. As explained in the text, we do not fully understand why the MR drifts, although charge trapping in STO may explain the observed drift. **Bottom:** Zoomed in region near $H_\perp = 0$ mT.

An interesting feature of the MR in the superconducting regime is the appearance of a drift in the MR at temperatures above T_C. This is shown in a representative MR curve in the top panel of Fig. 4.14 for $V_g = 80$ V at two different temperatures, $T = 50$ mK $< T_C$ and $T = 375$ mK $> T_C$ (T_C for $V_g = 80$ V is 139 mK). The bottom panel shows the zoomed in region near $H_\perp = 0$ mT. As seen in the figure, not only does one not see any hysteresis in the high temperature MR curve, but MR drifts as the field is swept. Such a large drift in the MR is not observed in the insulating regime, where one even observes hysteresis at $T = 375$ mK. This is shown in Fig. 4.15. We do not fully understand why the drift appears only for gate voltages at which the sample becomes superconducting. It should be noted that, while in the sample presented here, the insulating state MR at high temperature does not show a drift, for other similar samples we do observe a drift in the MR at high temperatures even when the sample is in the insulating regime. A possible explanation for the drift is the charge trapping mechanism discussed above to explain the hysteresis in the gate voltage dependent properties. Such charges are trapped by the defect/impurity states which usually occur in the gap and are metastable with their decay rates being dependent on temperature. The lower the temperature, the longer the decay times. Such charge states can decay over time and give rise to the observed drift.

4.2.3. $T - H$ phase diagram

4.2.3.1. Perpendicular field phase diagram. Further evidence for the coexistence of superconductivity and ferromagnetism is obtained by examining the phase boundary between the normal and superconducting state as a function of magnetic field H. As

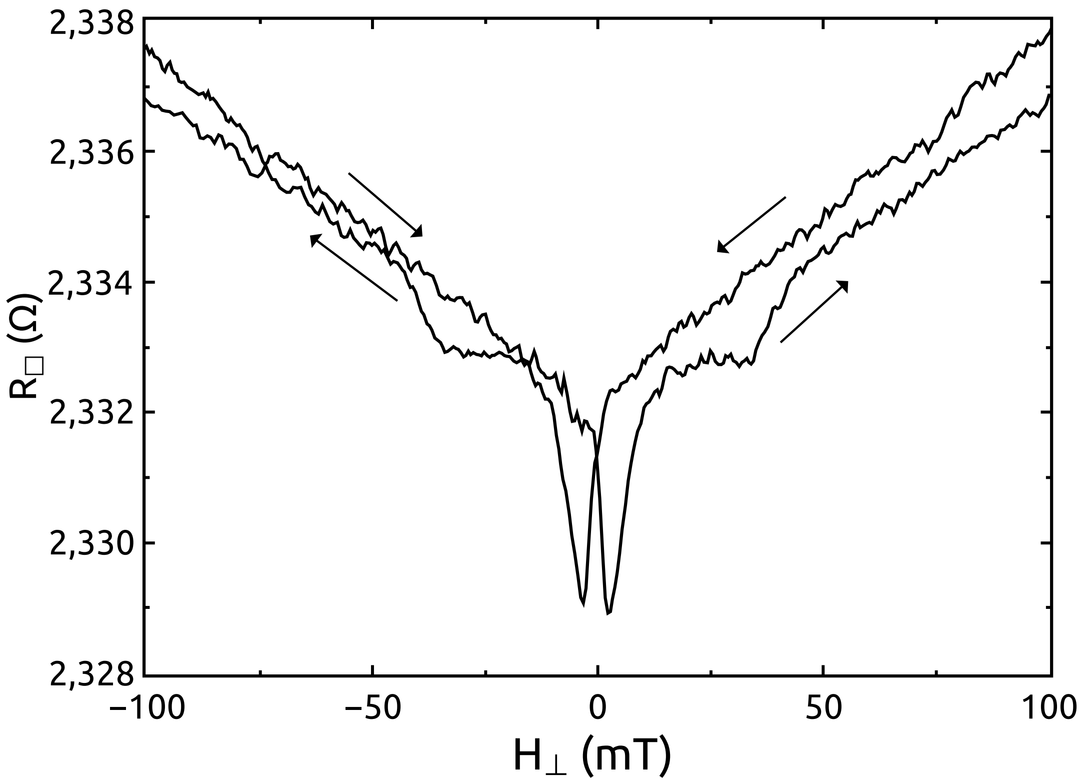

Figure 4.15. Perpendicular field MR in the insulating regime at V_g = -100 V at T = 375 mK. Arrows indicate the direction of field sweep. Unlike in the superconducting state, no large drift is seen in the MR.

explained in Chapter 3, we map out this phase boundary by controlling the temperature of the sample using a PID control loop (see Fig. 3.11 and its explanation for the technique used). This $T - H_{\perp}$ phase boundary is shown in Fig. 4.16 for three different resistance bias points along the superconducting transition at $V_g = 80$ V (top panel), for a magnetic field applied perpendicular to the plane of the sample. Like in the MR data above, the phase boundary as measured this way is also hysteretic, with the field scale at which the prominent hysteretic features occur, the dips in T_C, being $\simeq \pm$ 7 mT, less than the field scale for the peaks in the MR ($\pm$ 15 mT for $H_{\perp}$). This mismatch in the field scales is due to different field sweep rates for the MR data and for the $T-H$ data. The rate dependence of the hysteretic features is discussed later in the chapter.

To understand the observed hysteretic structure of T_C vs. $H_{\perp}$, we focus our attention on the curve corresponding to the bias point $R_{\square} = 208\ \Omega$, close to the midpoint of the superconducting transition. The mismatch in field scales notwithstanding, it is evident that the magnetization dynamics in the ferromagnet which causes the MR peaks, also causes the dips in T_C in Fig. 4.16, as explained below. This should not be surprising, since one is still monitoring the resistance of the superconductor in order to map out the $T-H$ phase diagram. From the direction of the arrows in Fig. 4.16, it is seen that the dips in T_C occur once the field crosses zero as the field is ramped. As discussed in the model above, at this field an additional field from the domain wall of the ferromagnet acts on the superconductor, reducing its T_C, resulting in the dips observed.

The curves obtained at the two other resistance bias points are similar, except that the overall curvature is negative when the sample is biased at the top of the transition, and positive when it is biased at the foot of the transition. The curvature of the curves could be due to the differing ferromagnet induced vortex dynamics in the superconductor at the top and the foot of the transition. An alternative explanation is the possibility of multiband superconductivity giving rise to the observed curvature of the $T_C - H$ curve [**158**, **159**]. However, more controlled experiments with multiple samples are needed in order to confirm multiband superconductivity in this system. The middle curve is the most linear as expected for a 2D superconductor in perpendicular magnetic field [**39**].

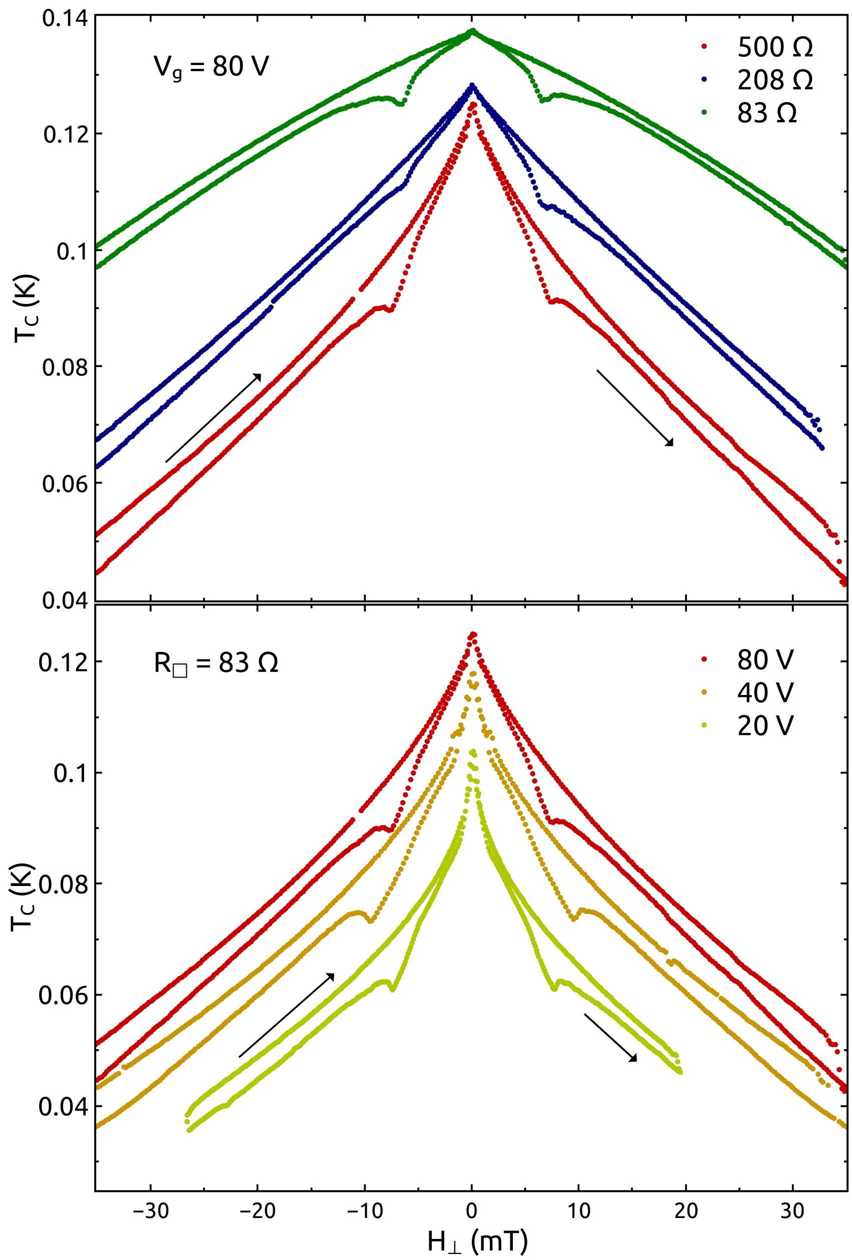

Figure 4.16. **Top:** Phase diagram, T_C vs. $H_\perp$, for $V_g = 80$ V. The three curves represent different resistance bias points along the superconducting transition, with the normal state resistance per square being 704 Ω. The arrows mark the direction of the magnetic field ramp. **Bottom:** Phase diagrams at a bias point of $R_\square = 83$ Ω, at the foot of the resistive transition, at three different gate voltages. Data for $V_g = 40$ V are shifted by 10 mK and data for $V_g = 80$ V by 20 mK for clarity.

One can extract the upper critical field, H_{C2}, from a fit to the curve at higher fields and calculate the Ginzburg-Landau coherence length,

$$\xi_{GL}^2 = \frac{\Phi_0}{2\pi H_{C2}}$$

where $\Phi_0 = h/2e$ is the superconducting flux quantum. For $V_g = 80$ V one obtains an upper critical field value of $H_{C2} \simeq 77$ mT, giving a coherence length of $\xi \approx 65$ nm, similar to that reported by other groups [**5, 33**]. We obtain a similar coherence length with the $T - H_\perp$ phase boundary mapped out in a more conventional manner, i.e., by measuring the T_C from R vs. T curves obtained at discrete magnetic fields. These data are shown in Fig. 4.17. The inset of the figure shows the $T - H_\perp$ phase boundary mapped out by the measurement of T_C at discrete magnetic fields. From the linear fit shown in the figure, one obtains, $H_{C2} \simeq 82$ mT and the corresponding coherence length of $\xi_{GL} \approx 63$ nm. Finally, similar hysteretic $T - H_\perp$ phase boundaries are observed for other gate voltages at which the sample goes superconducting, as demonstrated in the bottom panel of Fig. 4.16.

4.2.3.2. Parallel field phase diagram. From the continuous mapping of T_C vs. $H_\perp$ one can estimate the superconducting coherence length, ξ_{GL}, as discussed above. By making a similar PID controlled measurement to map out the $T - H_\parallel$ phase boundary, one can calculate the thickness of the superconducting layer. The result of this measurement is shown in Fig. 4.18. As expected for a 2D superconductor [**39**], the dependence of T_C on a parallel applied field is quadratic except at low fields where hysteresis due to the ferromagnet suppresses T_C. The field values at which the prominent hysteretic features, the dips in T_C, are observed coincide with the field values for the corresponding features,

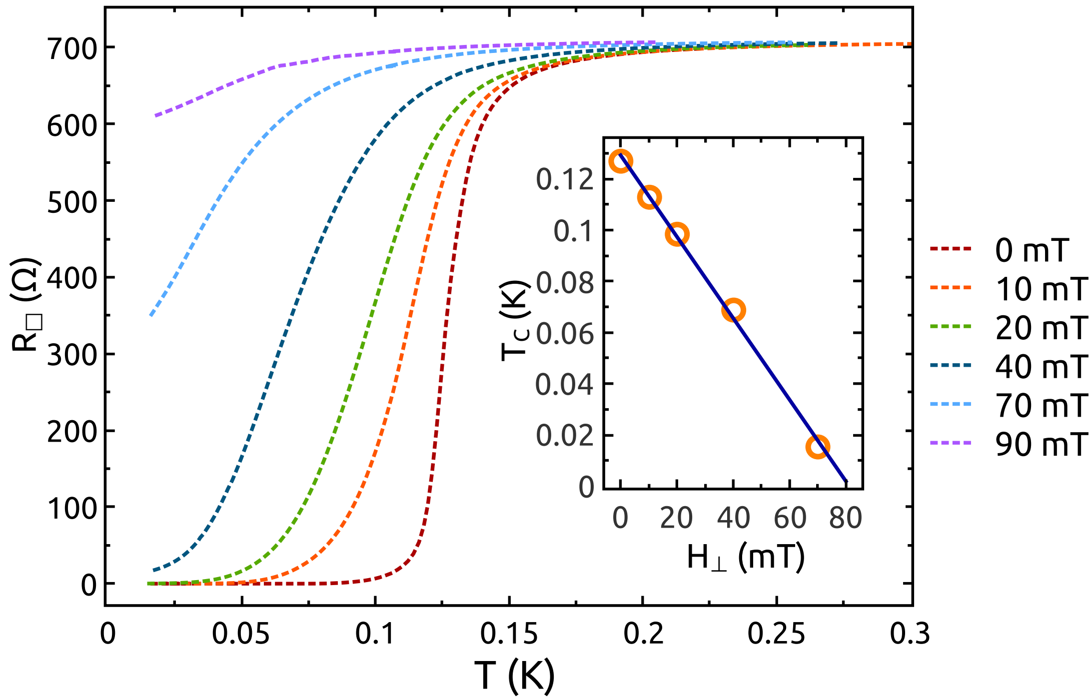

Figure 4.17. $R_\square$ vs. T at $V_g = 80$ V for different magnetic fields. The legend shows the different magnetic fields applied. The inset shows the T_C extracted from the $R_\square$ vs. T at the different magnetic fields. A linear fit (blue) to the data gives $H_{C2} \simeq 82$ mT, which yields a coherence length of $\xi_{GL} \approx 63$ nm.

peaks, in the MR curve ($H_\parallel = \pm$ 12 mT, see Fig. 4.13). The system was biased near the mid-point of the resistive transition ($R_\square = 288$ Ω @ $V_g = 80$ V). From a fit to the curve in Fig. 4.18 at high fields we extracted the parallel critical field, $H_{C\parallel} \sim 1.2$ T. For a thin film superconductor, $H_{C\parallel}$ and the film thickness are related by the formula [**39**]

$$H_{C\parallel} = \frac{\sqrt{3}\Phi_0}{\pi d \xi_{GL}}$$

where d is the thickness of the superconducting film. From a knowledge of ξ_{GL} and $H_{c\parallel}$, we determined the thickness of the superconducting film to be $d = 13.6$ nm, which is less than ξ_{GL}, confirming that the superconductor is 2D.

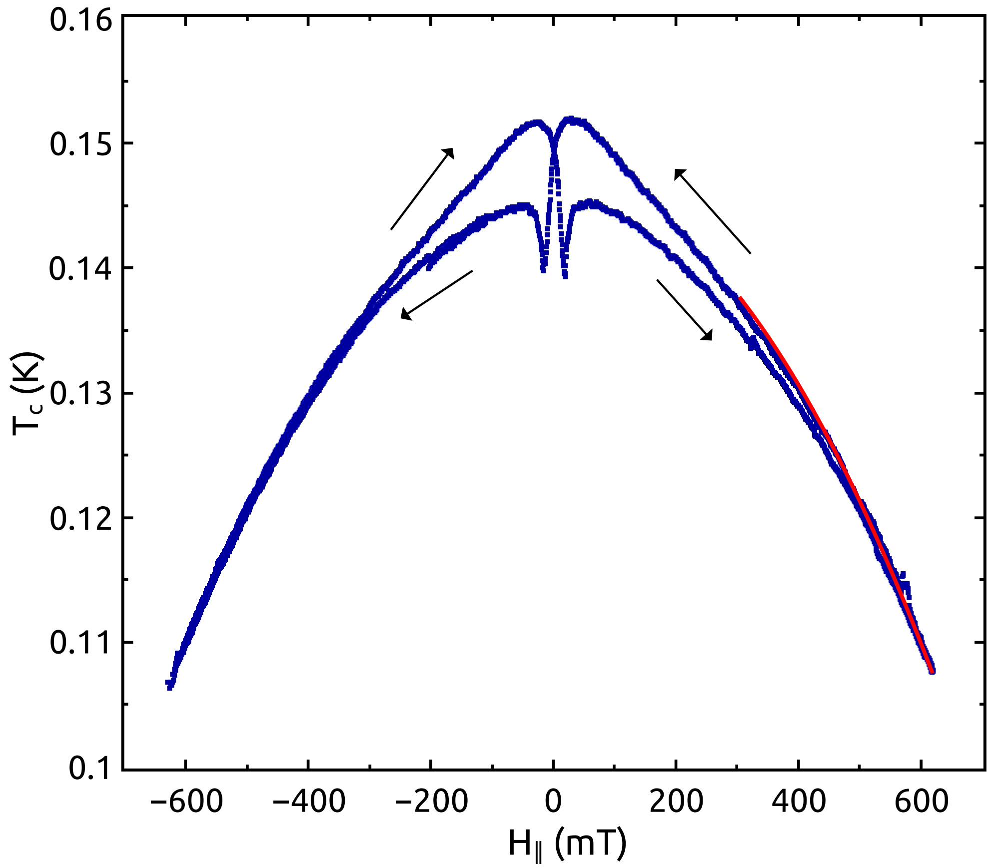

Figure 4.18. T_C vs $H_\parallel$ for V_g = 80 V. A parabolic fit (red curve) at high fields gives $H_{C\parallel} \sim 1.2$ T. The thickness of the superconducting layer estimated from this value is $d = 13.6$ nm.

4.3. Charge-vortex duality

In this section I discuss the observation of charge vortex duality in the MR data. As described in Chapter 2, duality transformations relate the two different quantum ground states in this system, superconductor and insulator, which can be accessed by tuning V_g as shown above. For a 2D SIT system the role of charge and magnetic flux interchanges between the two states under a duality transformation. Experimentally this gives rise to an observable interchange of current and voltage, or resistance and conductance as shown in the theory chapter. In the LAO/STO system, in the (001) direction, due to the weakly insulating state described above, the observation of duality in the $I-V$ characteristics of the sort shown in Chapter 2 (Fig. 2.17) becomes difficult. However, due to the almost serendipitous coexistence of superconductivity and ferromagnetism in this system, a duality of resistance and conductance is observed in the hysteretic MR features in the superconducting and the insulating regimes. To show that duality, I will first present some salient characteristics of the MR in both the superconducting and the insulating regimes. I will then describe how these can be understood within the model of our system, developed above. Finally, I will show a manifestation of duality in the MR features and present a quantitative analysis of the MR data based on phenomenological arguments.

4.3.1. Rate dependence of the MR features

4.3.1.1. Superconducting state. We begin with a discussion of a very peculiar characteristic of the MR features as a function of the external field sweep rate. I will first present data for the superconducting state and then for the insulating state. As an example of the superconducting state we take the case of $V_g = 80$ V. Figure 4.19a shows the MR in parallel field, $H_{\parallel}$, while Fig. 4.19c shows it for the perpendicular field, $H_{\perp}$ at a temperature, $T = 50$ mK, for different sweep rates of the external field. The data for both $H_{\parallel}$ and $H_{\perp}$ is shown as the field is swept from negative to positive values for clarity. The inset to Fig. 4.19a, which is the same data as that presented in Fig. 4.13, shows the full

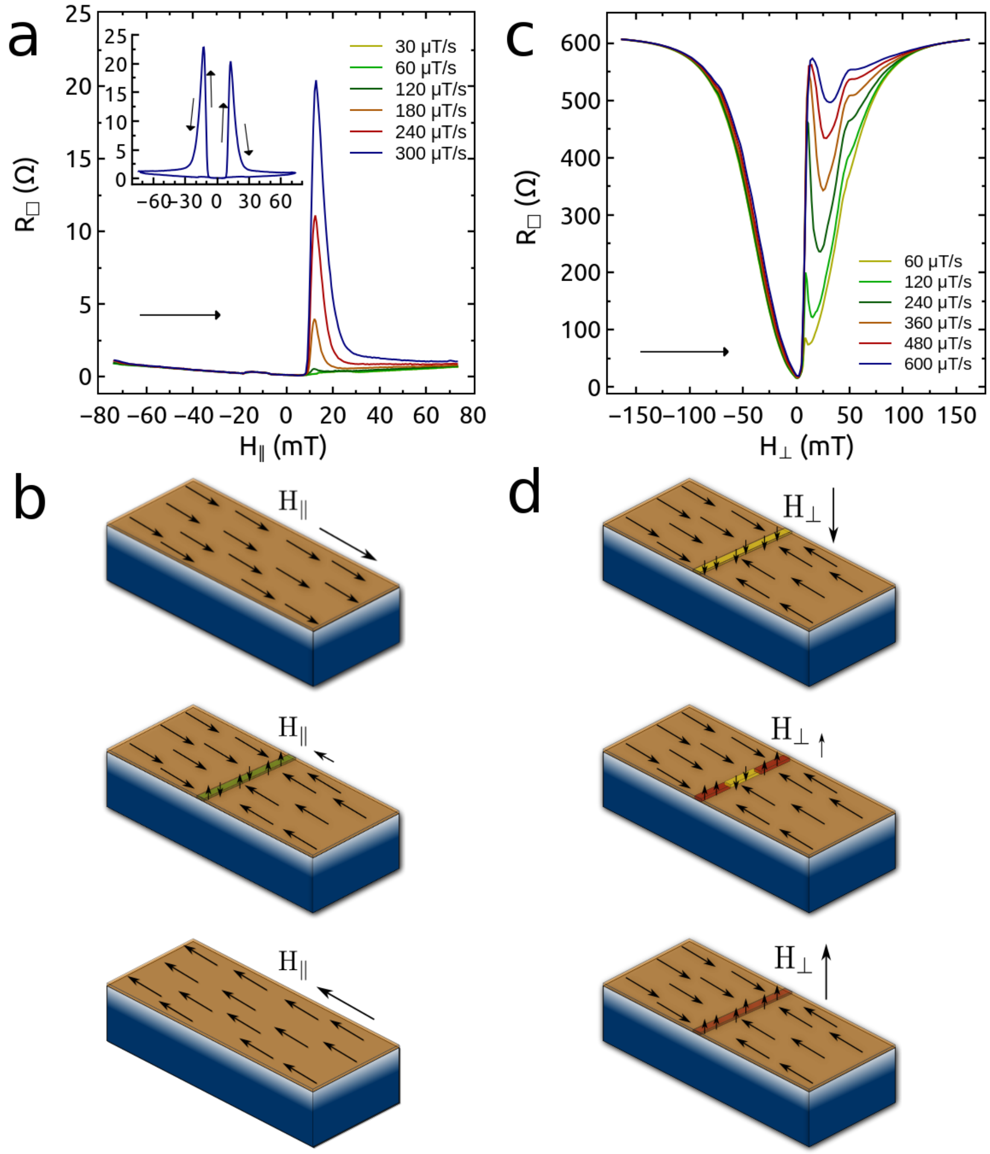

Figure 4.19. **a)** Parallel field MR as a function of different rates at $V_g = 80$ V. Data for only one field sweep direction is shown for clarity. Arrow indicates the direction of field sweep. The inset shows the MR for forward and backward field sweep directions at a sweep rate of 300 μT/s. **b)** Schematic of the system at different parallel field values. **c)** Perpendicular field MR for different field sweep rates at $V_g = 80$ V. **d)** Schematic of the magnetization state of the system at different perpendicular fields. Due to the shape anisotropy of the system, the majority of the moments lie in plane, but the external magnetic field orients the direction of the perpendicular component of the magnetization of the domain wall. $T = 50$ mK.

hysteretic MR. As explained earlier, the peaks in MR in the superconducting state can be understood if one considers the effect of magnetization dynamics in the ferromagnet on the superconductor (see §4.2.1).

The interesting thing to note about the data presented in Fig. 4.19 is the dependence of the MR features on the external field sweep rate. It is seen that the height of the MR peaks *increases* for faster field sweeps. Such behaviour is counterintuitive if one thinks about the usual effect of the sweep rate of an external parameter on a measured quantity like resistance. For example, in a measurement of dV/dI vs. I_{dc} for a superconductor, one normally observes sharp peaks in dV/dI at the critical current of the superconductor. However, if the current is swept too fast, the peaks get "washed out" due to averaging over a larger current interval. In contrast, what we see here is completely opposite. In fact, such a dependence of the MR features is understood if again one considers the effect of domain wall motion in the ferromagnet on the superconductor (shown schematically in Figs. 4.19b and d for $H_{\parallel}$ and $H_{\perp}$ respectively). As described in §4.2.1, in a simplified picture, one thinks of a domain wall that propagates through the ferromagnet at its coercive field, which induces vortices in the superconductor and whose motion causes the peaks in the MR. (Due to the 2D nature of the ferromagnet [**11**, **72**] ,the magnetization dynamics in the perpendicular field are more complex, giving rise to an additional peak in the MR, but the essential physics remains the same.) If we assume that the domain wall velocity, and hence the rate at which the vortices cross the Josephson links in the superconductor, is proportional to the external field sweep rate, then it is easy to explain the observed behaviour of the rate dependence of the MR features. The larger the sweep rate, the larger the rate at which vortices cross the Josephson links, giving rise to a larger peak height. This is because voltage appears across a superconductor via the general Josephson relation, $V \sim d\Phi/dt$, where Φ is a measure of the magnetic flux that crosses a link per unit time [**39**, **160**] (a more quantitative analysis of how the peaks are generated is presented below). Similar rate dependence of the peaks is observed at all the gate voltages at which the sample is superconducting.

The assumption of quasistatic dependence of the domain wall velocity on the external field sweep rate is supported by the following argument. We know that typical time scales for magnetization dynamics in a ferromagnet are extremely short, typically nanoseconds or smaller [**161**], so that the rates that we sweep the external magnetic field are essentially dc in comparison. Consequently, one can consider the magnetization reversal under the influence of the external magnetic field as essentially a quasistatic process, with the specific magnetization configuration a function only of the value of the external field, the field sweep direction, and any pinning sites in the sample. We have also confirmed this with micromagnetic simulations using a micromagnetic solver (OOMMF) [**162**], using magnetic parameters for both permalloy and the predicted values for the LAO/STO interface (Ref. 12), "samples" of various sizes, and the actual sweep rates used in the experiment. We found from the simulations that the rate of change of the magnetic field due to the ferromagnet that couples to the superconductor is determined entirely by the sweep rate of the external magnetic field.

4.3.1.2. Insulating state. Similar rate dependence of the MR features is seen on the insulating side of the gate tuned SIT. This is shown in Fig. 4.20 for a) $H_{\parallel}$ and b) $H_{\perp}$ for V_g = -100 V at T = 50 mK. Again, data for fields swept in only one direction are shown for clarity. In the insulating state the prominent MR features are *dips* in resistance from the background resistance at exactly the same field values at which peaks in MR occur in the superconducting regime. As with the peaks in the superconducting regime, the magnitude of the dips increases with increasing sweep rate. Note that in perpendicular field, one even observes two sets of dips (at $\pm$ 15 mT and $\pm$48 mT), mirroring the behavior seen in Fig. 4.19c. An interesting aspect of the dips in the insulating regime is their size. Unlike in the superconducting regime, where the size of the peaks are very different for $H_{\parallel}$ and $H_{\perp}$, the size of the dips in the insulating regime are very similar for the two field orientations. This is because there are no corresponding orbital effects in the insulating regime for $H_{\perp}$. The peaks in MR in the superconducting regime were explained by the effect of domain wall motion in the ferromagnet on the superconductor. How are the dips in resistance in the insulating regime caused? It would be reasonable to expect that an analogous effect of the domain wall dynamics in the ferromagnet on the 2DEG in the insulating regime causes the observed dips.

We can get a physical picture of how the dips occur on the insulating side, if we consider the effect of domain wall motion on the insulating state within the $E_J - E_C$ model described above. In the insulating state, the motion of magnetic flux does not cause any increase or peak in resistance as the Cooper pairs are confined to individual islands by the charging energy E_C. However, due to Faraday's law of induction, we know that a

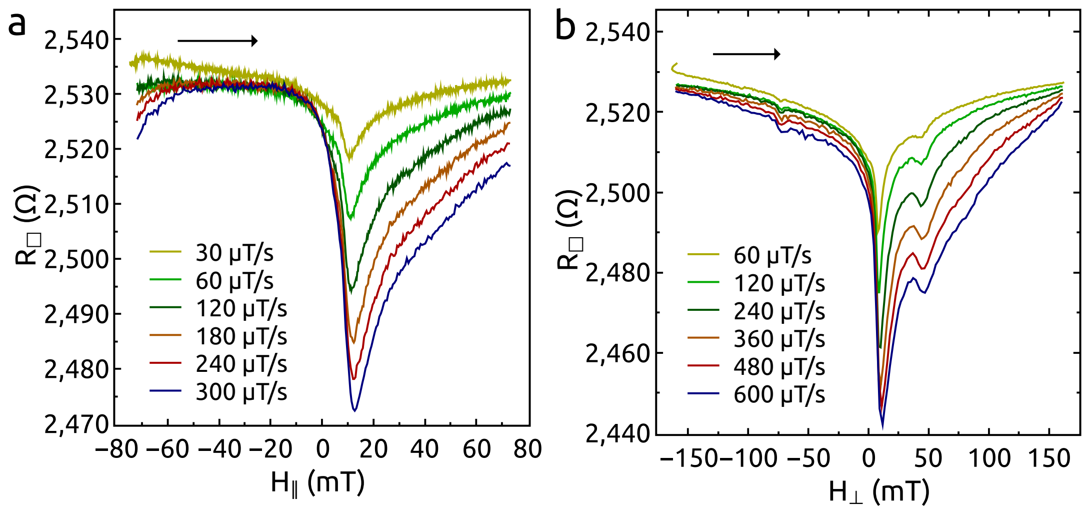

Figure 4.20. **a,** Parallel field MR for V_g = -100 V. Data for only one field sweep direction is shown for clarity. Arrow indicates the direction of field sweep. **b,** Perpendicular field MR for V_g = -100 V. T = 50 mK.

time rate of change of magnetic field gives rise to an electric field $\mathcal{E}_H = -\partial A/\partial t$, where A is the vector potential associated with the magnetic field. In our case the magnetic field is generated by the magnetization dynamics in the ferromagnet, just as in the superconducting regime. This electric field causes a potential difference to develop between two neighbouring islands separated by a distance a, $V = -\mathcal{E}_H a$. When the energy due to this potential difference exceeds the charging energy, the Cooper pairs can hop across the islands causing a decrease in resistance as observed. Again one expects the effect to be external field sweep rate dependent, since the speed of the domain wall is determined by the external field sweep rate. The larger the sweep rate, the larger the size of the dips, as observed. It should be noted that such behaviour of MR is only possible due to the weakly insulating nature of the insulating regime. If the SIT were into a strongly insulating regime, E_C would be very large and one would not observe the dips in MR.

I now discuss a novel observation of charge-vortex duality between the two ground states of the system, which is based on the change from peaks to dips in the MR as the system is tuned through the SIT.

4.3.2. SIT in the magnetoresistance: duality

As described above, in the charge-vortex duality model, current and voltage are switched in going across the SIT, so that conductance and resistance are also switched. Thus, where one observes peaks in resistance on the superconducting side, one should observe peaks in conductance (or dips in resistance) on the insulating side. This is exactly what is observed when one compares the MR in the superconducting and insulating regimes shown above. A further confirmation of this is seen in the evolution of peaks to dips as the system is tuned through the superconductor to insulator transition, as shown in Fig. 4.21. As V_g is changed from +80 V to -100 V, the peaks in the MR change to dips. For $H_{\parallel}$, this occurs at V_g between -25 to -30 V, which corresponds to the value at which one sees the SIT in the zero field temperature dependent resistance (see Fig. 4.5). For $H_{\perp}$, the gate voltage at which this transition occurs is lower because the applied perpendicular field also suppresses superconductivity due to orbital effects. Thus the same phenomenon, that of magnetization dynamics in the ferromagnet, which causes an increase in resistance on the superconducting side, causes an increase in conductance on the insulating side. This interchange of resistance and conductance between the two different ground states of the system demonstrates the duality of the two states. We note that the $R_{\square}$ value at which this transition occurs is approximately 2.1 kΩ, less than the universal resistance value of

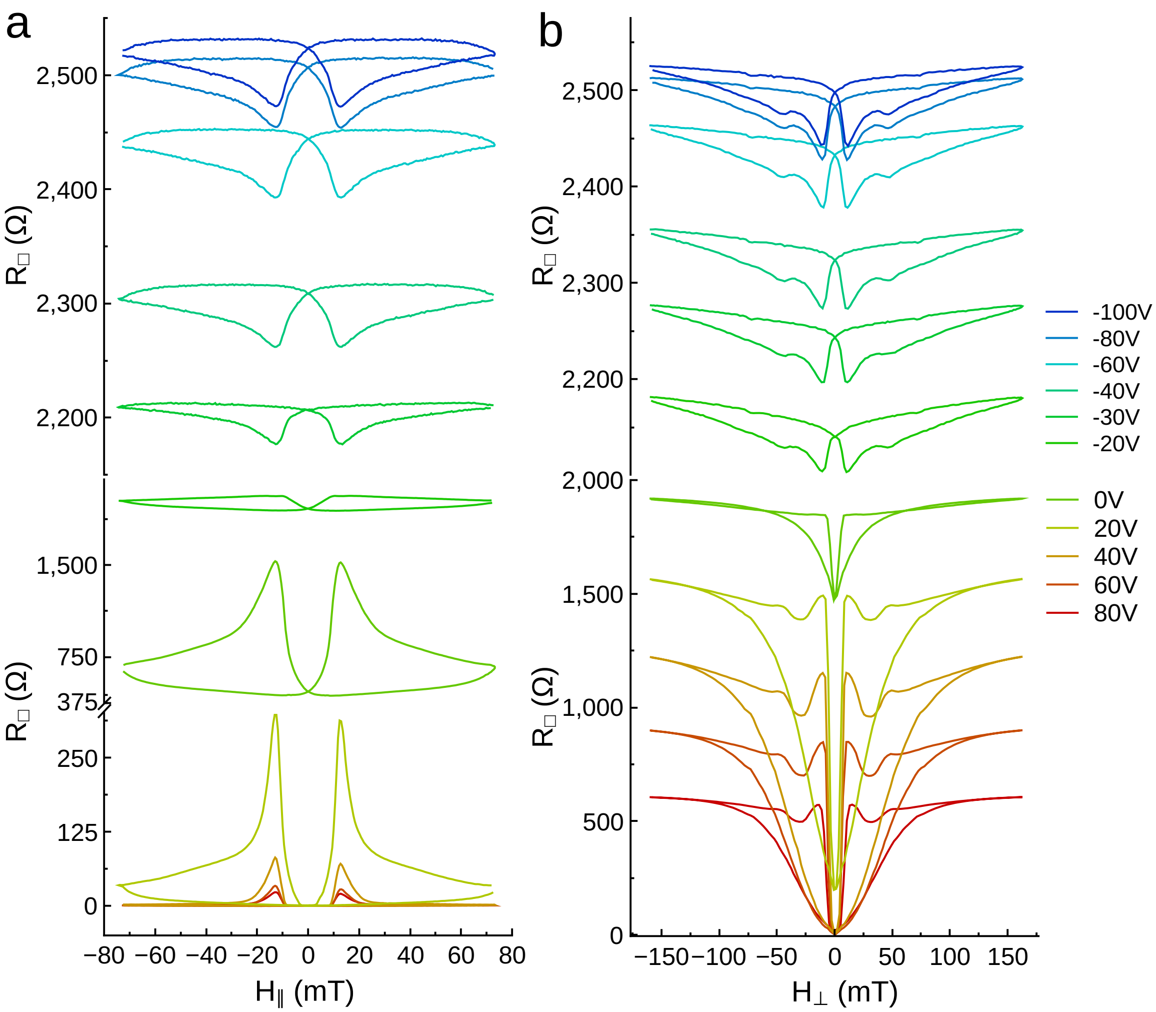

Figure 4.21. **a,** Parallel field MR for the fastest sweep rate (300 μT/s) as a function of gate voltage, tuning the system from the superconducting to the insulating regime. The top and bottom panels are for insulating and superconducting regimes respectively. Charge-vortex duality manifests itself as the conversion of the *peak* in the superconducting regime to a *dip* in the insulating regime. The peak and dip occur at the external field value of $H_{\parallel} \sim \pm$ 12 mT. (There is an axis break on the y-axis in the bottom panel.) The maximum change in the resistance occurs for $V_g = 0$ V, where the superconductivity is very weak. **b,** Similar behaviour in perpendicular field. Note that the fastest sweep rate in this case is 600 μT/s. Additional structure in the perpendicular field at $H_{\perp} \sim \pm$ 48 mT is due to the more complex magnetization dynamics in the perpendicular field. $T = 50$ mK.

$R_Q = h/4e^2 \sim 6.45$ kΩ expected for the SIT [**85**].

I now present a quantitative analysis of the MR data based on a phenomenological model that we have developed to explain the MR features.

4.3.3. Thermal activation model for the resistance peaks/dips

In order to explain the MR features we use the $E_J - E_C$ model of our system, which was described earlier. As before, we begin with the superconducting case.

4.3.3.1. Superconducting regime. On the superconducting side of the transition, $E_J >> E_C$, and the sample is in the zero resistance state provided there are no mobile vortices induced in it. Any stationary vortices present reside in the interstitials between the superconducting islands. Magnetization dynamics in the ferromagnet induce mobile vortices in the superconductor and give rise to a finite resistance peak in the MR as the vortices cross the Josephson links between the islands. In order to understand the mechanism of the generation of this resistance, we use the phase slip model due to Langer and Ambegaokar (LA) [**163**]. There are corrections to this model, for example by McCumber and Halperin [**164**], but the basic concepts developed by LA are all that are essential for our analysis.

To understand how the phase slip model of LA can be applied to our system, we consider two adjacent superconducting islands that are Josephson coupled to each other at two points, so that the interstitial region between them can enclose a vortex: the sample consists of a network of such interconnected islands. (More generally, one probably has multiple interconnected islands enclosing vortices, but this does not change the physical picture.) These two islands can be thought of as a dc superconducting quantum interference device (SQUID) [**39**], whose energy profile is given by

$$U(\phi) = -E_J \cos\phi \tag{4.2}$$

where ϕ is the phase difference across the SQUID and E_J is the Josephson energy. E_J is proportional to the critical current I_C of the SQUID. Such an oscillating energy profile of the SQUID has minima occurring at $\phi = 2n\pi, n = \pm1, \pm2, \pm3 \ldots$. For one vortex enclosed, the phase difference across the SQUID is $\pm2\pi$. At finite temperature, the system can be thermally activated over the energy barrier represented by E_J from one potential minimum to an adjacent minimum which differs by a value $\Delta\phi = \pm2\pi$. In our case this is achieved when a vortex jumps in or out of the interstitial. Each such phase slip event will give rise to a voltage pulse according to the Josephson relation

$$V = \frac{\hbar}{2e}\frac{d\phi}{dt} \tag{4.3}$$

where the phase change is $\pm2\pi$. In the absence of an external current, phase jumps in either direction are equally likely, hence the average voltage measured across the junction is zero, although such phase slip events may give rise to voltage noise.

In the presence of an external measuring current I, the SQUID's energy profile is modified to the "tilted washboard" potential [**39**]

$$U(\phi) = -E_J \cos\phi - \frac{\hbar}{2e} I\phi. \tag{4.4}$$

In this case, phase slip events corresponding to the system traveling "down" the washboard tilt are slightly more likely than those in the other direction, leading to a finite average voltage in the direction of current, and hence a finite resistance. However, the probability of such events is still quite small at low temperatures if $I << I_c$. LA's original paper focused on phase slips in a single weak link between two superconductors. They derived the rate at which phase slips occur in each direction

$$\eta_{\pm} = \Omega e^{-\Delta F^{\pm}/k_B T} \tag{4.5}$$

where Ω is the attempt frequency and depends on microscopic parameters as well as external parameters of the circuit and $\pm$ refers to the two directions. Here $\Delta F^{\pm}$ is the free energy barrier for phase jumps in the the two directions [**160**]

$$\Delta F^{\pm} \approx 2E_J \mp \frac{\pi\hbar I}{2e}. \tag{4.6}$$

In the LA model, the application of a voltage V drives the generation of phase slips, and in steady state, the average voltage due to the generation of phase slips is equal to the applied voltage, giving the relation

$$V = (2\pi\hbar/e)\Omega e^{-2E_J/k_B T} \sinh(\pi\hbar I/2ek_B T) \tag{4.7}$$

In the low current limit ($I \ll ek_B T/\hbar$) and one can expand the sinh function to obtain the corresponding resistance

$$R = V/I = (\pi\hbar^2/e^2 k_B T)\Omega e^{-2E_J/k_B T}. \tag{4.8}$$

As mentioned above, in our case, a phase slip is generated whenever a vortex crosses a weak link. The rate at which such vortex crossings occur is then proportional to the time dependence of the field generated by the magnetization of the ferromagnet, which in turn is proportional to the external magnetic field sweep rate $\dot{B} = dB/dT$. This means there is an additional factor in Eqn (4.8) proportional to $\dot{B}$. The change in resistance due to the motion of vortices for the entire sample is an average of terms such as Eqn (4.8) with a distribution of E_J's. Since each such term will have an additional factor of $\dot{B}$, the total resistance change in the sample will be proportional to $\dot{B}$. On the other hand, the measured value of the critical current I_C of the sample will be determined by a parallel combination of random paths through the weak links connecting the superconducting islands. Nevertheless, it is reasonable to assume that this measured critical current I_C is proportional to the mean Josephson energy E_J for the superconducting network. Thus, we can write the change in resistance due to the motion of vortices in the form

$$\Delta R = A\dot{B}e^{-\alpha I_c/k_B T} \tag{4.9}$$

where I_C is the measured critical current, and A and α are numerical constants at a fixed temperature. According to this equation, a plot of $\ln(\Delta R)$ vs. I_C should yield a straight line at a fixed temperature; where the I_C's are varied by changing V_g. Figure 4.22 shows this plot for ΔR values obtained for parallel field. As can be seen, the plot is indeed linear for the three highest field sweep rates. For lower values of sweep rates, we found that the plot deviates from the linear behaviour for V_g = 40, 60, and 80 V. Although we do not fully understand the reason for this, it could be due to the fact that at lower sweep rates, the energy in the domain wall velocity may not be enough to unpin the vortices from the interstitials between the superconducting islands. The slopes (equal to the exponential factor α/k_BT) of the linear fits in Fig 4.22 are 2.7×10^7, 2.22×10^7, and 1.97×10^7 A^{-1}, for the three sweep rates, 180, 240, and 300 μT/s respectively. The slopes (which should be equal for the three sweep rates) match to within about 20 %. It should be noted that for the perpendicular field the situation is complicated by the fact that there is also an orbital contribution to the peak height and the data does not lend itself to the simple analysis above.

4.3.3.2. Insulating regime. On the insulating side of the transition, $E_C > E_J$, and charge transport between islands is suppressed due to the charging energy E_C. If one considers thermal activation, the rate at which charge can be transferred is proportional to e^{-E_C/k_BT} [**165**], and as with the superconducting regime above, charge transfers in both directions are equally likely, so there is no net average current. In the presence of a finite voltage difference ΔV between two islands, the rate is modified to $e^{-(E_c \pm 2e\Delta V)/k_BT}$, and consequently favors charge transfer from the island at higher potential to the island at lower potential, resulting in a net average current between the islands. As described above, in our model, the potential ΔV results from the electric field that is generated by the moving magnetic field produced by the magnetization dynamics in the ferromagnet through Faraday's law. The time dependence of the changing magnetization, as we have pointed out above, is proportional to the sweep rate of the external magnetic field $\dot{B}$, and hence $\Delta V = \gamma\dot{B}$, where γ is a constant. Thus, the resistance of the dip should have a

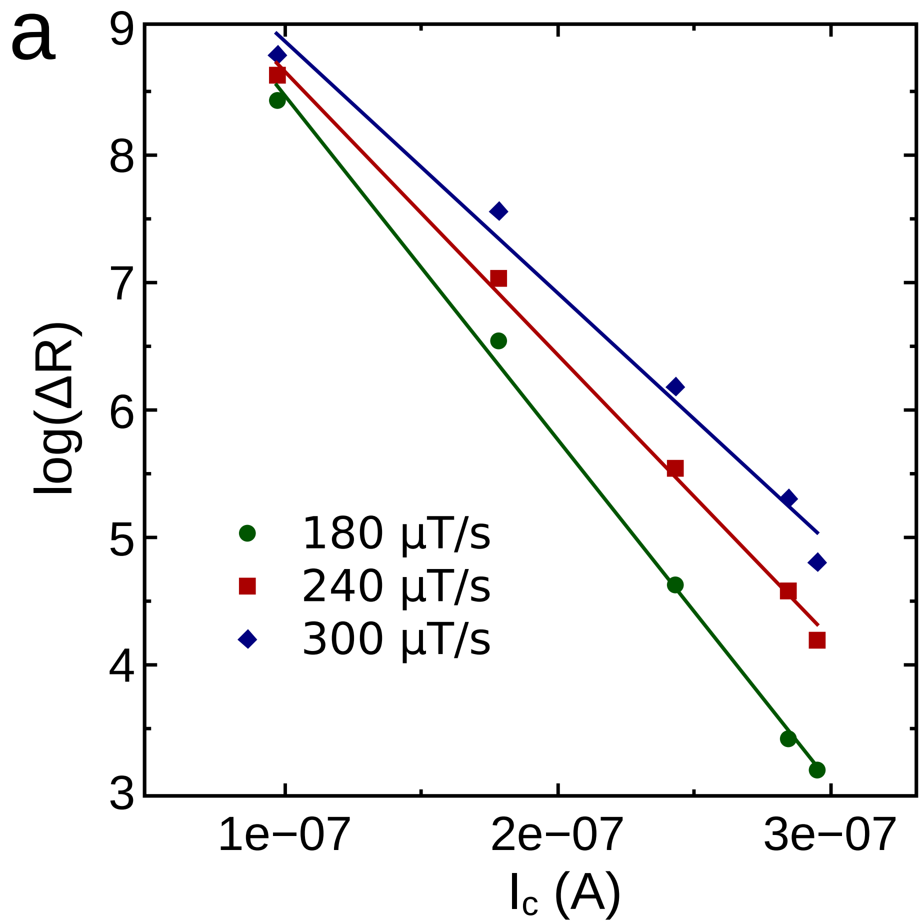

Figure 4.22. $\log(\Delta R)$ vs. I_C in the superconducting regime for the three fastest sweep rates in parallel external field. ΔR is defined as the difference in resistance between the forward and reverse magnetic field sweep traces at $H_{\parallel} \sim 12$ mT. The five gate voltages corresponding to the five I_C's are $V_g = 0$, 20, 40, 60, and 80 V from the smallest to the largest I_C. The three lines are the fits to the data at the three different sweep rates. Fitting parameters are given in the text. $T = 50$ mK.

dependence on the magnetic field sweep rate of the form

$$\Delta R = -A + Ce^{-\gamma \dot{B}/k_B T}. \tag{4.10}$$

where A and C are constants. We note that this is a characteristically different dependence than that which is predicted and found in the superconducting regime.

Figure 4.23 shows a plot of the resistance change at the dip as a function of the parallel field sweep rate for different gate voltages on the insulating side: the lines are fits to the exponential form, Eqn. 4.10. As can be seen, the fits are quite good. The fit parameters for $V_g = -30, -40, -60, -80$, and -100 V are, respectively: $A = 568.59$, 332.77, 371.9, 381.05, and 373.59 Ω; $C = 578.56$, 360.572, 379.10, 424.60, and 391.51 Ω; and $k_B T/\gamma = 25.11$, 5.22, 5.97, 5.79, and 5.89 μT/s. For V_g= -100, -80, -60 V, and -40 V the value of γ is almost the same. For V_g= -30 V, it is quite different. The time dependent magnetic field generates an electric field; the resulting voltage ΔV is not only proportional to the the electric field, but also to the spacing a between islands. Hence γ should also depend on a. As V_g is changed to bias the system closer to the transition from the insulating side, it is reasonable to expect that the effective spacing between islands decreases, resulting in a decrease in γ, as seen in the value of γ obtained from the fit.

I now discuss the magnetic field tuned SIT in this system.

4.4. Magnetic field tuned SIT

As seen above, a SIT in this system is induced under the effect of an electric field. It is found that the application of a perpendicular magnetic field, $H_\perp$ (we use H and $H_\perp$

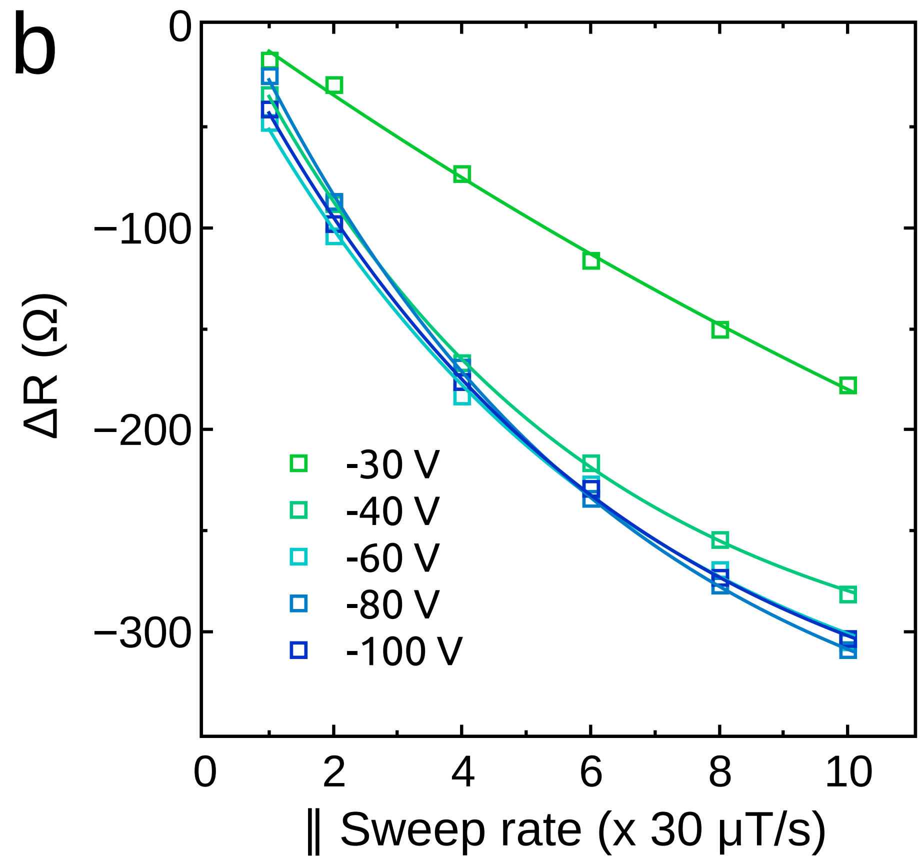

Figure 4.23. ΔR as a function of the parallel field sweep rate in the insulating regime. The data for each gate voltage, V_g = -30, -40, -60, -80, and -100 V are fitted to an exponentially decaying function. Fitting parameters are given in the text. $T = 50$ mK.

interchangeably in this section) also induces a SIT in this system which is also a quantum phase transition since it can occur at $T = 0$ K. In 2D superconductors the effect of magnetic field is to induce an insulating phase beyond a critical field H_C, which is different from the high temperature normal phase of the 2D system at $H = 0$. The nature of the insulating phase, and its transport behaviour, is found to be different in different systems [**86**, **89**, **92**, **106**, **136**, **166**–**168**]. As described in Chapter 2, there is still debate about the nature of the insulating phase: in the fermionic picture, the superconducting order parameter amplitude vanishes completely everywhere in the sample, while in the bosonic picture, the order parameter amplitude survives through the SIT, although increasing phase fluctuations between localized superconducting islands destroys long range phase coherence.

To observe the magnetic field tuned SIT we apply a perpendicular magnetic field to the sample and study its transport behaviour. Figure 4.24 shows the MR of the system at four temperatures below the critical temperature, T_C for the three gate voltages V_g = 60, 40, and 20 V. Since the maximum T_C observed in the R vs. T dependence is $V_g \sim 70$ V, we study the magnetic field tuned SIT for gate voltages below $V_g = 70$ V. In order to study the magnetic field tuned transition, we have chosen to eliminate the effect of hysteresis due to the ferromagnet on the 2DEG by applying a small parallel field, $H_{\|} = 100$ mT that aligns the moment of the ferromagnet in one direction. As seen in the figure, the MR is non-hysteretic with no peak features visible. Hence, we show data for one sweep direction of $H_{\perp}$ ($H_{\perp}$ swept from $0 \rightarrow 320$ mT). (The parallel field also results in a small (~ 3 mT) asymmetry about $H_{\perp} = 0$ mT due to the misalignment of the sample in the field.) As seen in Fig. 4.24, the system reaches a state of higher resistance with a weak temperature dependence, upon the application of the magnetic field. As in the case of the V_g tuned SIT in this system, the insulating phase of the magnetic field tuned SIT also seems to be a “weak” insulator, at least in the ranges of temperature and field measured. (See Fig. 3.12 for the results of a dV/dI vs. I_{dc} measurement showing a transition to the insulating state as an increasing magnetic field is applied at $V_g = 60$ V.)

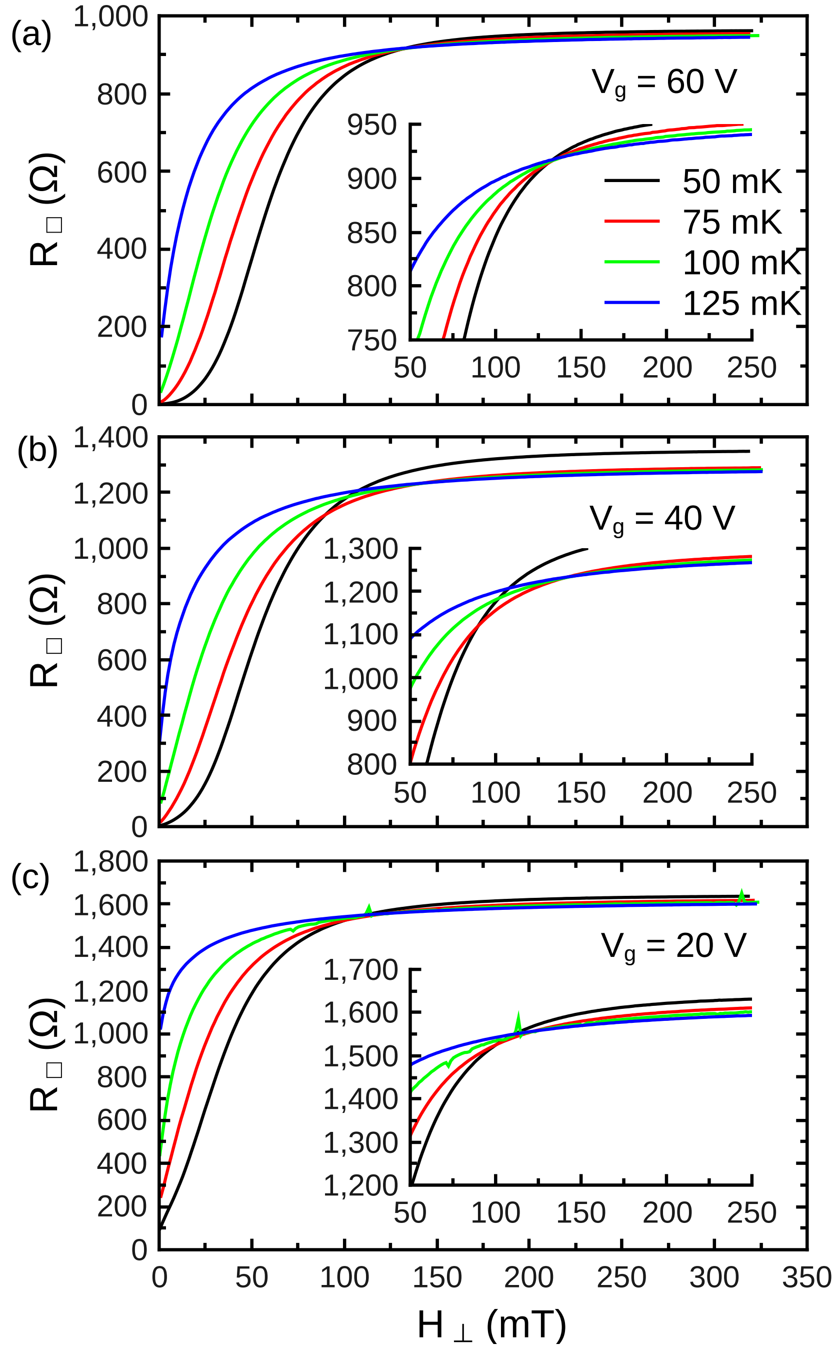

Figure 4.24. **(a)**, **(b)**, and **(c)** are the MR at four different temperatures for V_g = 60 V, 40 V, and 20 V respectively, in order of decreasing T_Cs. $T < T_C \ \forall \ V_g$'s. The insets show the zoomed in region of the MR where the different isotherms cross each other. The field at which the crossing occurs is close to the critical field H_C of the field induced SIT.

It is seen from Fig 4.24 that beyond a certain critical field (which is roughly the field at which the different MR isotherms cross; more on the determination of the critical field below) the MR increases slowly with the field for all the gate voltages, at all temperatures. Unlike other, more resistive systems in which the magnetic field tuned SIT is studied [**92**, **166**, **167**], we do not observe a large peak in the MR beyond the critical field, at least in the measured field range. In systems where such a peak is observed, its existence is thought to be due to the localization of Cooper pairs in the insulating state, with the size of the peak increasing with decreasing temperature. One way to think about the origin of the peak is that an increasing magnetic field causes a weakening of the Josephson links between neighbouring superconducting grains, which makes it difficult for Cooper pairs to tunnel between them, resulting in an increase in resistance. An observation of the MR peak is one of the signatures of the system being in the so called Bose insulator phase. Since we do not observe a peak, we need to perform a scaling analysis of our MR data in order to further characterize our system.

As described in Chapter 2, for systems that undergo a magnetic field tuned SIT, the resistance scales in the quantum critical region as,

$$R(H,T) = R_C f[|H - H_C|/T^{1/z\nu}]$$

where f is a homogeneous function of H and T, and R_C is a constant. Here H_C is the critical field at which the transition occurs, z is the dynamical critical exponent, and ν is the correlation length exponent. One of the critical factors determining the successful scaling of experimental data is the determination of the critical field H_C. One way to determine H_C is to see at what field the different MR isotherms cross (Fig. 4.24). However, this does not give an accurate measure of H_C (see for example the curves for $V_g = 20$ V), especially for low resistance samples like ours. From Fig. 3.12 it can be seen that the transition happens close to $H_\perp = 159$ mT for $V_g = 60$ V. However, the determination of H_C by changing the field discretely is a very time consuming process, particularly for a system with such a large phase space.

In order to ascertain the value of H_C for the different V_g's, we have measured the third derivative of voltage with current, d^3V/dI^3, as a function of the field (see Chapter 3 for an explanation of the d^3V/dI^3 measurement technique). We recall from Chapter 3, that in order to measure H_C using this technique, one simply monitors the sign of the third derivative as the external field is swept: the field at which the sign of d^3V/dI^3 goes from positive to negative, is the critical field of the transition. The advantage of such a measurement is that it is much faster to observe the field tuned transition compared to measuring the R vs. T or I-V characteristics at discrete magnetic fields.

Figure 4.25a shows d^3V/dI^3 vs $H_\perp$ for the three V_g's. Some non-monotonic features are seen at low fields, which arise due to the curvature in the shape of the MR (Fig. 4.24). As expected, the system transitions into the insulating state for all V_g's, as seen by the change in sign of the curves, and the critical fields are different for the different gate voltages. For $V_g = 60$ V, $H_C = 159$ mT, indicated by the arrow. This value of H_C is confirmed by the dV/dI vs. I_{dc} measurements shown in Fig. 3.12, where precisely at $H =$

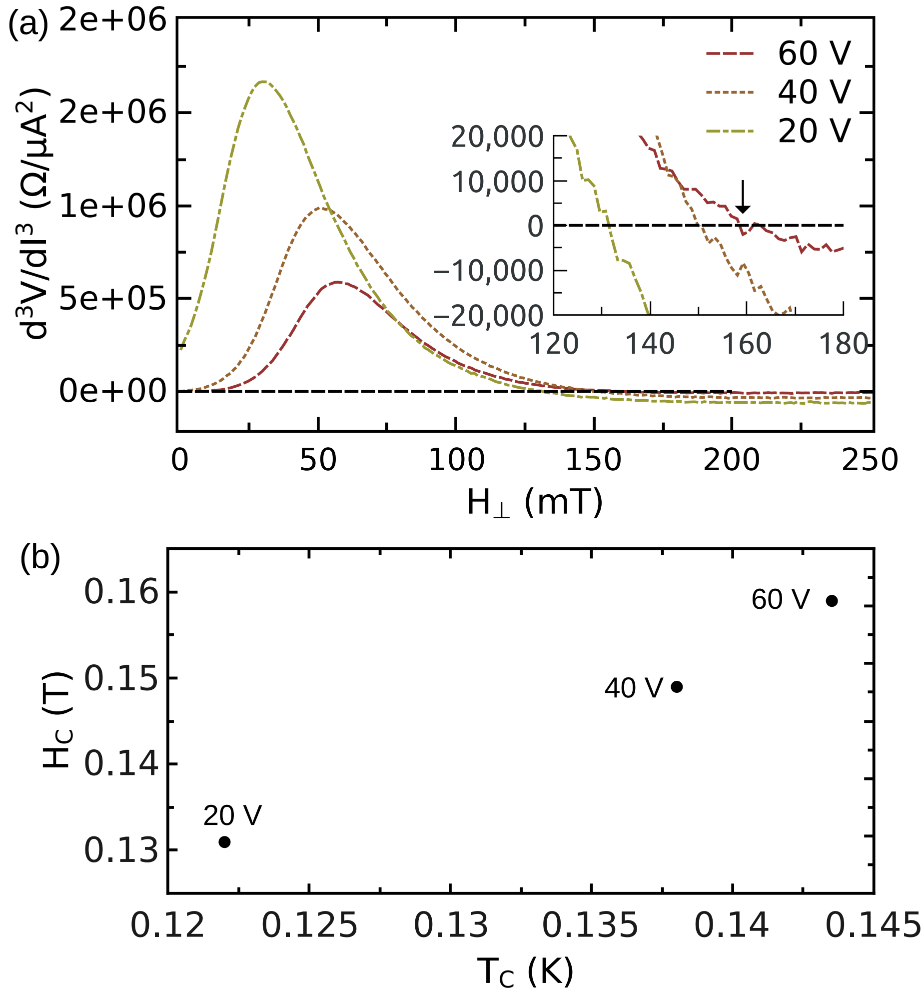

Figure 4.25. **(a)**, d^3V/dI^3 vs $H_\perp$ for different V_g's. The horizontal dashed line indicates the zero of d^3V/dI^3. The inset shows the zoomed in region near $d^3V/dI^3 = 0$. When the third derivative crosses this line as a function of the field, the system passes into an insulating state. The critical value of the field for $V_g = 60$ V is indicated by the arrow, $H_C = 159$ mT. **(b)** Measured H_C as a function of different measured T_C's for the different V_g's.

159 mT one sees the change from superconducting to insulating behaviour. Figure 4.25b shows the dependence of H_C on the measured transition temperature, T_C, for the different V_g's (the T_C values are from Fig. 4.6). It was argued by Fisher [**86**] and demonstrated by Hebard and Paalanen [**89**], that near the critical point of the disorder driven transition,

$H_C \sim T_C^{2/z}$, $z = 1$. We do not see such behaviour in our data, but that could be because at the measured gate voltages we are still relatively far from the gate voltage at which the SIT occurs in the gate-voltage tuned transition.

Using the values of H_C obtained from d^3V/dI^3 measurements we perform a scaling analysis of the MR data. Since the critical exponent product, $z\nu$, determines the universality class of the phase transition, we tried scaling our data with a number of values for $z\nu$. The results are shown in Fig. 4.26 for $V_g = 60$ V. For compactness, only four representative values of $z\nu$ are shown in the figure. It is found that the critical exponent product that best scales the data is $z\nu = 2.15$, as seen by the different temperature curves falling on top of one another. Among the two different universal values of $z\nu$ for which the magnetic field tuned SIT has been studied until now, $z\nu = 4/3 \approx 1.33$ or $z\nu = 7/3 \approx 2.33$ (more on the significance of these two values below), it appears that our data is closer to $z\nu = 7/3$. Therefore, we use $z\nu = 7/3$ to scale our MR data for the other V_g's. The scaled MR curves for all the V_g's using $z\nu = 7/3$ are shown in Fig. 4.27.

The critical exponent product $z\nu = 7/3$ is indicative of quantum percolation [**106**, **169**], while $z\nu = 4/3$ is indicative of classical percolation [**89**, **90**] as mechanisms for phase transitions. For inhomogeneous systems that show a phase transition from a conducting to a non-conducting state, quantum percolation signifies transport through charge tunneling (as opposed to direct transport) between two conducting regions across a non-conducting region. In the 2D SIT, the question is whether the principal charge transport is through Cooper pairs (bosons) or through electrons (fermions) as the magnetic field is

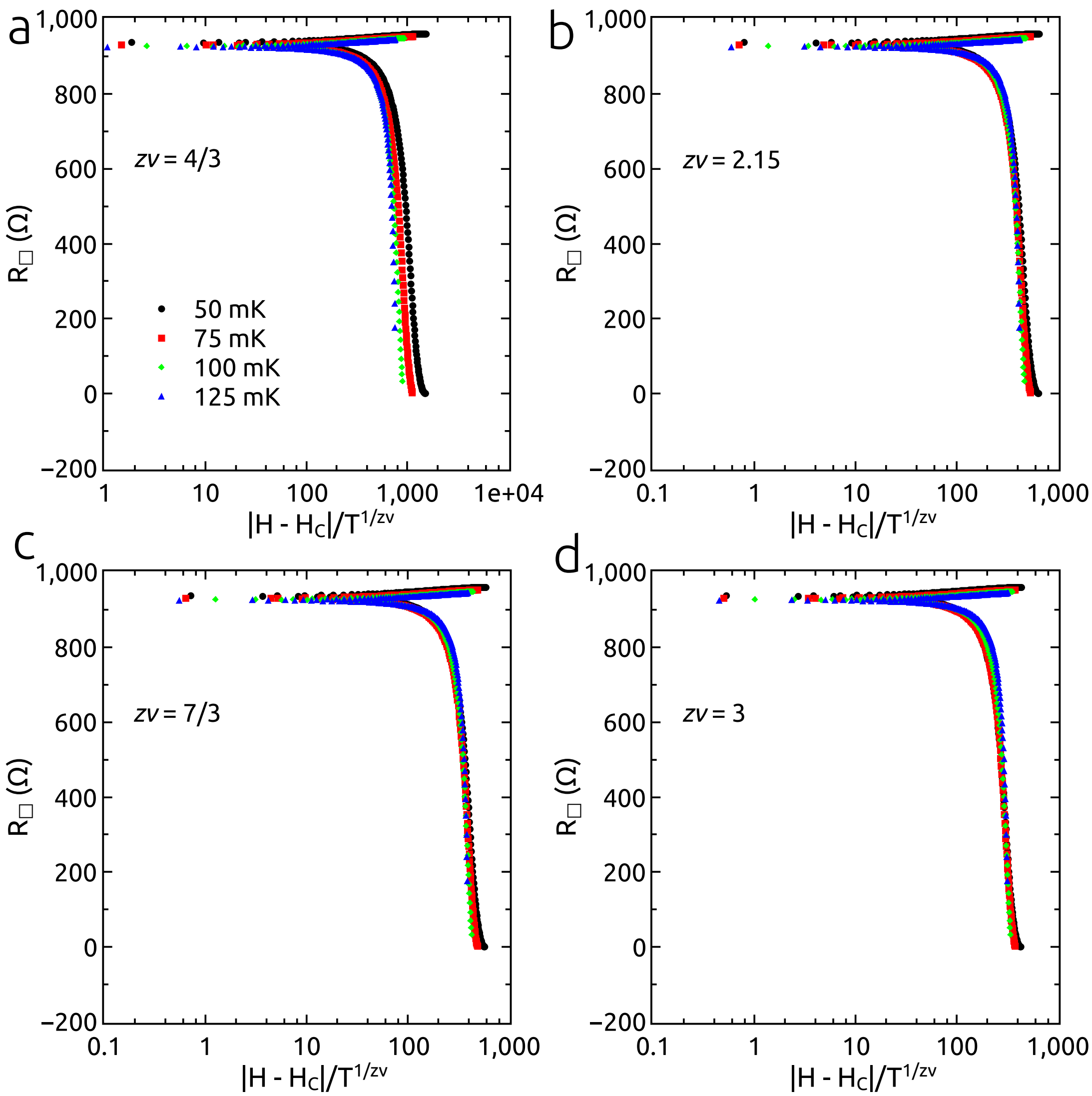

Figure 4.26. $R_\square$ vs $|H - H_C|/T^{1/z\nu}$ at $V_g = 60$ V for (a) $z\nu = 4/3$, (b) $z\nu = 2.15$, (c) $z\nu = 7/3$, and (d) $z\nu = 3$. $H_C = 159$ mT. The critical exponent product $z\nu = 2.15$ best scales the data, such that visually all the curves collapse onto each other. This value of $z\nu$ is close to $z\nu = 7/3$, which is expected where quantum percolation is dominant.

increased. Previous studies [**89**, **90**] of the magnetic field tuned SIT in thin film superconductors have yielded the critical exponent product $z\nu = 4/3$, which corresponds to transport through classical percolation. Usually this critical exponent product has been seen for films with a wide range of normal state resistances. For example, Hebard *et*

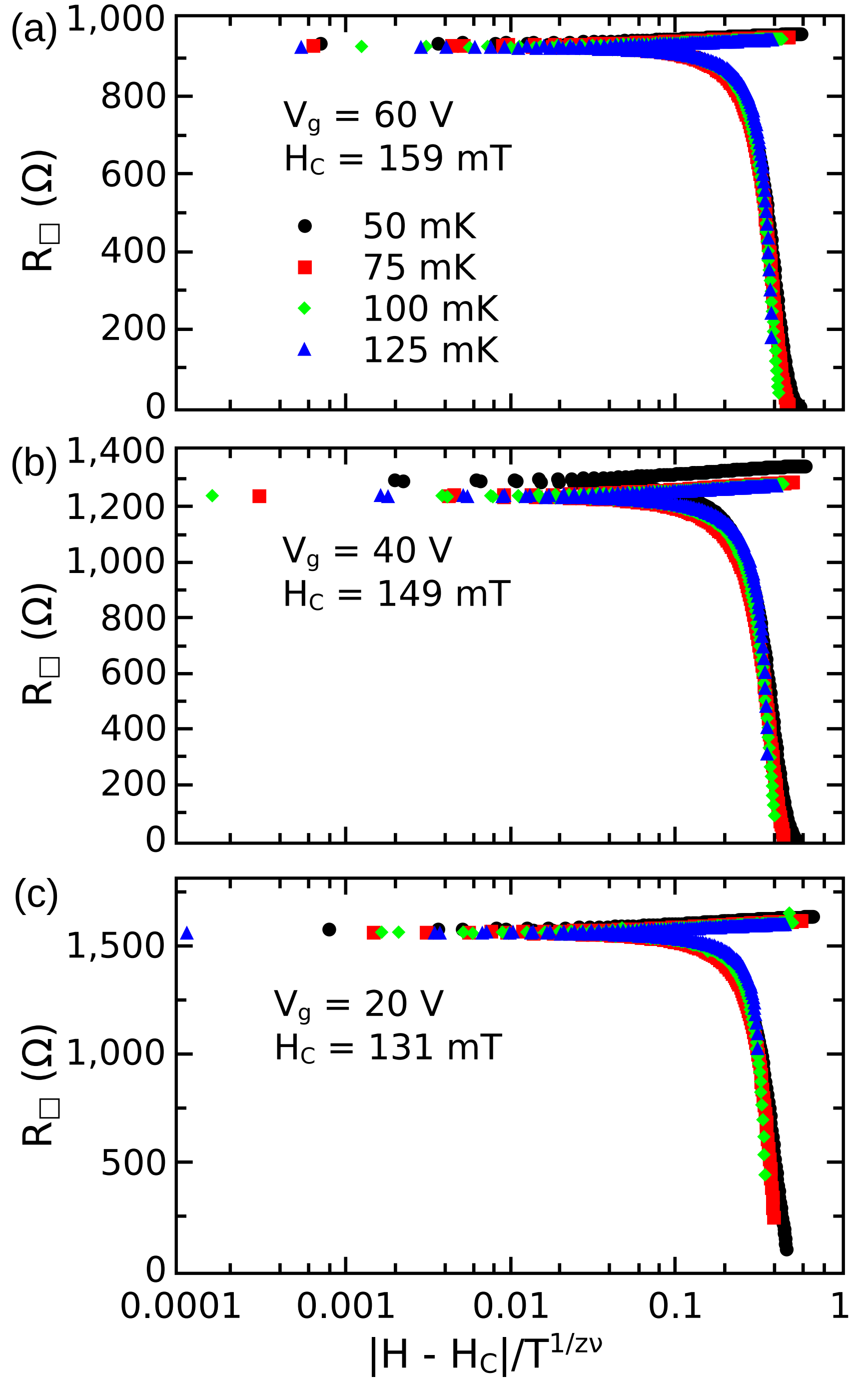

Figure 4.27. $R_{\square}$ vs $|H - H_C|/T^{1/z\nu}$ for (a) $V_g = 60$ V, (b) $V_g = 40$ V, and (c) $V_g = 20$ V. The critical exponent product $z\nu = 7/3$ is used to scale the data. The scaling is reasonably good, as seen by the fact that all the curves collapse onto each other.

al. [**89**] report a transition for InO_x films with $R_{\square}^{N} \sim 6$ kΩ, whereas Yazdani *et al.* [**90**] report a transition in $\alpha-$MoGe films with $R_{\square}^{N} \lesssim 2$ kΩ. On the other hand, the critical exponent product $z\nu = 7/3$ has been reported for high resistance InO_x films by Steiner *et al.* [**106**]. In contrast, our data shows a transition based on quantum percolation ($z\nu = 7/3$) for a relatively low resistance system (maximum $R_{\square}^{N} \approx 1.5$ kΩ at $V_g = 20$ V). It is difficult, however, to say if the transition is bosonic or fermionic, from the extracted value of $z\nu = 7/3$. A more detailed measurement, with a larger field and temperature range might give more insight into the nature of the transition.

CHAPTER 5

Conclusions and Outlook

The 2DEG formed at the interface of LAO/STO shows a rich variety of physical phenomena including superconductivity, ferromagnetism and the coexistence of the two. Through extensive transport measurements, we have characterized this 2DEG and found a number of interesting aspects. Among them is the very inhomogeneous nature of the electron system. We found that the resistance and the superconducting transition temperatures of two Hall bars fabricated on the same sample were very different, with the resistance values differing by a factor of about 2. Based on such observations we could conclude that the length scale of inhomogeneities was at least a few μms in our sample, although inhomogeneities at a smaller length scale may also be present. It is unclear whether such inhomogeneities occur due to local inhomogeneities in the chemical composition at the interface, for example due to oxygen vacancies, or they arise due to strong electron correlations and thus are of a more intrinsic nature. Local measurements of the electron system through techniques like scanning probe microscopy (SPM) will help shed more light on the matter. Development of a multi-mode low temperature scanning probe microscope (LT-SPM) is in advanced stages of completion [**170–172**] in the lab, and once finished, it will be employed to perform local probe microscopy on the system. A possible experiment is performing electrostatic force microscopy on the 2DEG, which can reveal if the electron system breaks up into puddles with different concentrations of electrical charges in different regions of the sample. Such a measurement would give information about the length scales of the inhomogeneities and also their evolution with temperature.

As reported by other groups, we also found that the properties of the 2DEG could be tuned by the application of a back-gate voltage, V_g. From the measurements of Hall effect we found evidence for multi-carrier transport in this system. This was seen in the increase of the Hall coefficient, R_H, with increasing V_g. Such behaviour could not be explained by a single, electron-like carrier. More detailed measurements on multiple samples are underway in the group by other graduate students in order to study the charge density dependence on V_g. These include the measurement of the induced charge density through a measurement of the capacitance of the 2DEG. By measuring the 2DEG quantum capacitance (i.e. geometry independent capacitance) at different V_g's, one can extract the density of states of the system and its evolution with V_g [**173**].

We also found that the application of V_g induces a superconductor to insulator transition (SIT) in this system. The superconducting transition temperature, T_C, and hence the strength of the superconducting order parameter is a non-monotonic function of V_g. The insulating state of the V_g tuned SIT was found to be weak, with contributions to its resistance from various mechanisms like weak localization, electron-electron interactions and even some superconducting fluctuations. It will be interesting to see if the system can be driven into a more deeply insulating regime by the application of a top-gate voltage. Efforts to make such top-gated devices are also underway in the group. Varada Bal has fabricated locally top-gated and globally back-gated structures on LAO/STO which can be made to mimic superconducting hybrid devices, like superconductor-insulator-superconductor (S-I-S) junctions, on the application of both top and back gate voltages [**121**]. Superconducting phase sensitive tests based on the Josephson effect will help reveal the symmetry of the superconducting order parameter. Specifically one studies the evolution of the product $I_C R_N$ with temperature to get information on the symmetry of the superconducting order parameter [**174**]. Here I_C is the critical current of the Josephson junction and R_N is its normal state resistance.

One of the major results of this thesis is the observation of the coexistence of superconductivity and ferromagnetism at the LAO/STO interface. We presented evidence of hysteretic magnetoresistance (MR) in the superconducting state in both parallel and perpendicular magnetic fields. We developed a model of the system through which the magnetization dynamics in the ferromagnet can give rise to the observed features in the MR, which are sharp peaks in resistance in the superconducting regime and sharp dips in resistance in the insulating regime. A multi-mode scanned probe study would elucidate further the relationship between the ferromagnetic and superconducting orders in this system. For example, simultaneous magnetic and electrostatic force microscopy (MFM and EFM) of the system would reveal whether the distribution of superconducting and ferromagnetic orders are correlated in our samples. A detailed MFM study of the sample would also help shed light on the formation of ferromagnetic domains in the system and how they evolve with both V_g and temperature.

The change of the MR features from peaks to dips as the system is tuned through the SIT is a consequence of the duality of the superconducting and insulating regimes in this system. Such a manifestation of duality in MR is new, and is a result of the coexistence of the superconductivity and ferromagnetism in this system. We have developed a phenomenological model based on thermal activation of vortices in the superconducting regime and of charges in the insulating regime which well fits the observed dependence of the MR features on the sweep rate of the external magnetic field.

Finally, we presented our results on a study of the perpendicular magnetic field tuned SIT at this interface. We showed that the insulating state reached in the magnetic field tuned SIT was also weak, at least in the field and temperature ranges measured. Through a measurement of d^3V/dI^3 as a function of $H_\perp$, we were able to determine the critical field of the transition. Scaling of the MR curves obtained at different temperatures yielded a critical exponent product $z\nu = 7/3$, which signifies transport through quantum percolation.

We conclude this chapter by showing the rich phase diagram of this system, schematically depicting both electric field (as applied by V_g) and the perpendicular magnetic field tuned SIT's. Figure 5.1 shows such a phase diagram. In this thesis, we have mapped out the various phase boundaries shown in the figure. While the transport measurements presented here suggest that the superconducting order parameter survives into the insulating state in the V_g tuned SIT, it is unclear if the insulating state reached in the magnetic field tuned transition has any Cooper pairs. A more detailed magnetotransport study of the system with increased field and temperature ranges of measurement will indicate if there are any signatures of Cooper pairs, like a giant peak in MR at large fields, on the insulating side of the transition.

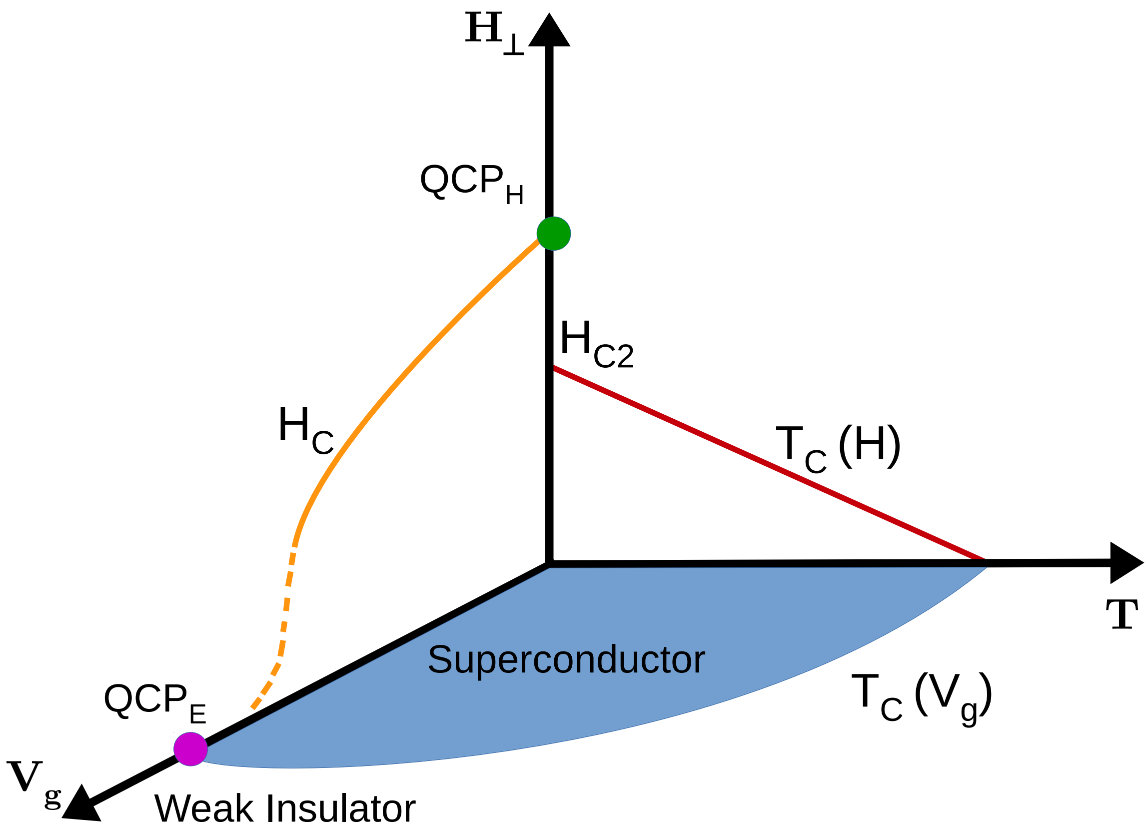

Figure 5.1. Schematic of the phase diagram in this system. The various phase boundaries shown here were mapped out and presented in this thesis.

References

[1] Nobel Lectures, Physics 1996-2000, Editor Gösta Ekspong, World Scientific Publishing Co., Singapore, 2002.

[2] Ohtomo, A., Hwang, H. Y., A high-mobility electron gas at the $LaAlO_3/SrTiO_3$ heterointerface. *Nature* **427**, 423-426 (2004).

[3] H. Y. Hwang, Y. Iwasa, M. Kawasaki, B. Keimer, N. Nagaosa and Y. Tokura, 'Emergent phenomena at oxide interfaces,' *Nature Materials* **11**, 103 (2012).

[4] Thiel, S., Hammerl, G., Schmehl, A., Schneider,C. W. and Mannhart J. Tunable Quasi-Two-Dimensional Electron Gases in Oxide Heterostructures. *Science* **313**, 1942-1945 (2006).

[5] Reyren, N., Thiel, S., Caviglia, A. D., Fitting Kourkoutis, L., Hammerl,G., Richter,C., Schneider,C. W., Kopp, T., Rëtschi, A.-S., Jaccard, D., Gabay, M., Muller, D. A., Triscone, J.-M. and Mannhart, J. Superconducting Interfaces Between Insulating Oxides. *Science* **317**, 1196-1199 (2007).

[6] Caviglia, A. D., Gariglio, S., Reyren, N., Jaccard, D., Schneider, T., Gabay, M., Thiel, S., Hammerl, G., Mannhart, J. and Triscone J.-M. Electric field control of the $LaAlO_3/SrTiO_3$ interface ground state. *Nature* **456**, 624-627 (2008).

[7] A. Brinkman, M. Huijben, M. van Zalk, J. Huijben, U. Zeitler, J. C. Maan, W. G. van der Weil, G. Rijnders, D. H. A. Blank and H. Hilgenkamp, 'Magnetic effects at the interface between non-magnetic oxides,' *Nature Materials* **6**, 493 (2007).

[8] M. Ben Shalom, C. W. Tai, Y. Lereah, M. Sachs, E. Levy, D. Rakhmilevitch, A. Palevski, Y. Dagan, 'Anisotropic magnetotransport at the $LaAlO_3/SrTiO_3$ interface,' Phys. Rev B **80**, 140403 (2009).

[9] C. Cen , S. Thiel, G. Hammerl, C. W. Schneider, K. E. Andersen, C. S. Hellberg, J. Mannhart and J. Levy, 'Nanoscale control of an interfacial metal-insulator transition at room temperature,' *Nature Materials* **7**, 298 (2008).

[10] Dikin, D. A., Mehta, M., Bark, C. W., Folkman, C. M., Eom, C. B. and Chandrasekhar, V. Coexistence of superconductivity and ferromagnetism in two dimensions. *Phys. Rev. Lett* **107**, 056802 (2011).

[11] Bert, J. A., Kalisky, B., Bell, C., Kim, M., Hikita, Y., Hwang, H. Y. and Moler, K. A. Direct imaging of the coexistence of ferromagnetism and superconductivity at the LaAlO3/SrTiO3 interface. *Nat. Phys.* **7**, 767-771 (2011).

[12] Li, L., Richter, C., Mannhart, J. and Ashoori, R. C. Coexistence of magnetic order and two-dimensional superconductivity at $LaAlO_3/SrTiO_3$ interfaces. *Nat. Phys.* **7**, 762-766 (2011).

[13] Girvin, S. M. Duality in Perspective. *Science* **274**, 524-525 (1996).

[14] J. Mannhart and D. G. Schlom, Oxide InterfacesAn Opportunity for Electronics, *Science* **327**, 1607 (2010).

[15] Douglas H. Lowndes, X.Y. Zheng, Shen Zhu, J. D. Budai and R. J. Warmack, *Appl. Phys. Lett.* **61**, 852 (1992).

[16] W. J. Lin, T. Y. Tseng, H. B. Lu, S. L. Tu, S. J. Yang and I. N. Lin, *J. Appl. Phys.* **77**, 6466 (1995).

[17] Andrei V. Bandura, Robert A. Evarestov and Yuri F. Zhukovskii, Energetic stability and photocatalytic activity of $SrTiO_3$ nanowires: ab initio simulations, *RSC Adv.*, **5**, 24115 (2015).

[18] A. F. Santander-Syro *et al.*, Two-dimensional electron gas with universal subbands at the surface of $SrTiO_3$, *Nature* **469**, 189193 (2011).

[19] W. Meevasana *et al.*, Creation and control of a two-dimensional electron liquid at the bare $SrTiO_3$ surface, *Nature Materials* **10**, 114 (2011).

[20] N.C. Plumb *et al.*, Mixed Dimensionality of Confined Conducting Electrons in the Surface Region of $SrTiO_3$, *Phys. Rev. Lett.* **113**, 086801 (2014).

[21] A. F. Santander-Syro *et al.*, Giant spin splitting of the two-dimensional electron gas at the surface of $SrTiO_3$, *Nature Materials* **13**, 1085 (2014).

[22] R. C. Neville, B. Hoeneisen, and C. A. Mead, Permittivity of Strontium Titanate, *J. Appl. Phys.* **43**, 2124 (1972).

[23] C. S. Koonce, Marvin Cohen, J. F. Schooley, W. R. Hosler, and E. R. Pfeiffer, *Phys. Rev.* **163**, 380 (1967).

[24] J. F. Schooley, W. R. Hosler, and Marvin L. Cohen, Superconductivity in Semiconducting $SrTiO_3$, *Phys. Rev. Lett.* **12**, 474 (1964).

[25] E. R. PFEIFFER and J. F. SCHOOLEY, *Phys. Lett.* **29A**, 589 (1969).

[26] G. Binnig, A. Baratoff, H. E. Hoenig, and J. G. Bednorz, *Phys. Rev. Lett.* **45**, 1352 (1980).

[27] Hiroshi Suzuki *et al.*, *J. Phys. Soc. Jpn.* **65**, 1529 (1996).

[28] David Olaya, Feng Pan, Charles T. Rogers, and John C. Price, *Appl. Phys. Lett.* **84**, 4020 (2004).

[29] A. Spinelli, M. A. Torija, C. Liu, C. Jan, and C. Leighton, *Phys. Rev. B* **81**, 155110 (2010).

[30] A. H. Kahn and A. J. Leyendecker, Electronic Energy Bands in Strontium Titanate, *Phys. Rev.* **135**, A1321 (1964).

[31] L. F. Mattheiss, Energy Bands for $KNiF_3$, $SrTiO_3$, $KMoO_3$, and $KTaO_3$, *Phys. Rev. B* **6**, 4718 (1972).

[32] A. D. Caviglia, M. Gabay, S. Gariglio, N. Reyren, C. Cancellieri, and J.-M. Triscone, 'Tunable Rashba Spin-Orbit Interaction at Oxide Interfaces,' *Phys. Rev. Lett.* **104**, 126803 (2010).

[33] M. Ben Shalom, M. Sachs, D. Rakhmilevitch, A. Palevski, Y. Dagan, 'Tuning Spin-Orbit Coupling and Superconductivity at the $SrTiO_3/LaAlO_3$ Interface: A Magnetotransport Study,' *Phys. Rev. Lett.* **104**, 126802 (2010).

[34] H. P. R. Frederikse, W. R. Thurber, and W. R. Hosler, Electronic Transport in Strontium Titanate, *Phys. Rev.* **134**, A442 (1964).

[35] J. F. Schooley, W. R. Hosler, E. Ambler, J. H. Becker, Marvin L. Cohen, and C. S. Koonce, Dependence of the Superconducting Transition Temperature on Carrier Concentration in Semiconducting $SrTiO_3$, *Phys. Rev. Lett.* **14**, 305 (1965).

[36] MARVIN L. COHEN, The Existence of a Superconducting State in Semiconductors, *Rev. Mod. Phys.* **36**, 240 (1964).

[37] Marvin L. Cohen, Superconductivity in Many-Valley Semiconductors and in Semimetals, *Phys. Rev.* **134**, A511 (1964).

[38] J. Bardeen, L. N. Cooper, and J. R. Schrieffer, 'Theory of Superconductivity,' *Phys. Rev.*, **108**, 1175 (1957).

[39] Tinkham, M. *Introduction to Superconductivity*, 2nd edition (McGraw-Hill, 1996).

[40] Evgeny Y. Tsymbal, Elbio R. A. Dagotto, Chang-Beom Eom, Ramamoorthy Ramesh. *Multifunctional Oxide Heterostructures.* (Oxford University Press, USA, 2012).

[41] R. Pentcheva and W.E. Pickett, Charge localization or itineracy at $LaAlO_3SrTiO_3$ interfaces: Hole polarons, oxygen vacancies, and mobile electrons. *Phys. Rev. B*, **74**, 035112 (2006).

[42] Min Sik Park, S. H. Rhim, and Arthur J. Freeman, 'Charge compensation and mixed valency in $LaAlO_3SrTiO_3$ heterointerfaces studied by the FLAPW method,' *Phys. Rev. B*, **74**, 205416 (2006).

[43] NAOYUKI NAKAGAWA, HAROLD Y. HWANG AND DAVID A. MULLER, 'Why some interfaces cannot be sharp,' *Nature Materials* **5**, 204 (2006).

[44] Tsuneya Ando, Alan B. Fowler, and Frank Stern, Electronic properties of two-dimensional systems, *Rev. Mod. Phys.* **54**, 437 (1982).

[45] N. W. Ashcroft and N. D. Mermin, *Solid State Physics*, 1st edition (Saunders, 1976).

[46] K. Yoshimatsu, R. Yasuhara, H. Kumigashira, and M. Oshima, Origin of Metallic States at the Heterointerface between the Band Insulators $LaAlO_3$ and $SrTiO_3$, *Phys. Rev. Lett.* **101**, 026802 (2008).

[47] Bo-Chao Huang *et al.*, Mapping Band Alignment across Complex Oxide Heterointerfaces, *Phys. Rev. Lett.* **109**, 246807 (2012).

[48] Zoran S. Popovic, Sashi Satpathy, and Richard M. Martin, 'Origin of the Two-Dimensional Electron Gas Carrier Density at the $LaAlO_3$ on $SrTiO_3$ Interface,' *Phys. Rev. Lett.*, **101**, 256801 (2008).

[49] G. Herranz, F. Sanchez, N. Dix, M. Scigaj and J. Fontcuberta, High mobility conduction at (110) and (111) $LaAlO_3SrTiO_3$ interfaces, *Scientific Reports* **2**, 758 (2012).

[50] Alexey Kalabukhov, Robert Gunnarsson, Johan Börjesson, Eva Olsson, Tord Claeson, and Dag Winkler, Effect of oxygen vacancies in the $SrTiO_3$ substrate on the electrical properties of the $LaAlO_3SrTiO_3$ interface. *Phys. Rev. B* **75**, 121404(R) (2007).

[51] W. Siemons, G. Koster, H. Yamamoto, W. A. Harrison, G. Lucovsky, T. H. Geballe, D. H. A. Blank, M. R. Beasley, 'Origin of Charge Density at $LaAlO_3$ on $SrTiO_3$ Heterointerfaces: Possibility of Intrinsic Doping,' *Phys. Rev Lett* **98**, 196802 (2007).

[52] O. N. Tufte and P. W. Chapman. Electron Mobility in Semiconducting Strontium Titanate. *Phys. Rev.* **155**, 796802 (1967).

[53] P. R. Wilmott *et al.* Structural Basis for the Conducting Interface between $LaAlO_3$ and $SrTiO_3$. *Phys. Rev. Lett.* **99**, 155502 (2007).

[54] Yanwu Xie, Christopher Bell, Yasuyuki Hikita and Harold Y. Hwang, 'Tuning the Electron Gas at an Oxide Heterointerface via Free Surface Charges,' *Adv. Mat.*, **23**, 1744 (2011).

[55] R. Pentcheva, R. Arras, K. Otte, V. G. Ruiz, W. E. Pickett, 'Termination control of electronic phases in oxide thin films and interfaces: $LaAlO_3/SrTiO_3$ (001),' *Phil. Trans. R. Soc. A*, **370**, 4904 (2012).

[56] Yanwu Xie *et al.*, Charge Writing at the $LaAlO_3SrTiO_3$ Surface, *Nano Lett.* **10**, 25882591 (2010).

[57] Scott A. Chambers, Understanding the mechanism of conductivity at the $LaAlO_3SrTiO_3$(001) interface, *Surface Science* **605**, 11331140 (2011).

[58] R. Pentcheva, M. Huijben, K. Otte, W. E. Pickett, J. E. Kleibeuker, J. Huijben, H. Boschker, D. Kockmann, W. Siemons, G. Koster, H. J. W. Zandvliet, G. Rijnders, D. H. A. Blank, H. Hilgenkamp, and A. Brinkman, Parallel Electron-Hole Bilayer Conductivity from Electronic Interface Reconstruction, *Phys. Rev. Lett.* **104**, 166804 (2010).

[59] E I Rashba and V I Sheka, *Fiz. Tverd. Tela: Collected Papers* **2**, 16276 (1959). (Original paper published in Russian, english translation available at this url: http://iopscience.iop.org/1367-2630/17/5/050202/media)

[60] Yu A Bychkov and E I Rashba, Oscillatory effects and the magnetic susceptibility of carriers in inversion layers, *Journal of Physics C: Solid State Phys* **17**, 6039 (1984).

[61] William Shockley, On the Surface States Associated with a Periodic Potential, *Phys. Rev.* **56**, 317 (1939).

[62] Igor Tamm, On the possible bound states of electrons on a crystal surface, *Phys. Z. Soviet Union* **1**, 733 (1932).

[63] Jules D. Levine and Peter Mark, Theory and Observation of Intrinsic Surface States on Ionic Crystals, *Phys. Rev.* **144**, 751 (1966).

[64] M. Sing *et al.*, Profiling the Interface Electron Gas of $LaAlO_3/SrTiO_3$ Heterostructures with Hard X-Ray Photoelectron Spectroscopy, *Phys. Rev. Lett.*, **102**, 176805 (2009).

[65] G. Herranz *et al.*, High Mobility in $LaAlO_3/SrTiO_3$ Heterostructures: Origin, Dimensionality, and Perspectives, *Phys. Rev. Lett.*, **98**, 216803 (2007).

[66] M. Basletic *et al.*, Mapping the spatial distribution of charge carriers in $LaAlO_3/SrTiO_3$ heterostructures, *Nature Materials* **7**, 621 (2008).

[67] Massimiliano Stengel, First-Principles Modeling of Electrostatically Doped Perovskite Systems, *Phys. Rev. Lett.*, **106**, 136803 (2011).

[68] S Gariglio, A Fte and J-M Triscone, Electron confinement at the $LaAlO_3/SrTiO_3$ interface, *J. Phys.: Condens. Matter* **27**, 283201 (2015).

[69] R. Pentcheva and W.E. Pickett, 'Correlation-Driven Charge Order at the Interface between a Mott and a Band Insulator,' *Phys. Rev. Lett.*, **99**, 016802 (2007).

[70] R. Pentcheva and W.E. Pickett, 'Ionic relaxation contribution to the electronic reconstruction at the $n-$type $LaAlO_3/SrTiO_3$ interface,' *Phys. Rev. B*, **78**, 205106 (2008).

[71] Karolina Janicka, Julian P. Velev, and Evgeny Y. Tsymbal, 'Quantum Nature of Two-Dimensional Electron Gas Confinement at $LaAlO_3/SrTiO_3$ Interfaces,' *Phys. Rev. Lett.*, **102**, 106803 (2009).

[72] Michaeli, K., Potter, A. C., and Lee, P. A. *Phys. Rev. Lett.* **108**, 117003 (2012).

[73] N. Pavlenko, T. Kopp, E. Y. Tsymbal, G. A. Sawatzky, and J. Mannhart, *Phys. Rev. B* **85**, 020407(R) (2012).

[74] Peter Fulde and Richard A. Ferrell, 'Superconductivity in a Strong Spin-Exchange Field,' *Phys. Rev.*, **135**, A550 (1964). A. I. Larkin and Y. N. Ovchinikov, *Sov. Phys. JETP*, **20**, 762 (1965).

[75] Victor Barzykin and Lev P. Gorkov, 'Inhomogeneous Stripe Phase Revisited for Surface Superconductivity,' *Phys. Rev. Lett.* **89**, 227002 (2002).

[76] Olga Dimitrova and M. V. Feigelman, 'Theory of a two-dimensional superconductor with broken inversion symmetry,' *Phys. Rev. B* **76**, 014522 (2007).

[77] C. Zener, 'Interaction Between the d Shells in the Transition Metals,' *Phys. Rev.*, **81**, 440 (1951).

[78] I. S. Elfimov, S. Yunoki, and G. A. Sawatzky, 'Possible Path to a New Class of Ferromagnetic and Half-Metallic Ferromagnetic Materials,' *Phys. Rev. Lett.* **89**, 216403 (2002).

[79] M. Mehta *et al.* Evidence for chargevortex duality at the $LaAlO_3/SrTiO_3$ interface. *Nature Communications* **3**, Article number: 955 (2012).

[80] A P Petrović, A Paré, T R Paudel, K Lee, S Holmes, C H W Barnes, A David, T Wu, E Y Tsymbal and C Panagopoulos, Emergent vortices at a ferromagnetic superconducting oxide interface, *New Journal of Physics* **16**, 103012 (2014).

[81] B. Kalisky *et al.* Critical thickness for ferromagnetism in $LaAlO_3/SrTiO_3$ heterostructures. *Nature Communications* **3**, 922 (2012).

[82] Marc Gabay and Jean-Marc Triscone, Oxide heterostructures: Hund rules with a twist, *Nature Physics* **9**, 610611 (2013).

[83] Gang Chen and Leon Balents, Ferromagnetism in Itinerant Two-Dimensional t_{2g} Systems, *Phys. Rev. Lett.* **110**, 206401 (2013).

[84] Sumilan Banerjee, Onur Erten and Mohit Randeria, Ferromagnetic exchange, spinorbit coupling and spiral magnetism at the $LaAlO_3/SrTiO_3$ interface, *Nature Physics* **9**, 626 (2013).

[85] Fisher, M. P. A., Grinstein, G. and Girvin, S. M. *Phys. Rev. Lett.* **64**, 587-590 (1990).

[86] Fisher, M. P. A., Quantum phase transitions in disordered two-dimensional superconductors, *Phys. Rev. Lett.* **65**, 923-926 (1990).

[87] Haviland, D. B., Liu, Y. and Goldman, A. M. *Phys. Rev. Lett.* **62**, 2180-2183 (1989).

[88] Jaeger, H. M., Haviland, D. B., Orr, B. G., Goldman, A. M. Onset of superconductivity in ultrathin granular metal films. *Phys. Rev. B* **40**, 182-196 (1989).

[89] Hebard, A. F. and Paalanen, M. A. *Phys. Rev. Lett.* **65**, 927-930 (1990).

[90] A. Yazdani and A. Kapitulnik, *Phys. Rev. Lett.* **74**, 3037 (1995).

[91] S.J. Lee and J.B. Ketterson, *Phys. Rev. Lett.* **64**, 3078 (1990).

[92] T. I. Baturina, C. Strunk, M. R. Baklanov, and A. Satta, *Phys. Rev. Lett.* **98**, 127003 (2007).

[93] H. S. J. van der Zant, F. C. Fritschy, W. J. Elion, L. J. Geerligs, and J. E. Mooij, *Phys. Rev. Lett.* **69**, 2971 (1992).

[94] Seongshik Oh, Trevis A. Crane, D. J. Van Harlingen, and J. N. Eckstein, *Phys. Rev. Lett.* **96**, 107003 (2006).

[95] Kouichi Semba and Azusa Matsuda, *Phys. Rev. Lett.* **86**, 496 (2001).

[96] J. Biscaras, N. Bergeal, S. Hurand, C. Feuillet-Palma, A. Rastogi, R. C. Budhani, M. Grilli, S. Caprara, and J. Lesueur, *Nat. Mat.* **12** 542 (2013).

[97] Subir Sachdev, *Quantum Phase Transitions*, 2$^{\text{nd}}$ edition (Cambridge University Press; May 9, 2011).

[98] S. L. Sondhi, S. M. Girvin, J. P. Carini, and D. Shahar, 'Continuous quantum phase transitions,' *Rev. Mod. Phys.* **69**, 315 (1997).

[99] A. M. Finkelshtein, *JETP Lett.* **45**, 46 (1987).

[100] M. Mehta *et al.*, 'Magnetic field tuned superconductor-insulator transition at the $LaAlO_3/SrTiO_3$ interface,' *Phys. Rev. B*, **90**, 100506(R) (2014).

[101] A. M. Goldman and N. Markovic, 'SuperconductorInsulator Transitions in the TwoDimensional Limit,' *Physics today* pp. 39 (1998).

[102] Peierls R. E., *Ann. Inst. Henri Poincar* **5**, 177-222 (1935).

[103] J M Kosterlitz and D J Thouless, 'Ordering, metastability and phase transitions in two-dimensional systems,' *J. Phys. C: Solid State Phys.* **6**, 1181 (1973). V. L.

Berezinskii, *Zh. Eksp. Teor. Fiz.* **61**, 1144 (1971). V. L. Berezinskii, *Sov. Phys. JETP* **34**, 610 (1972).

[104] For a review of the BKT transition, see J. E. Mooij in *Percolation, Localization and Superconductivity*, A. M. Goldman, S. Wolf, eds., (Plenum, New York; 1984) pp. 433.

[105] A. J. Rimberg, T. R. Ho, . Kurdak, John Clarke, K. L. Campman, and A. C. Gossard, 'Dissipation-Driven Superconductor-Insulator Transition in a Two-Dimensional Josephson-Junction Array,' *Phys. Rev. Lett.* **78**, 2632 (1997).

[106] M. Steiner, N.P. Breznay, and A. Kapitulnik, *Phys. Rev. B* **77**, 212501 (2008).

[107] J. M. Valles, Jr., R. C. Dynes, and J. P. Garno, 'Electron tunneling determination of the order-parameter amplitude at the superconductor-insulator transition in 2D,' *Phys. Rev. Lett.* **69**, 3567 (1992).

[108] Jonghwa Eom, Ph.D. Thesis, Northwestern University (1998).

[109] Chen-jung Chien, Ph.D. Thesis, Northwestern University (1998).

[110] Jose Aumentado, Ph.D. Thesis, Northwestern University (2000).

[111] Zhigang Jiang, Ph.D. Thesis, Northwestern University (2005).

[112] Zhengfan Zhang, Ph.D. Thesis, Northwestern University (2006).

[113] Paul Cadden-Zimansky, Ph.D. Thesis, Northwestern University (2008).

[114] Park, J. W., Bogorin, D.F., Cen, C., Felker, D.A., Zhang, Y., Nelson, C.T., Bark, C.W., Folkman, C.M., Pan, X.Q., Rzchowski, M.S., Levy, J. and Eom, C.B. Creation of a two-dimensional electron gas at an oxide interface on silicon. *Nat. Comm.* **1**, 94 (2010).

[115] Bark, C. W., Felker, D. A., Wang, Y., Zhang, Y., Jang, H. W., Folkman, C. M., Park, J. W., Baek, S. H., Zhou, H., Fong, D. D., Pan, X. Q., Tsymbal, E. Y., Rzchowski, M. S., and Eom, C. B. Tailoring a two-dimensional electron gas at the $LaAlO_3/SrTiO_3$ (001) interface by epitaxial strain. *Proc. Natl. Acad. Sci.* **108**, 4720-4724 (2011).

[116] Park, J. W. and Baek, S. H. and Bark, C. W. and Biegalski, M. D. and Eom, C. B., Quasi-single-crystal (001) $SrTiO_3$ templates on Si, *Applied Physics Letters* **95**, 061902 (2009).

[117] Kai Wang, Laser Based Fabrication of Graphene, in Advances in Graphene Science, Dr. M. Aliofkhazraei (Ed.), InTech (2013). Available from: http://www.intechopen.com/books/advances-in-graphene-science/laser-based-fabrication-of-graphene.

[118] Howard M. Smith and A. F. Turner, Vacuum Deposited Thin Films Using a Ruby Laser, *Applied Optics* **4**, 147-148 (1965).

[119] Douglas H. Lowndes, D. B. Geohegan, A. A. Puretzky, D. P. Norton, C. M. Rouleau, Synthesis of Novel Thin-Film Materials by Pulsed Laser Deposition, *Science* **273**, 898-903 (1996).

[120] Ayahiko Ichimiya and Philip I. Cohen, *Reflection High-Energy Electron Diffraction*, 1st edition (Cambridge University Press, 2004).

[121] Bal, V. V. and Mehta, M. M. and Ryu, S. and Lee, H. and Folkman, C. M. and Eom, C. B. and Chandrasekhar, V., Gate-tunable superconducting weak link behavior in top-gated $LaAlO_3$-$SrTiO_3$, *Applied Physics Letters* **106**, 212601 (2015).

[122] For a very "practitioner's" explanation of dilution refrigerators, see *Experimental Techniques in Condensed Matter Physics at Low Temperatures*, R C Richardson and E N Smith, Eds, (Addison Wesley, 1988). The book is full of useful tidbits needed to run low temperature apparatus.

[123] Venkat Chandrasekhar, Ph.D. Thesis, Yale University (1989).

[124] Sam Davis *et al.*, manuscript in preparation.

[125] S. Yunoki, J. Hu, A. L. Malvezzi, A. Moreo, N. Furukawa, and E. Dagotto, Phase Separation in Electronic Models for Manganites, *Phys. Rev. Lett.* **80**, 845 (1998).

[126] M. Uehara, S. Mori, C. H. Chen and S.-W. Cheong. Percolative phase separation underlies colossal magnetoresistance in mixed-valent manganites. *Nature* **399**, 560-563 (1999).

[127] Kenjiro K. Gomes *et al.* Visualizing pair formation on the atomic scale in the high-T_c superconductor $Bi_2Sr_2CaCu_2O_{8+\delta}$. *Nature* **447**, 569-572 (2007).

[128] K. M. Lang *et al.* Imaging the granular structure of high-T_c superconductivity in underdoped $Bi_2Sr_2CaCu_2O_{8+\delta}$, *Nature* **415**, 412 (2002).

[129] Ariando *et al.*, Electronic phase separation at the $LaAlO_3/SrTiO_3$ interface, *Nat. Comm.* **2**, 188 (2010).

[130] Z. Ristic *et al.*, Nanoscale modulation of the density of states at the conducting interface between $LaAlO_3$ and $SrTiO_3$ band insulators, *Europhysics Letters* **93**, 17004 (2011)

[131] S. Caprara, F. Peronaci, and M. Grilli, Intrinsic Instability of Electronic Interfaces with Strong Rashba Coupling, *Phys. Rev. Lett.* **109**, 196401 (2012).

[132] H.-M. Christen, J. Mannhart, E. J. Williams, and Ch. Gerber, Dielectric properties of sputtered $SrTiO_3$ films, *Phys. Rev. B* **49**, 12095 (1994).

[133] E. H. Hall, On a New Action of the Magnet on Electric Currents, *American Journal of Mathematics* **2**, 287-292 (1879).

[134] Arjun Joshua, S. Pecker, J. Ruhman, E. Altman and S. Ilani, A universal critical density underlying the physics of electrons at the $LaAlO_3/SrTiO_3$ interface, *Nature Communications* **3**, Article number: 1129 (2012).

[135] C. Bell, S. Harashima, Y. Kozuka, M. Kim, B. G. Kim, Y. Hikita, and H. Y. Hwang, Dominant Mobility Modulation by the Electric Field Effect at the $LaAlO_3/SrTiO_3$ Interface, *Phys. Rev. Lett.* **103**, 226802 (2009).

[136] N. Mason and A. Kapitulnik, Dissipation Effects on the Superconductor-Insulator Transition in 2D Superconductors, *Phys. Rev. Lett.* **82**, 5341 (1999).

[137] B. I. Halperin, David R. Nelson, Resistive transition in superconducting films, *Journal of Low Temperature Physics* **36**, 599-616 (1979).

[138] M. R. Beasley, J. E. Mooij, T. P. Orlando, Possibility of Vortex-Antivortex Pair Dissociation in Two-Dimensional Superconductors, *Phys. Rev. Lett.* **42**, 1165 (1979).

[139] Schneider, T., Caviglia, A. D., Gariglio, S., Reyren, N. and Triscone, J. -M. Electrostatically-tuned superconductor-metal-insulator quantum transition at the $LaAlO_3/SrTiO_3$ interface. *Phys. Rev. B* **79**, 184502 (2009).

[140] Patrick A. Lee and T. V. Ramakrishnan, Disordered electronic systems, *Rev. Mod. Phys.* **57**, 287 (1985).

[141] B. L. Altshuler, D. Khmel'nitzkii, A. I. Larkin, and P. A. Lee, Magnetoresistance and Hall effect in a disordered two-dimensional electron gas, *Phys. Rev. B* **22**, 5142 (1980).

[142] P. Santhanam, S. Wind, and D. E. Prober, Localization, superconducting fluctuations, and superconductivity in thin films and narrow wires of aluminum, *Phys. Rev. B* **35**, 3188 (1987).

[143] N.F. Mott and E.A. Davis, *Electronic processes in non-crystalline materials*, (Clarendon Press, 1971).

[144] A. Parendo, K. H. Sarwa B. Tan, and A. M. Goldman, Electrostatic and parallel-magnetic-field tuned two-dimensional superconductor-insulator transitions, *Phys. Rev. B* **73**, 174527 (2006).

[145] Valerii M. Vinokur *et al.*, Superinsulator and quantum synchronization, *Nature* **452**, 613-615 (2008).

[146] For a review of EEI, see *Electron-Electron Interactions in Disordered Systems*, A.L. Efros and M. Pollak (Eds.), (Elsevier, 1985).

[147] Sadamichi Maekawa, Hidetoshi Fukuyama, Magnetoresistance in Two-Dimensional Disordered Systems: Effects of Zeeman Splitting and Spin-Orbit Scattering, *Journal of the Physical Society of Japan* **50**, 2516 (1981).

[148] Haviland, D. B., Liu, Y. and Goldman, A. M. Onset of superconductivity in the two-dimensional limit. *Phys. Rev. Lett* **62**, 2180-2183 (1989).

[149] Fazio, R. and Schon, G. Charge and vortex dynamics in arrays of tunnel junctions. *Phys. Rev. B* **43**, 5307-5320 (1991).

[150] van der Zant, H. S. J., Fritschy, F. C., Elion, W. J., Geerligs, L. J. and Mooij, J. E. Field-induced superconductor-to-insulator transitions in Josephson-junction arrays. *Phys. Rev. Lett* **69**, 2971-2974 (1992).

[151] S. S. Saxena, P. Agarwal, K. Ahilan, F. M. Grosche, R. K. W. Haselwimmer, M. J. Steiner, E. Pugh, I. R. Walker, S. R. Julian, P. Monthoux, G. G. Lonzarich, A. Huxley, I. Sheikin, D. Braithwaite, J. Flouquet, 'Superconductivity on the border of itinerant-electron ferromagnetism in UGe_2,' Nature **406**, 587 (2000).

[152] D. Aoki, A. Huxley, E. Ressouche, D. Braithwaite, J. Flouquet, J. Brison, E. Lhotel, C. Paulsen, 'Coexistence of superconductivity and ferromagnetism in URhGe,' Nature **413**, 613 (2001).

[153] C. Pfleiderer, M. Uhlarz, S. M. Hayden, R. Vollmer, H. v. Löhneysen, N. R. Bernhoeft and G. G. Lonzarich, 'Coexistence of superconductivity and ferromagnetism in the d-band metal $ZrZn_2$, Nature **412**, 58 (2001).

[154] I. Felner, U. Asaf, Y. Levi, O. Millo, 'Coexistence of magnetism and superconductivity in $R_1.4Ce_0.6RuSr_2Cu_2O_10-$ (R=Eu and Gd),' Phys. Rev B **55**, R3374 (1997).

[155] Kittel, C., *Introduction to Solid State Physics*, 7th edition (Wiley; July 12, 1995).

[156] Kim, J. B., Akinaga, H. and Kim, J. Direct observation of the spin configurations of vertical Bloch line. *Appl. Phys. Lett.* **98**, 052510 (2011).

[157] For a review of vortex physics in superconductors, see G. Blatter and V. B. Geshkenbein, Chapter 12, *Vortex Matter*, in *Superconductivity Volume 1: Conventional and Unconventional Superconductors*, Bennemann, Karl-Heinz, Ketterson, John B. (Eds.), (Springer-Verlag Berlin Heidelberg, 2008).

[158] R. M. Fernandes, J. T. Haraldsen, P. Wlfle, and A. V. Balatsky, Two-band superconductivity in doped $SrTiO_3$ films and interfaces, *Phys. Rev. B* **87**, 014510 (2013).

[159] Jonathan M. Edge, Alexander V. Balatsky, Upper critical field as a probe for multiband superconductivity in bulk and interfacial STO, arXiv:1401.5318v3 [cond-mat.supr-con] (2014).

[160] Bertrand I. Halperin, Gil Refael, and Eugene Demler, RESISTANCE IN SUPERCONDUCTORS, *International Journal of Modern Physics B* **24**, 4039 (2010).

[161] E. Beaurepaire, J.-C. Merle, A. Daunois, and J.-Y. Bigot, Ultrafast Spin Dynamics in Ferromagnetic Nickel, *Phys. Rev. Lett.* **76**, 4250 (1996).

[162] The Object Oriented MicroMagnetic Framework (OOMMF) project at ITL/NIST, http://math.nist.gov/oommf/.

[163] Langer, J. S., Ambegaokar, V. Intrinsic Resistive Transition in Narrow Superconducting Channels. *Phys. Rev.* **164**, 498-510 (1967).

[164] McCumber, D. E., Halperin, B. I. Time Scale of Intrinsic Resistive Fluctuations in Thin Superconducting Wires. *Phys. Rev. B* **1**, 1054-1070 (1970).

[165] Shimshoni, E., Auerbach, A., Kapitulnik, A. Transport through Quantum Melts. *Phys. Rev. Lett.* **80**, 3352-3355 (1998).

[166] M. A. Steiner and A. Kapitulnik, Superconductivity in the insulating phase above the field-tuned superconductorinsulator transition in disordered indium oxide films, *Physica C* **422**, 16 (2005).

[167] G. Sambandamurthy, L. W. Engel, A. Johansson, and D. Shahar, Superconductivity-Related Insulating Behavior, *Phys. Rev. Lett.* **92**, 107005 (2004).

[168] Shih-Ying Hsu, J. A. Chervenak, and J. M. Valles, Jr., Magnetic Field Enhanced Order Parameter Amplitude Fluctuations in Ultrathin Films near the Superconductor-Insulator Transition, *Phys. Rev. Lett.* **75**, 132 (1995).

[169] Dubi, Y., Meir, Y., and Avishai, Y., Unifying Model for Several Classes of Two-Dimensional Phase Transition, *Phys. Rev. Lett.* **94**, 156406 (2005).

[170] Yongho Seo, Paul Cadden-Zimansky, and Venkat Chandrasekhar. Low-temperature high-resolution magnetic force microscopy using a quartz tuning fork. *APPLIED PHYSICS LETTERS* **87**, 103103 (2005).

[171] V. Chandrasekhar and M. M. Mehta, RTSPM: Real-time Linux control software for scanning probe microscopy, *Rev. Sci. Instrum.* **84**, 013705 (2013).

[172] Manan Mehta and V. Chandrasekhar, A hybrid analog-digital phase-locked loop for frequency mode non-contact scanning probe microscopy, *Rev. Sci. Instrum.* **85**, 013707 (2014).

[173] Jilin Xia, Fang Chen, Jinghong Li and Nongjian Tao, Measurement of the quantum capacitance of graphene, *Nature Nanotechnology* **4**, 505 - 509 (2009).

[174] Yukio Tanaka and Satoshi Kashiwaya, Josephson Effect in Unconventional-Superconductor/Ferromagnet/Unconventional-Superconductor Junctions, *Journal of the Physical Society of Japan* **68**, 3485-3488 (1999).